

AD-A155 480

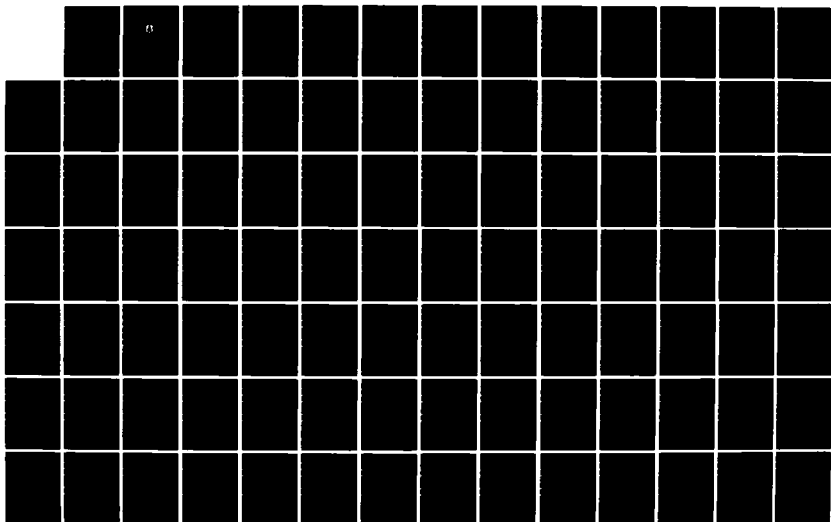
ACTA AERODYNAMICA SINICA(U) FOREIGN TECHNOLOGY DIV
WRIGHT-PATTERSON AFB OH 30 APR 85 FTD-ID(RS)T-1168-84

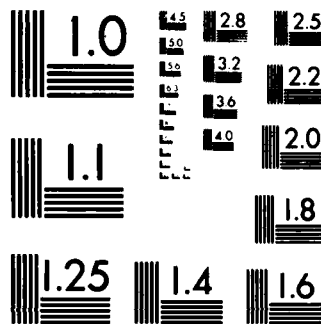
1/2

UNCLASSIFIED

F/G 20/4

NL





MICROCOPY RESOLUTION TEST CHART
NATIONAL BUREAU OF STANDARDS-1963-A



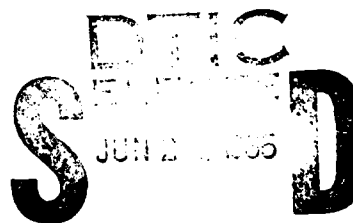
FTD-ID(RS)T-1168-84

AD-A155 480

FOREIGN TECHNOLOGY DIVISION



ACTA AERODYNAMICA SINICA



76 G

Approved for public release;
distribution unlimited.

85 5 28 133

AD-A155 480



EDITED TRANSLATION

FTD-ID(RS)T-1168-84

30 April 1985

MICROFICHE NR: FTD-85-C-000269

ACTA AERODYNAMICA SINICA

English pages: 131

Source: Konggi Donglixue Xuebao, Nr. 1, 1984,
pp. 1-39; 49-63; 71-84; 100-105

Country of origin: China

Translated by: SCITRAN
F33657-84-E-0165

Requester: FTD/TQTA

Approved for public release; distribution unlimited.

THIS TRANSLATION IS A RENDITION OF THE ORIGINAL FOREIGN TEXT WITHOUT ANY ANALYTICAL OR EDITORIAL COMMENT. STATEMENTS OR THEORIES ADVOCATED OR IMPLIED ARE THOSE OF THE SOURCE AND DO NOT NECESSARILY REFLECT THE POSITION OR OPINION OF THE FOREIGN TECHNOLOGY DIVISION.

PREPARED BY:

TRANSLATION DIVISION
FOREIGN TECHNOLOGY DIVISION
WP-afb, OHIO.

Accession For	
NTIS GRA&I	<input checked="" type="checkbox"/>
DTIC TAB	<input type="checkbox"/>
Unannounced	<input type="checkbox"/>
Justification	
By	
Distribution/	
Availability Codes	
Dist	Avail and/or Special
A/1	



Table of Contents

Graphics Disclaimer	ii
A Boundary Element Technique in Transonic Flow; by Yang Zuosheng	1
The Exploration of the Spatial Oscillations in Finite Difference Solutions for Navier-Stokes Shocks; by Zhang Hanxin	18
Calculation of Boundary Layer Growth Behind an Unsteady Expansion Wave in a Tube; by Wang Songgao	33
Numerical Computation for Inviscid Supersonic Flow Around a Bent Cone; by Ji Chuqun	46
Theory of Similarity and the Profile of the Mean Density Distribution of Hypersonic Boundary Layer; by Cai Shutang	66
The Engineering Numerical Technique for the Determination of the Inviscid Flow Field Heating Rate on Ballistic Re-entry Vehicles; by Yang Maozhao, He Fangshang	76
Visualization of Three Dimensional Separated Flows Using the Smoke Wire Technique; by Xia Xuejian	91
The Application of Surface Hot Film in Aerodynamic Testing; by Wang Tiecheng	104
Measurement of the Correlation Between the Fluctuating Pressure and the Fluctuating Velocity in a Turbulent Boundary Layer, by J.F. Morrison, P. Bradshaw	122

GRAPHICS DISCLAIMER

All figures, graphics, tables equations, etc. merged into this translation were extracted from the best quality copy available.

A Boundary Element Technique in Transonic Flow

/1

Yang Zuosheng

(Nanjing Aeronautical Institute)

I. Introduction

The name "boundary element" originates from C.A. Brebbia^[1]. The characteristic of the boundary element technique is that all the nodal unknowns are located on the surface boundary. Consequently, the numerical calculation is simplified and the required computer capacity is reduced. In this work, this technique was extended to the nonlinear transonic flow about a three-dimensional wing. A weighted residual formula suited for the transonic range was established and directly applied to the full velocity potential equation. In order to ensure the irreversibility of shock waves and to facilitate the solution to converge in the supercritical flow region, we added an artificial viscosity term to the full velocity potential equation. Furthermore, the flow field was divided into small subdomains and the Green theorem was applied to each element. If the selected interpolation function has C^1 continuity with respect to the velocity potential ϕ for every element, then the surface integrals of two neighboring elements cancel each other at the interface so that the remaining surface integral (consequently the nodal unknown) is located on the wing boundary. Thus, the boundary element integral equation was derived.

II. Full Velocity Potential Equation with Artificial Viscosity

The three-dimensional continuity equation is:

$$\frac{\partial(\rho U)}{\partial x} + \frac{\partial(\rho V)}{\partial y} + \frac{\partial(\rho W)}{\partial z} = 0 \quad (1)$$

where the x-axis is the flow direction, y-axis points at the right wing and x, y and z form an orthogonal right-handed coordinate. The full velocity potential equation for a nonviscous potential flow can be derived from equation (1):

$$\frac{\rho}{a^2} \left\{ (a^2 - U^2) \phi_{,xx} - UV \phi_{,xy} - UW \phi_{,xz} - VU \phi_{,yx} + (a^2 - V^2) \phi_{,yy} - VW \phi_{,yz} - WU \phi_{,zy} - WV \phi_{,xy} + (a^2 - W^2) \phi_{,zz} \right\} = 0 \quad (2)$$

where P is density and a is speed of sound. $U = \phi_{,x}$, $V = \phi_{,y}$ and $W = \phi_{,z}$ represent the three velocity components along x , y and z axes, respectively.

In the supercritical flow region, the following artificial compressibility (viscosity) was added to prevent an expansion shock wave solution and to eliminate any shock wave discontinuity by referring to equation (1):

$$-\left\{ \frac{\partial}{\partial x} \left[U \mu_1 A \frac{\partial \rho}{\partial \bar{x}} \right] + \frac{\partial}{\partial y} \left[V \mu_2 A \frac{\partial \rho}{\partial \bar{y}} \right] + \frac{\partial}{\partial z} \left[W \mu_3 A \frac{\partial \rho}{\partial \bar{z}} \right] \right\} \quad (3)$$

where $\mu_1 = \Delta x$, $\mu_2 = \Delta y$, $\mu_3 = \Delta z$. A is a switch function.

$$A = \max \left(0, 1 - \frac{M^2}{M_c^2} \right) \quad /2 \quad (4)$$

When the local flow Mach number M is less than M_c , A is zero. In this work, $M_c^2 = 0.8$. $\partial \rho / \partial \bar{x}$, $\partial \rho / \partial \bar{y}$ and $\partial \rho / \partial \bar{z}$ represent the partial differentiation of ρ in the x , y and z direction, respectively. If the artificial compressibility term (3) is superimposed onto the continuity equation (1), the local density will be replaced by the value upstream when the local Mach number exceeds M_c in order to permit receiving information from upstream. After expanding equation (3) and adding it to equation (2), the artificially viscous full velocity potential equation can be expressed as (in tensor symbols and abbreviated format):

$$K_{,ij} \phi_{,ij} = 0 ; \quad i, j = 1, 2, 3 \quad (5)$$

where

$$K_{,ij} = [\delta_{,ij} a^2 - \phi_{,i} \phi_{,j} - A(\delta_{,ij} a^2 \phi_{,i} \phi_{,j}) + A(\delta_{,ij} a^2 - \phi_{,i} \phi_{,j} \phi_{,i} \phi_{,j} / \phi_{,ii})] \quad (6)$$

The repeated subscripts indicate summation in the subscript range. The subscript ",," represents differentiation $\delta_{ij} = 0$ (when $i = j$) and $\delta_{ij} = 1$ (when $i \neq j$). ϕ_1 , ϕ_2 and ϕ_3 represents the ϕ values at $(x-\Delta x, y, z)$, $(x, y-\Delta y, z)$ and $(x, y, z-\Delta z)$, respectively.

III. Boundary Element Integration Equation

Equation (5) can be rewritten as:

$$K_{ij}\phi_{,i} = (K_{ij}\phi_{,i})_{,j} - \phi_{,j}K_{ij,i} = 0 \quad i, j = 1, 2, 3 \quad (7)$$

Using a finite element method, we divided the Ω region of the flow field into M elements. If ϕ is replaced by its approximation $\tilde{\phi}$ in each element, then the weighted residual expression for equation (7) is:

$$\sum_{e=1}^M \int_{\Omega_e} (K_{ij}\tilde{\phi}_{,i})_{,j} G d\Omega - \sum_{e=1}^M \int_{\Omega_e} \tilde{\phi}_{,j} K_{ij,i} G d\Omega = 0 \quad (8)$$

For simplicity, the superscript "~" is omitted in the following. G is a weighted function yet to be determined. We applied the Green theorem to each element Ω_e in the first volume integral on the left side of equation (8). If the interpolation function chosen for ϕ has C^1 continuity, i.e., ϕ and its first order derivative is continuous across the boundary, then the boundary surface integrals of neighboring elements will cancel out. After applying Green theorem twice to the first integral on the left side of equation (8), the surface integral is located on the boundary S. Thus, equation (8) becomes: (with respect to wings, including external surface and its rear vortex surface):

$$\begin{aligned} \sum_{e=1}^M \left[\int_{S_e} G K_{ij}\phi_{,i} n_j dS - \int_{S_e} \phi K_{ij} G_{,i} n_j dS \right] + \sum_{e=1}^M \int_{\Omega_e} \phi K_{ij} G_{,i} d\Omega + \\ + \sum_{e=1}^M \int_{\Omega_e} \phi G_{,j} K_{ij,i} d\Omega - \sum_{e=1}^M \int_{\Omega_e} \phi_{,j} K_{ij,i} G d\Omega = 0 \end{aligned} \quad (9)$$

where S_e is the area of the element e on the boundary S. If the element Ω_e is divided small enough, then K_{ij} can be assumed to be a constant in each element. In the n^{th} iteration, its value is

equal to that in the middle of the element, $K_{ij}^{(n-1)}$, in the $(n-1)^{th}$ iteration. Thus, $K_{ij,i} = K_{ij,j} = 0$ in each element. It is a step function. Its derivative $K_{ij,i}$ or $K_{ij,j}$ is a pulse function. In order to satisfy the continuity requirement for ϕ_{ij} across the boundary, we assumed that the variation of K_{ij} is linear in the vicinity of the boundary. Thus, the volume integral in equation (9) is reduced to the following surface integral along the boundary:

$$\sum_{i=1}^M \int_{\Omega_i} \phi_{G,i} K_{ij,i} d\Omega = \sum_{i=1}^J \int \phi_{G,i} \Delta K_{1,i} dS_P + \sum_{i=1}^K \int \phi_{G,i} \Delta K_{2,i} dS_Q + \sum_{i=1}^L \int \phi_{G,i} \Delta K_{3,i} dS_R \quad (10)$$

$$\sum_{i=1}^M \int_{\Omega_i} \phi_{G,i} K_{ij,i} G d\Omega = \sum_{i=1}^J \int G \phi_{G,i} \Delta K_{1,i} dS_P + \sum_{i=1}^K \int G \phi_{G,i} \Delta K_{2,i} dS_Q + \sum_{i=1}^L \int G \phi_{G,i} \Delta K_{3,i} dS_R \quad (11)$$

$i = 1, 2, 3$

where P, Q, and R are the local coordinates for the element. dS_P , dS_Q and dS_R represent the differential areas on the boundary when $P = \text{const.}$, $Q = \text{const.}$, and $R = \text{const.}$, respectively. J, K, and L represent the total number of boundaries on the planes where $P = \text{const.}$, $Q = \text{const.}$, and $R = \text{const.}$, respectively. Hence, equation (9) can be written as the following in the n^{th} iteration.

$$\sum_{i=1}^M \left[\int_{\Omega_i} G K_{ij,i}^{(n-1)} \phi_{G,i} d\Omega - \int_{\Omega_i} \phi_{G,i} K_{ij,i}^{(n-1)} G d\Omega \right] + \sum_{i=1}^J \int \Delta K_{1,i}^{(n-1)} (\phi_{G,i} - G \phi_{G,i})^{(n-1)} dS_P + \sum_{i=1}^K \int \Delta K_{2,i}^{(n-1)} (\phi_{G,i} - G \phi_{G,i})^{(n-1)} dS_Q + \sum_{i=1}^L \int \Delta K_{3,i}^{(n-1)} (\phi_{G,i} - G \phi_{G,i})^{(n-1)} dS_R = 0 \quad (12)$$

$i, j = 1, 2, 3$

If K_{ij} is a positive definite (which is always satisfied in a subcritical flow), we obtain the fundamental solution G^* to the following equation as the weighted function G:

$$K_{ij}^{(n-1)} G_{,ij} = -4\pi \delta(\vec{x}_i - \vec{x}_j) \quad (13)$$

When $K_{ij}^{(n-1)}$ is constant, the basic solution to this equation is^[2]

$$G^*(\vec{x}_i, \vec{x}_j) = |K^{ij}|^{\frac{1}{2}} \frac{1}{R} \quad (13)'$$

where δ is a pulse function.

$$R^2 = K^{ij}(x_i - x_j)(x_i - x_j), \quad i, j = 1, 2, 3 \quad (14)$$

K^{ij} is the inverse matrix of K_{ij} and $|K^{ij}|$ is the determinant of the matrix K^{ij} . \vec{x}_i and \vec{x}_i' represent the coordinate vectors of a fixed point and a moving point, respectively. When a fixed point and a moving point \vec{x}_i are outside an element Ω_e , then $\vec{x}_i \neq \vec{x}_i'$.

The third integral in equation (12) is zero. When the fixed point \vec{x}_i is inside an element Ω_e , based on the characteristic of a pulse function, the volume integral of the element is $-4\pi\phi(\vec{x}_i)$. /4

In the supercritical flow region, K_{ij} is no longer positive definite; however, $K_{ij}^{(n-1)}$ in equation (13) must be positive definite. Therefore, the third term in equation (12) must be rewritten if the neighboring upstream element is still supercritical:

$$\sum_{i=1}^M \int_{\Omega_e} \phi K_{ij}^{(n-1)} G_{,ij} d\Omega = \sum_{i=1}^M \int_{\Omega_e} \phi \bar{K}_{ij}^{(n-1)} G_{,ij} d\Omega + H \quad (15)$$

where

$$H = \sum_{i=1}^{M_s} \int_{\Omega_e} \phi (K_{ij}^{(n-1)} - \bar{K}_{ij}^{(n-1)}) G_{,ij} d\Omega \quad (16)$$

Here, \bar{K}_{ij} represents the K_{ij} value at the first subcritical element upstream from the supercritical element. M_s is the total number of supercritical elements. Because M_s is finite, the workload to calculate the volume integral H is also finite. Thus, the following boundary element integral for velocity potential ϕ can be obtained from equation (12):

$$4\pi\phi(\vec{x}) = \sum_{i=1}^N \left[\int_{s_i} G^* K_{ij}^{(n-1)} \phi(\vec{x}) n_j dS - \int_{s_i} \phi K_{ij}^{(n-1)} G^* n_j dS \right] + B + H \quad (17)$$

where

$$B = \sum_{i=1}^I \int \Delta K_{ij}^{(n-1)} (\phi G^* - G^* \phi)_{i=x_p}^{(n-1)} dS_p + \sum_{i=1}^K \int \Delta K_{ij}^{(n-1)} (\phi G^* - G^* \phi)_{i=z_p}^{(n-1)} dS_p + \sum_{i=1}^L \int \Delta K_{ij}^{(n-1)} (\phi G^* - G^* \phi)_{i=y_p}^{(n-1)} dS_p \quad (18)$$

ΔK_{ij} represents the difference between two neighboring K_{ij} values. By respectively differentiating equation (17) with respect to x , y and z , the corresponding boundary conditions are

$$\begin{aligned} \vec{q} \cdot \vec{n} &= 0 & (\text{on wing surface}) \\ \Delta C_p &= 0 & (\text{on tail vortex surface}) \\ \phi &= V_\infty x & (\text{at infinity}) \end{aligned} \quad (19)$$

where ΔC_p is the difference of pressure indices between the top and bottom surface, and q is the full velocity.

In the transonic small perturbation field for a thin wing, the boundary element integral equation (17) can be simplified as:

$$\begin{aligned} 4\pi\phi(x, y, z) &= \sum_{i=1}^N \left\{ \int_{s_i} \Delta\varphi \frac{\partial G^*(n-1)}{\partial \xi} dS - \int_{s_i} G^*(n-1) \Delta \frac{\partial \varphi}{\partial \xi} dS \right\} + \\ &+ \sum_{i=1}^I \int_{s_i} \Delta K_{ii} \left(\varphi \frac{\partial G^*}{\partial \xi} - G^* \frac{\partial \varphi}{\partial \xi} \right)_{i=x_p}^{(n-1)} dS_p + H \end{aligned} \quad (20)$$

Differentiating equation (20) with respect to x , we get

$$\begin{aligned} 4\pi u(x, y, z) &= \sum_{i=1}^N \left\{ \int_{s_i} \Delta\varphi \frac{\partial^2 G^*(n-1)}{\partial x \partial \xi} dS - \int_{s_i} \frac{\partial G^*(n-1)}{\partial x} \Delta \frac{\partial \varphi}{\partial \xi} dS \right\} + \\ &+ \sum_{i=1}^I \frac{\partial}{\partial x} \int_{s_i} \Delta K_{ii} \left(\varphi \frac{\partial G^*}{\partial \xi} - G^* \frac{\partial \varphi}{\partial \xi} \right)_{i=x_p}^{(n-1)} dS_p + \frac{\partial H}{\partial x} \end{aligned} \quad (21) \quad /5$$

Differentiating equation (20) with respect to y , we get

$$\begin{aligned} 4\pi v(x, y, z) &= \sum_{i=1}^N \left\{ \int_{s_i} \Delta\varphi \frac{\partial^2 G^*(n-1)}{\partial y \partial \xi} dS - \int_{s_i} \frac{\partial G^*(n-1)}{\partial y} \Delta \frac{\partial \varphi}{\partial \xi} dS \right\} + \\ &+ \sum_{i=1}^I \frac{\partial}{\partial y} \int_{s_i} \Delta K_{ii} \left(\varphi \frac{\partial G^*}{\partial \xi} - G^* \frac{\partial \varphi}{\partial \xi} \right)_{i=x_p}^{(n-1)} dS_p + \frac{\partial H}{\partial y} \end{aligned} \quad (22)$$

where x_p represents the x coordinate on the plane where $P = \text{const}$. Differentiating equation (20) with respect to z , we get

$$4\pi w(x, y, z) = \sum_{e=1}^N \left\{ \int_{S_e} \Delta \varphi \frac{\partial^2 G^{*(''-1)}}{\partial z \partial \xi} dS - \int_{S_e} \frac{\partial G^{*(''-1)}}{\partial z} \Delta \frac{\partial \varphi}{\partial \xi} dS \right\} + \\ + \sum_{e=1}^I \frac{\partial}{\partial z} \int_{S_e} \Delta K_{11} \left(\varphi \frac{\partial G^*}{\partial \xi} - G^* \frac{\partial \varphi}{\partial \xi} \right)_{t=t_e} dS_e + \frac{\partial H}{\partial z} \quad (23)$$

For a small perturbation flow field, we obtain the following from equation (6):

$$\begin{cases} K_{11} = 1 - M_\infty^2 - [3 - (2 - \gamma) M_\infty^2] M_\infty^2 u(x, y, z) + A[3 - (2 - \gamma) M_\infty^2] \times \\ \quad M_\infty^2 u(x, y, z) - A[3 - (2 - \gamma) M_\infty^2] M_\infty^2 u(x - \Delta x, y, z) \\ K_{22} = K_{33} = 1 \\ K_{12} = K_{13} = K_{21} = K_{23} = K_{31} = K_{32} = 0 \end{cases} \quad (24)$$

From equations (13)' and (14), we get

$$G^{*(''-1)} = 1 / \sqrt{(x - \xi)^2 + K_{11}^{(''-1)} [(y - \eta)^2 + (z - \xi)^2]} \quad (25)$$

In equations (20) - (23):

$$\left. \begin{aligned} \Delta \varphi(\xi, \eta, 0) &= \varphi(\xi, \eta, 0_+) - \varphi(\xi, \eta, 0_-) \\ \Delta \frac{\partial \varphi}{\partial \xi}(\xi, \eta, 0) &= \frac{\partial \varphi}{\partial \xi}(\xi, \eta, 0_+) - \frac{\partial \varphi}{\partial \xi}(\xi, \eta, 0_-) \end{aligned} \right\} \quad (26)$$

φ is the small perturbation velocity potential. u , v and w are the small perturbation velocity components along x , y , and z , respectively. γ is the specific heat ($\gamma = 1.4$ for air). S'_e is the area of an element e on the $z = 0$ plane where the boundary surface S is considered to be located in approximation. In order to limit the integration to the wing region S_w , we substituted equation (25) into (20). The first integral on the right side of equation (20) was integrated by part:

$$4\pi \varphi(x, y, z) = \sum_{e=1}^{N_w} \left\{ z \int_{S_w} \frac{\Delta u(\xi, \eta, 0)}{(y - \eta)^2 + z^2} \left[1 + \frac{x - \xi}{\sqrt{(x - \xi)^2 + K_{11}^{(''-1)} [(y - \eta)^2 + z^2]}} \right] dS - \right.$$

Similarly

$$- \int_{S_w} G^{*(''-1)} \Delta \frac{\partial \varphi}{\partial \xi} dS \left. \right\} + \sum_{e=1}^I \int_{S_e} \Delta K_{11} \left(\varphi \frac{\partial G^*}{\partial \xi} - G^* \frac{\partial \varphi}{\partial \xi} \right)_{t=t_e} dS_e + H \quad (27)$$

$$4\pi u(x, y, z) = \sum_{i=1}^{N_w} \left\{ K_{11}^{(n-1)} z \int_{s_{w,i}} \frac{\Delta u(\xi, \eta, 0)}{[(x-\xi)^2 + K_{11}^{(n-1)} [(y-\eta)^2 + z^2]^{\frac{1}{2}}} dS - \right. \\ \left. - \int_{s_{w,i}} \frac{\partial G^{*(n-1)}}{\partial x} \Delta \frac{\partial \varphi}{\partial \xi} dS \right\} + \sum_{i=1}^I \frac{\partial}{\partial x} \int_{s_i} \Delta K_{11} \left(\varphi \frac{\partial G^*}{\partial \xi} - G^* \frac{\partial \varphi}{\partial \xi} \right)_{t-z, i}^{(n-1)} dS_i + \frac{\partial H}{\partial x} \quad (28)$$

$$4\pi v(x, y, z) = \sum_{i=1}^{N_w} \left\{ z \frac{\partial}{\partial y} \int_{s_{w,i}} \frac{\Delta u(\xi, \eta, 0)}{(y-\eta)^2 + z^2} \left[1 + \frac{x-\xi}{\sqrt{(x-\xi)^2 + K_{11}^{(n-1)} [(y-\eta)^2 + z^2]}} \right] \times \right. \\ \times dS - \int_{s_{w,i}} \frac{\partial G^{*(n-1)}}{\partial y} \Delta \frac{\partial \varphi}{\partial \xi} dS + \sum_{i=1}^I \frac{\partial}{\partial y} \int_{s_i} \Delta K_{11} \left(\varphi \frac{\partial G^*}{\partial \xi} - G^* \frac{\partial \varphi}{\partial \xi} \right)_{t-z, i}^{(n-1)} \\ \times dS_i + \frac{\partial H}{\partial y} \quad (29)$$

$$4\pi w(x, y, z) = \sum_{i=1}^{N_w} \left\{ \left(1 + z \frac{\partial}{\partial z} \right) \int_{s_{w,i}} \frac{\Delta u(\xi, \eta, 0)}{(y-\eta)^2 + z^2} \times \right. \\ \times \left[1 + \frac{x-\xi}{\sqrt{(x-\xi)^2 + K_{11}^{(n-1)} [(y-\eta)^2 + z^2]}} \right] dS - \\ - \int_{s_{w,i}} \frac{\partial G^{*(n-1)}}{\partial z} \Delta \frac{\partial \varphi}{\partial \xi} dS \Big\} + \sum_{i=1}^I \frac{\partial}{\partial z} \int_{s_i} \Delta K_{11} \left(\varphi \frac{\partial G^*}{\partial \xi} - G^* \frac{\partial \varphi}{\partial \xi} \right)_{t-z, i}^{(n-1)} \\ \times dS_i + \frac{\partial H}{\partial z} \quad (30)$$

When the fixed point (x, y, z) is located on the wing surface ($z = 0_+$), the following can be derived from equations (28) and (30):

$$4\pi[u(x, y, 0_+) + u(x, y, 0_-)] = -2 \sum_{i=1}^{N_w} \int_{s_{w,i}} \frac{\partial G^{*(n-1)}}{\partial x} \Delta \frac{\partial \varphi}{\partial \xi} dS + D + E \quad (31)$$

$$4\pi[w(x, y, 0_+) + w(x, y, 0_-)] = \lim_{z \rightarrow 0} 2 \sum_{i=1}^{N_w} \int_{S_i} \frac{\Delta u(\xi, \eta, 0)}{(y-\eta)^2 + z^2} \left[1 + \frac{x-\xi}{\sqrt{(x-\xi)^2 + K_{i1}^{(n-1)} [(y-\eta)^2 + z^2]}} \right] dS + F + G \quad (32)$$

where

$$\left. \begin{aligned} D &= 2 \sum_{i=1}^I \frac{\partial}{\partial x} \int_{S_i} \Delta K_{i1} \left(\varphi \frac{\partial G^*}{\partial \xi} - G^* \frac{\partial \varphi}{\partial \xi} \right)_{t=t_i}^{(n-1)} dS_i \\ E &= 2 \frac{\partial H}{\partial x} \\ F &= 2 \sum_{i=1}^I \frac{\partial}{\partial z} \int_{S_i} \Delta K_{i1} \left(\varphi \frac{\partial G^*}{\partial \xi} - G^* \frac{\partial \varphi}{\partial \xi} \right)_{t=t_i}^{(n-1)} dS_i \\ G &= 2 \frac{\partial H}{\partial z} \end{aligned} \right\} \quad (33) \quad /7$$

For a thin wing, the boundary conditions (19) can be simplified as:

$$\begin{aligned} w &= \partial \varphi / \partial z = dz' / dx' - a \quad (\text{on wing surface}) \\ \Delta C_p &= 2 \Delta u = 0 \quad (\text{on tail vortex surface}) \\ \nabla \varphi &= 0 \quad (\bar{y}, \bar{z} \rightarrow \pm \infty) \end{aligned} \quad (34)$$

where z' is the vertical coordinate of the lower wing surface in the body axis coordinate x', y', z' and a is the attack angle. The first term on the right hand side of equation (31) is similar to the linearized small perturbation thickness integral; therefore, the result of the linearized equation can be directly used. Equation (32) can be considered as the expression for a linearized small perturbation lift problem when the effective washdown velocity at the control point is $w(x, y, 0_+) + w(x, y, 0_-)/2 + (F+G)/4\pi$. Therefore, once the values of F and G are determined, it is possible to solve equation (32) by familiar numerical methods for the linearized lift problem (such as nuclear function method and vortex lattice method)^[4] to obtain the corresponding $\Delta u(x, y, 0)$ distribution along the wing surface and the F and G values.

IV. Solution

We divided it along the wing surface into N_w quadrangular elements. Moreover, planes ($p = \text{const.}$) perpendicular to the

wing surface were made along the chord direction of the wing element. These planes extend to a height approximately equal to 2 times the chord length. Many quadrangular elements were divided along the plane, as shown in Figure 1. Figure 1 only shows one of the $P = \text{const.}$ planes and the partitioning of its elements. In order to ensure that φ has C^1 continuity across the boundary on a $P = \text{const.}$ plane, we expressed φ in an element approximately as:

$$\begin{aligned} \varphi = & L_1 \varphi_1 + L_2 v_1 + L_3 w_1 + L_4 \varphi_2 + L_5 v_2 + L_6 w_2 + L_7 \varphi_3 + L_8 v_3 \\ & + L_9 w_3 + L_{10} \varphi_4 + L_{11} v_4 + L_{12} w_4 \end{aligned} \quad (35)$$

where L_i ($i = 1, 2, \dots, 12$) is the interpolation function. The subscripts 1, 2, 3, 4 of v , w represent the values at corresponding nodal points of the quadrangle, as shown in Figure 2. In the element coordinate QR shown in the figure, L_i can be expressed as^[3]:

$$\left. \begin{aligned} L_1 &= f_1(R) f_1(Q), & L_2 &= g_1(R) g_1(Q) \\ L_3 &= f_1(Q) g_1(R), & L_4 &= f_2(Q) f_1(R) \\ L_5 &= g_2(Q) f_1(R), & L_6 &= f_2(Q) g_2(R) \\ L_7 &= f_2(R) f_2(Q), & L_8 &= g_2(R) g_2(Q) \\ L_9 &= f_2(Q) g_2(R), & L_{10} &= f_1(Q) f_2(R) \\ L_{11} &= g_1(Q) f_1(R), & L_{12} &= f_1(Q) g_2(R) \end{aligned} \right\} \quad (36)$$

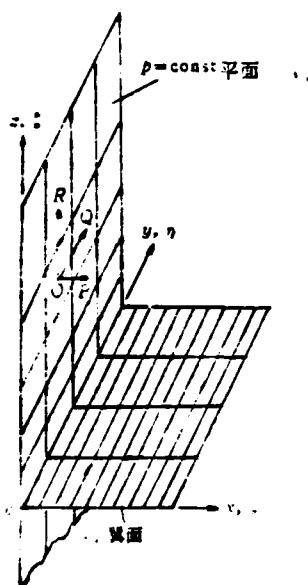


Figure 1

1. $p = \text{const.}$ plane
2. wing surface

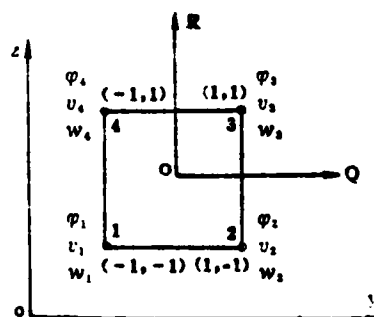


Figure 2

The functions are

$$f_1(\theta) = 1 - 3\left(\frac{\theta+1}{2}\right)^2 + 2\left(\frac{\theta+1}{2}\right)^3$$

$$f_2(\theta) = 3\left(\frac{\theta+1}{2}\right)^2 - 2\left(\frac{\theta+1}{2}\right)^3$$

$$g_1(\theta) = \frac{\theta+1}{2} - 2\left(\frac{\theta+1}{2}\right)^2 + \left(\frac{\theta+1}{2}\right)^3$$

$$g_2(\theta) = \left(\frac{\theta+1}{2}\right)^3 - \left(\frac{\theta+1}{2}\right)^2$$

The variable θ represents R or Q. The overall coordinate of a point in an element can be expressed by the overall coordinates of its four nodal points:

$$\begin{aligned} y = & \frac{1}{4}(1-R)(1-Q)y_1 + \frac{1}{4}(1+Q)(1-R)y_2 + \frac{1}{4}(1+R)(1+Q)y_3 + \\ & + \frac{1}{4}(1-Q)(1+R)y_4 \\ z = & \frac{1}{4}(1-R)(1-Q)z_1 + \frac{1}{4}(1-R)(1+Q)z_2 + \frac{1}{4}(1+R)(1+Q)z_3 + \\ & + \frac{1}{4}(1+R)(1-Q)z_4 \end{aligned} \quad (37)$$

The value of u in each element on a $P = \text{const.}$ plane can be approximated by the u value at the center of the element. The solution finding process is:

1. First, we assume the $u(x, y, 0_+)$ values at the center of each element on the wing surface, the values of v and w at the nodal points of each element on $P = \text{const.}$ planes, and the values of u at the centers of elements. They are used as initial values.

2. By substituting equation (35) into (33), the values of D , E , F , and G are obtained from the given initial values after transforming the integration variables to R and Q .

3. Using the vortex lattice method^[4], the value of $u(x, y, 0)$ at the center of each element on the wing surface can be obtained from equation (32) based on the boundary condition (34) and calculated values of F and G .

4. The calculated values of D and E , as well as the value of $u(x, y, 0-) = u(x, y, 0+) - \Delta u$, are substituted into equation (31). Furthermore, equation (31) is satisfied at the center of each element on the wing surface so that $u(x, y, 0)$ can be obtained at the center of each element on the wing surface.

5. According to equations (27), (29) and (30), the values of ϕ, v and w are calculated at each nodal point on $P = \text{const.}$ planes. The value of u at the center of each element on a $P = \text{const.}$ plane is calculated based on equation (28).

6. Steps 2, 3 and 4 are repeated until the difference of two consecutive values of $u(x, y, 0+)$ at the center of each wing surface element is less than the specified value.

In order to allow the solution to converge in the supercritical region, the contribution from the supersonic point $(x, y, 0-)$ should equal zero.

V. Examples

The examples shown in Figures 3-5 are identical to those in reference [4]. The number of elements on the wing surface is also equal to that in reference [4]. In the $P = \text{const.}$ plane, it was partitioned into five regions along the height according to the law of tangent (from 0° - 63.4°). The partitioning in the span direction is similar to that on the wing surface. From these figures, the results in this work agree well with those in references [4] and [5]. However, when there is an attack angle, the front fringe result of this work is between those of references [4] and [5]. Figure 6 shows the calculated pressure distributions along the chord direction at three span positions of a dull leading edge rectangular wing by using this method and the difference method used in reference [6]. One can see that they are in good agreement.

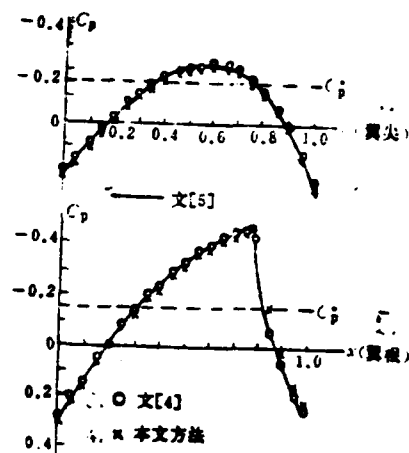


Figure 3. Rectangular Wing with Aspect Ratio 4 (double arc wing, relative thickness 6%), $M_\infty = 0.908$, $\alpha = 0$

1. (wing tip)
2. reference [5]
3. reference [4]
4. this work
5. wing root

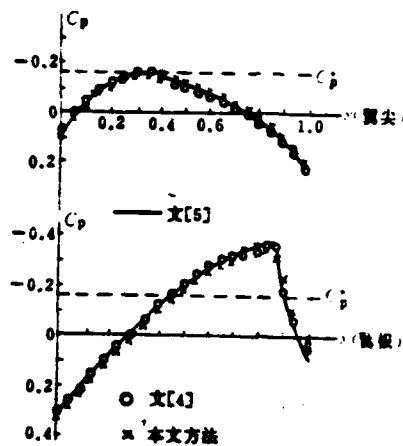


Figure 4. 30 Equi-chord Length Sweptback Wing with Aspect Ratio 4 (double arc wing, relative thickness 6%), $M_\infty = 0.908$, $\alpha = 0$

1. wing tip
2. reference [5]
3. reference [4]
4. this work
5. wing root

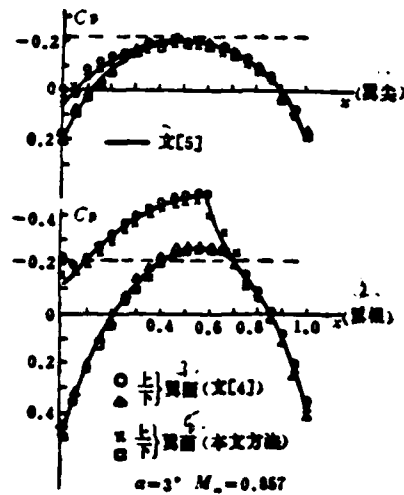


Figure 5. Rectangular Wing with Aspect Ratio 2 (double arc wing, relative thickness 6%)

1. wing tip
2. reference [5]
3. wing root
4. upper
lower } wing surface (ref.[4])
5. upper
lower } wing surface (this method)

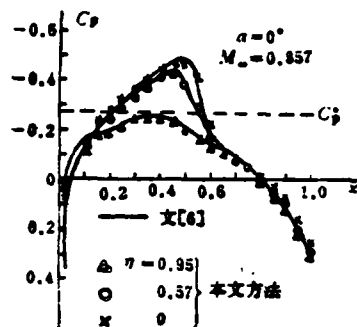


Figure 6. Rectangular Wing with Aspect Ratio 5 (Model NACA64A006)

1. this method

References

- [1] Brebbia, C.A., The Boundary Element Method for Engineers, Pentech Press, 1978.
- [2] Chang, Y.P., Kang, C.S., Chen, D.J., Int. J. Heat Mass Transfer, Vol. 16, pp. 1905-1918, 1973.
- [3] Connor, J.J., Brebbia, C.A., Finite Element Techniques for Fluid Flow, 2nd ed., Newnes-Butterworths, London, 1977.
- [4] Yang, Z.S., Proceedings of the Fourth International Symposium on Finite Element Methods in Flow Problems, pp. 425-432, 1982.
- [5] Bailey, F.R., Steger, J.L., AIAA Paper 72-189.
- [6] Weatherill, W.H., NASA CR-2933.

A BOUNDARY ELEMENT TECHNIQUE IN TRANSONIC FLOW

Yang Zuosheng

(Nanjing Aeronautical Institute)

Abstract

The boundary element technique is now extended to study the nonlinear transonic flow about three dimensional wings. A weighted residual formulation, valid throughout a Mach number range including transonic, is developed and applied directly both to the nonviscous full velocity potential equation and transonic small perturbation equation. In order to ensure the irreversible character of shock wave and to make the solutions stable and converged in supercritical region, an artificial viscosity term is introduced. We partition the flow domain into a number of small elements and apply the Green theorem to each element. The boundary integral equations are obtained by using an interpolation function which is C^1 continuous for velocity potential and finally solved by means of finite element collocation method.

The Exploration of the Spatial Oscillations in Finite Difference Solutions for Navier-Stokes Shocks

Zhang Hanxin

(China Aerodynamic Research and Development Center)

Abstract

In this paper, the cause for the oscillations in the upstream and downstream difference solutions was investigated. The study showed that adding a second order diffusion term to the Navier-Stokes equation could smooth out the shock wave. However, the third order dispersion term and fourth order diffusion term could cause oscillations in the upstream and downstream solutions under certain given conditions. If the second or third order difference method is used to solve the NS shock wave equation, the solution oscillates because of the dispersion and diffusion terms.

I. Introduction

When a difference method is used to solve a shock wave motion, if the difference method is of the first order of accuracy (or with an added second order diffusion term), the shock wave is smeared. If the difference method is of higher orders of accuracy such as second or third order, oscillations frequently appear upstream and downstream^{[1][2]}. In reality, there is no oscillation^[3]. This oscillation still exists when the computation stabilizes. It is significant to explain the cause of this oscillation.

In this paper, an attempt was made to perform an enlightening analysis. We believe that because the step lengths of spatial lattice and time are not zero in the difference equation, it is approximately correct to use the difference quotient to replace the derivative. Therefore, there is a finite difference between the difference equation and differential equation. For example, the model equation for the initial value

problem is

$$\frac{\partial u}{\partial t} + a \frac{\partial u}{\partial x} = \nu \frac{\partial^2 u}{\partial x^2} \quad (1.1)$$

In the corresponding difference equation, when the difference is expressed in a Taylor series the equivalent equation is:

$$\frac{\partial u}{\partial t} + a \frac{\partial u}{\partial x} = \nu \frac{\partial^2 u}{\partial x^2} + \sum_{n=1}^{\infty} \nu_n \frac{\partial^n u}{\partial x^n} \quad (1.2)$$

This equation is called the correction formula for (1.1) where K is the accuracy of the difference lattice and ν_n is a coefficient related to time and spatial steps. For compatible difference lattices, when the time and spatial steps approach zero, $\nu_n \rightarrow 0$. Comparing (1.1) with (1.2), the difference between differential and difference equation is:

$$\epsilon_s = \sum_{n=1}^{\infty} \nu_n \frac{\partial^n u}{\partial x^n} \quad (1.3)$$

This difference not only affects the stability of the difference equation but also causes the difference between the solution of the difference equation and that of the differential equation.

According to this understanding, we used the small perturbation method to analyze the shock wave flow upstream and downstream. We studied the effect of the second, third, and fourth order terms on the right hand side of the correction equation to illustrate the correlation between the difference format and the oscillation in the solution. Some meaningful conclusions were also provided. /13

II. Effect of Second, Third, and Fourth Order Derivative Terms in the NS Equation of Shock Wave Motion

1. Starting Equation

In order to simulate the effect of ϵ_k in the correction formula, let us study a one-dimensional normal shock wave motion (see Figure 1). The basic equation set is:

$$\rho \frac{\partial u}{\partial t} + \frac{\gamma+1}{2\gamma} \rho \cdot u_{\infty} \left(1 - \frac{u_1 u_{\infty}}{u^2}\right) \frac{\partial u}{\partial x} = \frac{\partial}{\partial x} \left[(v + v_1) \frac{\partial u}{\partial x} \right] - \frac{\partial}{\partial x} \left[v \cdot \frac{\partial^2 u}{\partial x^2} \right] - \frac{\partial}{\partial x} \left[v_1 \cdot \frac{\partial^3 u}{\partial x^3} \right] + \dots \quad (2.1)$$

Here, $\rho = \rho_{\infty} u_{\infty} / u$, ρ and u are the density and the velocity of the gas, t is the time, x represents the coordinate (see Figure 1), γ is the adiabatic index, $v = (4/3)\mu$. μ is the viscosity of the gas which is calculated according to:

$$\mu = \mu_{\infty} \left(\frac{h}{h_{\infty}} \right)^n \quad (A)$$

where

$$h = \frac{1}{2} u_{\infty}^2 \left(1 + \frac{2}{\gamma-1} \frac{1}{M_{\infty}^2} \right) - \frac{1}{2} u^2 \quad (B)$$

The subscript " ∞ " represents the value at $x \rightarrow -\infty$, M is the Mach number and n is the exponent. In equation (2.1)

$$u_1 = \frac{\gamma-1}{\gamma+1} \left(1 + \frac{2}{\gamma-1} \frac{1}{M_{\infty}^2} \right) u_{\infty} \quad (C)$$

v_1 is the coefficient of the added derivative terms which is assumed to be a constant. It should be pointed out that when v_1 's ($i = 2, 3, \dots$) are zero, equation (2.1) is an accurate NS equation accurately describing the positive shock wave motion in normal conditions^[3]. Therefore, the steady state solution to equation (2.1) is the correct shock wave. When v_1 's are not zero and assume certain values related to the lattice step, equation (2.1) simulated the correction formula with a specific difference lattice. Hence, we can study the effect of second and third order terms by solving equation (2.1).

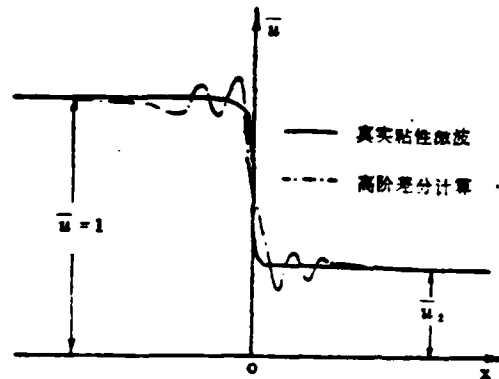


Figure 1. Velocity Distribution of One-dimensional Positive Shock Wave

1. real viscous shock wave
2. higher order difference calculation

2. Effect of Second, Third and Fourth Order Terms

If the distribution of any physical quantity of a nonviscous positive shock wave is used as the initial value, it has already been proven that (2.1) has a steady state smooth shock wave solution when $v_2 = v_3 = v_4 = \dots = 0$ [3]. Its shock wave zone is very thin (assuming the center is $x = 0$). Outside the shock wave region, the physical quantities rapidly approach the upstream and downstream values of a nonviscous shock wave. If v_2, v_3, \dots are not zero, although (2.1) still approaches its nonviscous value far away from the shock wave region yet some oscillation emerges near the shock wave (See Figure 1). In the following, the correlation between v_2, v_3, v_4 and the oscillation is analyzed. /14

In reality, if we only consider the presence of v_2, v_3 and v_4 then (2.1) gives the following when the solution is stabilized:

$$(\nu + \nu_2) \frac{\partial \bar{u}}{\partial x} - \nu_1 \frac{\partial^2 \bar{u}}{\partial x^2} - \nu_3 \frac{\partial^3 \bar{u}}{\partial x^3} = \frac{\gamma + 1}{2\gamma} \rho_\infty u_\infty \frac{(\bar{u} - 1)(\bar{u} - \bar{u}_1)}{\bar{u}} \quad (2.2)$$

where

$$\bar{u} = \frac{u}{u_\infty} \quad (2.3)$$

$$\bar{u}_2 = \frac{\gamma-1}{\gamma+1} \left(1 + \frac{2}{\gamma-1} \frac{1}{M_\infty^2} \right) \quad (2.4)$$

Obviously $\bar{u} = 1$ and $\bar{u} = \bar{u}_2$ are the upstream and downstream values of the nonviscous shock wave, respectively.

Let us study the nature of the solution to (2.2) near $\bar{u} = 1$ and $\bar{u} = \bar{u}_2$. Because $u = 1$ when $x \rightarrow -\infty$ and $\bar{u} = \bar{u}_2$ when $x \rightarrow \infty$, this investigation can provide the characteristics of the solution upstream and downstream.

$$\text{Let } \bar{u} = 1 + u' \text{ (upstream)} \quad (2.5)$$

$$\bar{u} = \bar{u}_2 + u' \text{ (downstream)}$$

Assuming $|u'| \ll 1$ in the upstream and $|u'| \ll \bar{u}_2$ in the downstream, equation (2.5) is substituted into (2.2). After omitting higher order small terms beyond u'^2 , we get

$$\begin{aligned} \mu_1 \frac{\partial u'}{\partial x} - \nu_1 \frac{\partial^2 u'}{\partial x^2} - \nu_1 \frac{\partial^3 u'}{\partial x^3} &= k_1 u' & \text{(upstream)} \\ \mu_2 \frac{\partial u'}{\partial x} - \nu_2 \frac{\partial^2 u'}{\partial x^2} - \nu_2 \frac{\partial^3 u'}{\partial x^3} &= -k_2 u' & \text{(downstream)} \end{aligned} \quad (2.6)$$

where

$$\begin{aligned} \mu_1 &= \nu_{1\infty} + \nu_1, & \mu_2 &= \nu_{2\infty} + \nu_2 \\ k_1 &= \frac{\gamma+1}{2\gamma} \rho_\infty u_\infty (1 - \bar{u}_2) > 0 \\ k_2 &= \frac{\gamma+1}{2\gamma} \rho_\infty u_\infty \frac{1 - \bar{u}_2}{\bar{u}_2} > 0 \end{aligned} \quad (2.7)$$

$\nu_{1\infty}$ and $\nu_{2\infty}$ are the ν values at $\bar{u} = 1$ and \bar{u}_2 , respectively. Obviously, (2.6) is a linear equation whose solution can easily be determined by the following characteristic equations:

$$\begin{aligned} \nu_1 \lambda^3 + \nu_1 \lambda^2 - \mu_1 \lambda + k_1 &= 0 & \text{(upstream)} \\ \nu_2 \lambda^3 + \nu_2 \lambda^2 - \mu_2 \lambda - k_2 &= 0 & \text{(downstream)} \end{aligned} \quad (2.8)$$

The discussion is carried out in the following cases:

(1) μ_1 and μ_2 are greater than zero and $\nu_3 = \nu_4 = 0$. The characteristic root of (2.8) is

$$\lambda = \frac{k_1}{\mu_1} \quad (\text{upstream})$$

$$\lambda = -\frac{k_2}{\mu_2} \quad (\text{downstream})$$

The general solution to (2.6) is:

/15

$$u' = Ae^{\frac{k_1}{\mu_1}x} \quad (\text{upstream})$$

$$u' = Be^{-\frac{k_2}{\mu_2}x} \quad (\text{downstream})$$

Or, one can get from (2.5) that

$$\bar{u} = 1 + Ae^{\frac{k_1}{\mu_1}x} \quad (\text{upstream})$$

$$\bar{u} = \bar{u}_2 + Be^{-\frac{k_2}{\mu_2}x} \quad (\text{downstream}) \quad (2.9)$$

(2.9) shows that the upstream solution smoothly approaches 1 exponentially when $x \rightarrow -\infty$. When $x \rightarrow \infty$, the downstream solution smoothly approaches u_2 without any oscillation.

(2) $\mu_1 > 0$, $\mu_2 > 0$, $v_3 > 0$, and $v_4 = 0$

From (2.8) in the upstream if

$$\frac{\mu_1^2}{k_1 v_3} > 4 \quad (2.10)$$

then both characteristic roots are positive real numbers. The general solution to (2.6) is:

$$\begin{aligned} \bar{u} = & 1 + A_1 \exp \left[\left(\frac{\mu_1}{2v_3} + \frac{1}{2v_3} \sqrt{\mu_1^2 - 4v_3 k_1} \right) x \right] + \\ & + A_2 \exp \left[\left(\frac{\mu_1}{2v_3} - \frac{1}{2v_3} \sqrt{\mu_1^2 - 4v_3 k_1} \right) x \right] \end{aligned} \quad (2.11)$$

Here, A_1 and A_2 are integration constants and the solution does not oscillate. If

$$\frac{\mu_1^2}{k_1 v_3} < 4 \quad (2.12)$$

both characteristic roots of (2.8) are complex numbers.

Therefore, the general solution of (2.6) is:

$$\begin{aligned}\bar{u} = & 1 + A_1 \exp\left(\frac{\mu_1}{2\nu_3} x\right) \cos\left(\frac{1}{2\nu_3} \sqrt{4\nu_3 k_1 - \mu_1^2} x\right) \\ & + A_2 \exp\left(\frac{\mu_1}{2\nu_3} x\right) \sin\left(\frac{1}{2\nu_3} \sqrt{4\nu_3 k_1 - \mu_1^2} x\right)\end{aligned}\quad (2.13)$$

This equation shows that the solution exhibits oscillations in the upstream. Moreover, the amplitude gradually increases with increasing x . Figure 2a shows this change.

In the downstream region, because all characteristic roots of (2.8) are real and $\bar{u} \rightarrow \bar{u}_2$ when $x \rightarrow \infty$, the solution to (2.6) is:

$$\bar{u} = \bar{u}_2 + A \exp\left\{\left[\frac{\mu_2}{2\nu_3} - \frac{1}{2\nu_3} (\mu_2^2 + 4k_2\nu_3)^{\frac{1}{2}}\right] x\right\} \quad (2.14)$$

One can see that the solution does not oscillate.

If we assume that $\mu_1, \mu_2 > 0$, $\nu_3 < 0$ and $\nu_4 = 0$. The solution does not show oscillation upstream as one can see by the same analysis. In the downstream, however, if

$$\frac{\mu_1^2}{k_2 |\nu_3|} < 4$$

the solution shows oscillations (see Figure 2b).

/16



Figure 2a $\mu_1, \mu_2 > 0$, $\nu_3 > 0$ and $\nu_4 = 0$

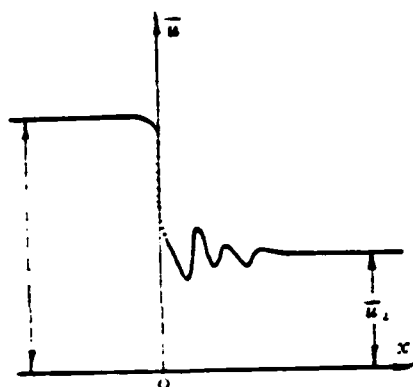


Figure 2b $\mu_1, \mu_2 > 0, v_3 < 0, v_4 = 0$

(3) $v_4 > 0, v_3 = \mu_1 = \mu_2 = 0$

In the upstream region, the characteristic roots, given by (2.8) are:

$$\begin{cases} \lambda_1 = -\left(\frac{k_1}{v_4}\right)^{\frac{1}{3}} \\ \lambda_2 = \lambda_2^{(1)} + \lambda_2^{(2)} i \\ \lambda_3 = \lambda_2^{(1)} - \lambda_2^{(2)} i \end{cases} \quad (2.15)$$

where

$$\begin{cases} \lambda_2^{(1)} = \frac{1}{2} \left(\frac{k_1}{v_4}\right)^{\frac{1}{3}} \\ \lambda_2^{(2)} = \frac{1}{2} \sqrt{3} \left(\frac{k_1}{v_4}\right)^{\frac{1}{3}} \end{cases} \quad (2.16)$$

Considering $\bar{u} \rightarrow 1$ when $x \rightarrow -\infty$, the solution (2.6) is:

$$\bar{u} = 1 + A_1 e^{\lambda_1^{(1)} x} \cos(\lambda_1^{(2)} x) + A_2 e^{\lambda_1^{(1)} x} \sin(\lambda_1^{(2)} x) \quad (2.17)$$

Here, A_1 and A_2 are integration constants. This solution obviously oscillates. Furthermore, the amplitude increases with increasing x (see Figure 3).

For the downstream region, the solution of (2.6) can be obtained similarly:

$$\bar{u} = \bar{u}_1 + B_1 e^{-\lambda_2^{(1)} x} \cos(\lambda_2^{(2)} x) + B_2 e^{-\lambda_2^{(1)} x} \sin(\lambda_2^{(2)} x) \quad (2.18)$$

where

$$\begin{cases} \lambda_2^{(1)} = \frac{1}{2} \left(\frac{k_2}{v_1} \right)^{\frac{1}{2}} \\ \lambda_2^{(2)} = \frac{\sqrt{3}}{2} \left(\frac{k_2}{v_1} \right)^{\frac{1}{2}} \end{cases} \quad (2.19)$$

It shows that the solution also oscillates downstream. Moreover, the amplitude increases with decreasing x (See Figure 3).

(4) v_4 , v_3 , μ_1 and μ_2 simultaneously are present.

/17

Assuming $v_4 > 0$, based on the determination formula of the third order equation one can easily find out that if

$$\frac{(v_1^2 + 3\mu_1 v_4)^2}{\left(v_1^2 + \frac{9}{2} \mu_1 v_1 v_4 + \frac{27}{2} k_1 v_1^2\right)^2} < 1 \quad (2.20)$$

then the solution of (2.6) oscillates upstream. In the downstream area, if

$$\frac{(v_1^2 + 3\mu_1 v_4)^2}{\left(v_1^2 + \frac{9}{2} \mu_1 v_1 v_4 - \frac{27}{2} k_1 v_1^2\right)^2} < 1 \quad (2.21)$$

then the solution of (2.6) also oscillates. From (2.20) and (2.21) one can see that when $v_3 > 0$, $v_4 \neq 0$ and $\mu_1 = \mu_2 = 0$, it always oscillates upstream. In the downstream, however, only when

$$\frac{k_1 v_1^2}{v_1^2} > \frac{4}{27}$$

it exhibits oscillation. If $v_3 < 0$, $v_4 \neq 0$ and $\mu_1 = \mu_2 = 0$, there are always oscillations downstream. Upstream, however, only when

$$\frac{k_1 v_1^2}{|v_1^2|} > \frac{4}{27}$$

it exhibits oscillations (see Figure 4).

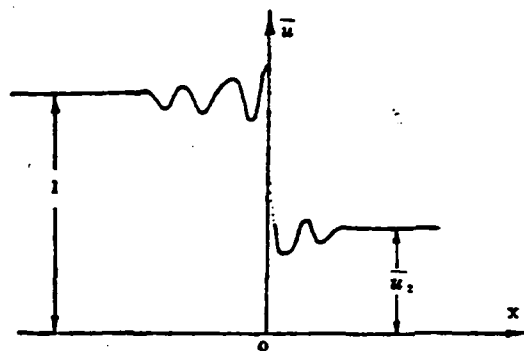


Figure 3. $v_4 > 0$, $v_3 = \mu_1 = \mu_2 = 0$.

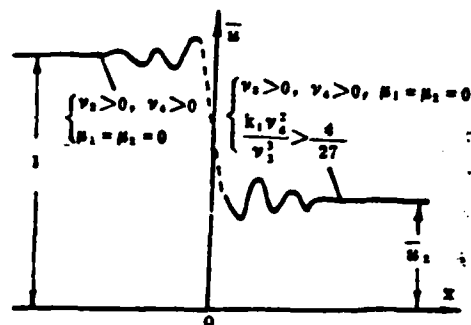


Figure 4. $v_3 > 0$, $v_2 > 0$, $\mu_1 = \mu_2 = 0$

III. Discussion on Upstream and Downstream Shock Wave Oscillation in Difference Calculation

Based on the above analysis, one can see that:

1. In the viscous shock wave propagation equation, a smooth solution can be obtained by adding v_2 alone. The second order diffusion term can smooth shock waves. If second and third order terms are added, when $v_3 > 0$ and

$$\frac{\mu_1^2}{v_1 k_1} < 4$$

the upstream shock wave solution shows oscillations and the downstream solution is smooth. If $v_3 < 0$ and

/18

$$\frac{\mu_1^2}{|v_1| k_1} < 4$$

the downstream solution exhibits oscillations and the upstream solution is smooth. If the fourth order term is added, its effect is to simultaneously cause or aggravate oscillations in the upstream and downstream.

2. Because the second order lattice has a third order dispersion term and a fourth order diffusion term and $v_2 = 0$, the upstream and downstream shock wave exhibits oscillations when $v = 0$ or very small. If the effect of the fourth order diffusion term is far less than that of the third order dispersion term, then one side of the shock wave exhibits larger oscillations depending on the sign of the dispersion term. In order to minimize oscillations, we should try to reduce the third and fourth order terms. For the explicit MacCormack form, if the Courant number approaches 1 and v_3 and v_4 are small, the oscillation should be small. It has already been proven in the numerical experiment in reference [1].

3. The fourth order diffusion term appears because $v_2 = v_3 = 0$ in the third order lattice. Therefore, it is unavoidable to have oscillations in the upstream and downstream shock wave when $v = 0$ or is very small. However, it is generally smaller than the second order oscillation. To further minimize oscillations,

we should reduce one fourth order diffusion term. It is expected that the fourth order lattice only has negligible oscillations in the upstream and downstream because $v_2 = v_3 = v_4 = 0$. The effect of higher order dispersion and diffusion terms is very small.

4. In order to verify the accuracy of these conclusions, we gathered some numerical shock wave experiments in the literature based on the following Burgers equation:

$$\frac{\partial u}{\partial t} + (u+a) \frac{\partial u}{\partial x} = \nu \frac{\partial^2 u}{\partial x^2}$$

Figure 5 is the calculated result given in reference [4] using the first order difference lattice. When $a = 0.038925$, $\nu = 0$ and $x = -\infty$, $u = 2.593467$. When $x = \infty$, $u = 1.393784$. One can see that the shock wave curve is smooth. Figure 6 shows the calculated results given in reference [5] using the explicit MacCormack second order lattice. When $a = 0$, $\nu = 10^{-7}$ and $x = -\infty$, $u = -1$. When $x = \infty$, $u = 1$. One can see that oscillation occurs both upstream and downstream. Figure 7 shows the results given in reference [4] using the third order lattice. The conditions are identical to those in Figure 5. One finds that there are oscillations on either end of the shock wave. However, it is much smaller than that using the second order lattice. Figure 8 shows the results given in reference [6] using the fourth order lattice. When $a = -(1/2)$ and $x = -\infty$, $u = 1$. When $x = \infty$, $u = 0$. The lattice Reynolds' number is 2.5. One can see that there is almost no oscillation in the shock wave. Correspondingly, if the second order lattice is used, oscillations will appear (see [6]).

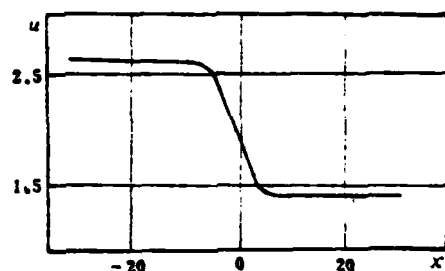


Figure 5. Burgers Equation Shock Wave Solution Given by First Order Difference Lattice[4]

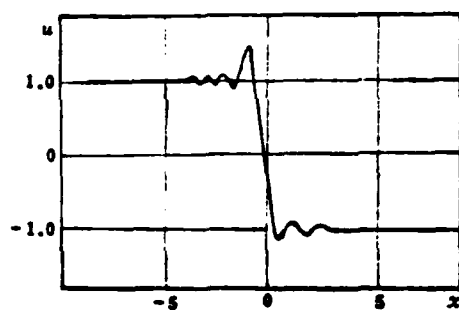


Figure 6. Burgers Equation Shock Wave Solution Given by Second Order MacCormack Lattice[5]

Similar conclusions are derived by numerical simulation of the Euler equation solution of the shock wave^[1,2].

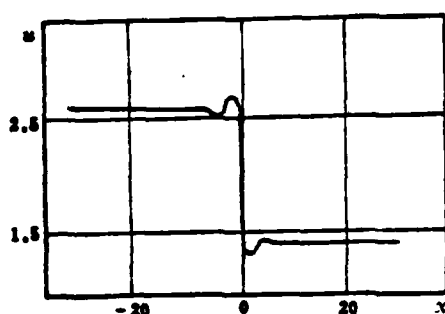


Figure 7. Burgers Equation Shock Wave Solution Given by Third Order Lattice[4]

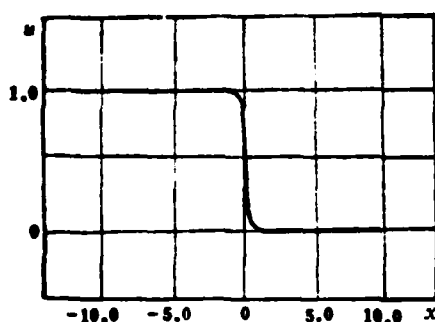


Figure 8. Burgers Equation Shock Wave Solution Given by Fourth Order Lattice[6]

Results of numerical simulation completely confirmed the accuracy of the conclusions. Therefore, the cause of oscillations in upstream and downstream shock wave solutions using a difference method is explained.

During the course of writing this paper, the author discussed with Comrade Gao Shuchun many times. He wishes to express gratitude for his assistance.

References

- [1] Anderson, D.A., J. of Comput. Phys., Vol. 15, No. 1, pp. 1-20, 1984.
- [2] Beam, R.M., and Warming, R.F., J. of Comput. Phys., Vol. 22, No. 1, pp. 87-110, 1976.
- [3] Loytsyanskiy, L.G. Mekhanika Zhidkosti i Gaza, GIFML, Moscow, 1959.
- [4] Rusanov, V.V., Besmenov, I. V., Nazhestkina, E.I., Lecture notes in Physics, 170, pp. 455-460, 1982.
- [5] Wu Huamo and Yang Mingling, A Concept of Structuring a Steady Difference Lattice, High Speed Aerodynamic Calculation, Computer Center, Chinese Academy of Science, 1978.
- [6] Graves, R.A., NASA TN D-8021, 1975.

THE EXPLORATION OF THE SPATIAL OSCILLATIONS IN FINITE DIFFERENCE SOLUTIONS FOR NAVIER-STOKES SHOCKS

Zhang Hanxin

(China Aerodynamic Research and Development Centre)

In this paper, the spatial oscillations in finite difference solutions for Navier-Stokes shocks are explored. It is shown that the second order diffusion term added to NS equations could smear the shock wave, damp the oscillations in the vicinity of the shock. However, the third order dispersion term and fourth order diffusion term added to NS equations could cause the oscillations in upstream and downstream region of the shock under the conditions given by this paper. Therefore the oscillations in the difference solutions with second or third order accuracy could arise from the numerical dispersion and diffusion terms.

Calculation of Boundary Layer Growth Behind An Unsteady Expansion Wave in a Tube

Wang Songgao

(Institute of Mechanics, Chinese Academy of Sciences)

I. Introduction

In order to improve the operating quality of wind tunnels and shock wave tubes, the study of boundary layer growth after an expansion wave enters a cylindrical tube is of significance. Especially in transonic wind tunnels, the boundary layer growth in the gas storage tube with time will directly affect the operating time and flow quality of the tunnel. To solve this problem is the basis of wind tunnel design.

E. Becker^[1] first calculated the boundary layer growth in the gas storage tube. He used the two element incompressibility assumption and the 1/7th power velocity distribution to simplify the boundary layer momentum integral. Then, the solution was found by using the Blasius skin friction law. Furthermore, an effective central expansion wave velocity was obtained. Although the effect of compressibility and heat transfer on ρ/ρ_c was considered in the boundary layer and the skin friction coefficient, the result is still incompressible. H. Ludwig [2] modified the Becker method for the velocity cross-section and skin friction coefficient to obtain better results.

J.C. Sivells' work^[3] pointed out that corrections must be made in axisymmetry, skin friction coefficient, velocity cross-section and effective expansion wave origin. Becker's effective expansion wave propagation speed could still be used. In his calculation, two modifications were made: one is to modify the result of a flat plate and the other is to correct the origin of the effective expansion wave according to the start-up time of the experiment. A numerical method was used in the calculation.

We began directly from the unsteady axisymmetric boundary layer momentum integral to find the boundary layer growth in and

behind the expansion wave assuming that the steady state boundary layer velocity cross-section and skin friction could be applied to an unsteady boundary layer, and the axial pressure gradient of the nuclear flow in the tube is negligible. Finally, the formulas to calculate the effective expansion wave propagation speed and boundary layer thickness were found. These formulas are in algebraic expressions. In the binary incompressible case, Becker's results are obtained. The computation process is simple. It is in good agreement with the experimental result.

For engineering design, modification of the origin of the effective expansion wave can be skipped.

II. Basic Equation and Its Solution

The unsteady boundary layer momentum integral for a tube is:

/21

$$\begin{aligned} \frac{\partial \theta}{\partial x} + \frac{1}{u_e} \frac{\partial u_e}{\partial x} (2\theta + \delta^*) + \theta \left(\frac{1}{\rho_e} \frac{\partial \rho_e}{\partial x} + \frac{1}{r_0} \frac{dr_0}{dx} \right) + \\ + \frac{1}{\rho_e u_e} \frac{\partial}{\partial t} (\rho_e u_e \delta^*) - \frac{1}{\rho_e u_e} \frac{\partial}{\partial t} (\rho_e \delta_e) = \frac{1}{2} c_f \end{aligned} \quad (1)$$

where

$$\left. \begin{aligned} \theta &= \int_0^{\delta} \left(1 - \frac{y}{r_0} \right) \frac{\rho u}{\rho_e u_e} \left(1 - \frac{u}{u_e} \right) dy \\ \delta^* &= \int_0^{\delta} \left(1 - \frac{y}{r_0} \right) \left(1 - \frac{\rho u}{\rho_e u_e} \right) dy \\ \delta_e &= \int_0^{\delta} \left(1 - \frac{y}{r_0} \right) \left(1 - \frac{\rho}{\rho_e} \right) dy \end{aligned} \right\} \quad (2)$$

Here, ρ , u and r_0 are the density, flow velocity and inner radius of the tube. The subscript e represents the free flow direction of the boundary layer. c_f is the skin friction coefficient. x is the axial coordinate and its positive direction coincides with the propagation direction of the expansion wave. y is the radial coordinate which points from the wall toward the center. t is time.

From

$$\begin{aligned} \frac{1}{u_e} \frac{\partial u_e}{\partial x} \delta^* + \frac{1}{u_e^2} \delta^* \frac{\partial u_e}{\partial t} &= \frac{\delta^*}{u_e} \left(u_e \frac{\partial u_e}{\partial x} + \frac{\partial u_e}{\partial t} \right) \\ &= -\frac{\delta^*}{\rho_e u_e^2} \frac{\partial p}{\partial x} = 0 \end{aligned}$$

Equation (1) can be converted into:

$$\frac{\partial \theta}{\partial x} + 2 \frac{\theta}{u_e} \frac{\partial u_e}{\partial x} + \frac{\theta}{\rho_e} \frac{\partial \rho_e}{\partial x} + \frac{1}{\rho_e u_e} \frac{\partial}{\partial t} (\rho_e \delta^* - \rho_e \delta_e) = \frac{1}{2} c, \quad (3)$$

Substituting the power law velocity distribution into equation (2), we get

$$\begin{aligned} \Delta \equiv \frac{\delta^* - \delta_e}{\theta} &= \frac{\frac{2}{n+2} \left[1 - \frac{n}{2(n+1)} \frac{T_e}{T_w} \right] - \frac{\delta}{r_0} \frac{1}{2(2n-1)} \left(1 - \frac{n}{2n+1} \frac{T_e}{T_w} \right) -}{\frac{n}{(n+1)(n+2)} \left[\frac{T_e}{T_w} + \left(1 - \frac{T_e}{T_w} \right) \frac{n+1}{n+3} \right] -} \\ &\quad \frac{- \left(1 - \frac{T_e}{T_w} \right) \left[\frac{1}{n+1} - \frac{\delta}{r_0} \frac{1}{2(2n+1)} \right]}{- \frac{n}{(2n+1)(2n+2)} \frac{\delta}{r_0} \left[\frac{T_e}{T_w} + \left(1 - \frac{T_e}{T_w} \right) \frac{2n+1}{2n+3} \right]} \end{aligned}$$

When $n \rightarrow \infty$, the above formula approaches 1. When $n = 7 \sim 11$, the change caused by $(T_e/T_w) = 0.8 \sim 1.0$ and $(\delta/r_0) = 0 \sim 1$ is around 4%. The entire change is approximately 8%. Because we assumed that Δ is a constant, equation (3) can be rewritten as:

$$\frac{\partial \theta}{\partial x} + \theta \left(\frac{2}{u_e} \frac{\partial u_e}{\partial x} + \frac{1}{\rho_e} \frac{\partial \rho_e}{\partial x} \right) + \frac{\Delta}{\rho_e u_e} \frac{\partial}{\partial t} (\rho_e \theta) = \frac{1}{2} c, \quad (4)$$

Let

$$\phi = \frac{\rho_e u_e}{\rho_e u_e} \theta \quad (5)$$

The subscript 4 represents the gas storage state. Equation (4) is converted into

$$\frac{\partial \phi}{\partial x} + \frac{\phi}{u_e} \frac{\partial u_e}{\partial x} + \frac{\Delta}{u_e} \left(\frac{\partial \phi}{\partial t} - \phi \frac{\partial u_e}{\partial t} \right) = \frac{1}{2} \frac{\rho_e u_e}{\rho_e u_e} c, \quad (6)$$

Equation (6) is the basic equation of this discussion.

Generally, an unsteady expansion wave is a wave series of finite thickness. The boundary layer growth in the wave and behind the wave should be separately discussed. The two solutions are linked together at the tail of the wave. Figure 1 illustrates this situation. In the following, we will discuss

in two separate situations and then combine them together.

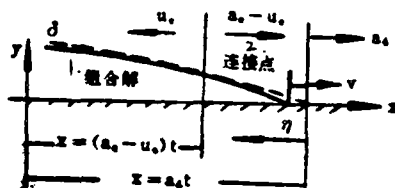


Figure 1. Schematic Diagram of Boundary Layer Growth

1. composite solution
2. connecting point

(1) Central Wave

When the thickness of an unsteady expansion wave is zero, the nuclear flow parameters p_e and u_e in the tube behind the wave are invariant. Equation (6) can be simplified as:

$$\frac{\partial \theta}{\partial x} + \frac{\Delta}{u_s} \frac{\partial \theta}{\partial t} = \frac{1}{2} c, \quad (7)$$

According to the theory of partial differential equation, we can obtain the characteristic equations for equation (7):

$$\left. \begin{aligned} \frac{dx}{ds} &= 1 \\ V \frac{dt}{ds} &= V \frac{\Delta}{u_r} \\ \frac{d\theta}{ds} &= \frac{1}{2} c_r \end{aligned} \right\} \quad (8)$$

Here, V represents the propagating speed of a central expansion wave. From the above formula, we can obtain an equivalent differential equation for equation (7):

$$\left(1 - \frac{V}{u_*} \frac{\delta^* - \delta_p}{\theta}\right) \frac{d\theta}{dX} = \frac{1}{2} c, \quad (9)$$

where

$$X = x - Vt$$

After ascertaining $c_f = c_f(\theta)$, equation (9) can be solved.

(2) Inside the Wave

Let

$$\left. \begin{aligned} \xi &= x \\ \eta &= 1 - \frac{x}{a_* t} \end{aligned} \right\} \quad (10)$$

Here, a is the speed of sound. The subscript 4 represents the gas storage state. We get

$$\left. \begin{aligned} \frac{\partial}{\partial x} &= \frac{\partial}{\partial \xi} - \frac{1-\eta}{\xi} \frac{\partial}{\partial \eta} \\ \frac{1}{a_*} \frac{\partial}{\partial t} &= \frac{(1-\eta)^2}{\xi} \frac{\partial}{\partial \eta} \end{aligned} \right\} \quad (11)$$

When $\gamma = 1.4$, the correlation between parameters inside an unsteady expansion wave and those in front of the wave is^[1]:

$$\left. \begin{aligned} \frac{u_*}{a_*} &= -\frac{5}{6} \eta \\ \frac{\rho_*}{\rho_*} &= \left(1 - \frac{1}{6} \eta\right)^3 \end{aligned} \right\} \quad (12)$$

We have

$$\left. \begin{aligned} \frac{\partial}{\partial \xi} \left(\frac{u_*}{a_*} \right) &= 0 \\ \frac{\partial}{\partial \eta} \left(\frac{u_*}{a_*} \right) &= -\frac{5}{6} \end{aligned} \right\} \quad (13)$$

The viscosity was approximated by the Sutherland formula^[1]:

/23

$$\frac{\mu_*}{\mu_*} = 1 - 0.28\eta \quad (14)$$

Using the above formulas, equation (6) can be written as:

$$\begin{aligned} & \frac{1-\eta}{\xi} \frac{\partial \phi}{\partial \eta} \left(1 + \frac{6\Delta}{5} \frac{1-\eta}{\eta}\right) - \frac{\partial \phi}{\partial \xi} + \frac{1-\eta}{\xi \eta} \phi \left(1 - \frac{6\Delta}{5} \frac{1-\eta}{\eta}\right) \\ & = \frac{5}{12} \eta \left(1 - \frac{1}{6} \eta\right)' c, \end{aligned} \quad (15)$$

Because $Re_\theta = \frac{\rho_e u_e \theta}{\mu_e} = \phi \frac{\rho_4 a_4}{\mu_4} \frac{\mu_4}{\mu_e} = f(\phi, \eta)$, and $c_f = c_f(\phi, \eta)$ in equation (15), the characteristic equation set for equation (15) is

$$\left. \begin{aligned} \frac{d\xi}{ds} &= -1 \\ \frac{d\eta}{ds} &= \frac{1-\eta}{\xi} \left(1 + \frac{6\Delta}{5} \frac{1-\eta}{\eta}\right) \\ \frac{d\phi}{ds} + \frac{1-\eta}{\xi \eta} \phi \left(1 - \frac{6\Delta}{5} \frac{1-\eta}{\eta}\right) &= \frac{5}{12} \eta \left(1 - \frac{1}{6} \eta\right)' c, \end{aligned} \right\} \quad (16)$$

From the two equations above, we get

$$\frac{d\xi}{\xi} = \frac{-\eta d\eta}{(1-\eta) \left[\frac{6\Delta}{5} + \left(1 - \frac{6\Delta}{5}\right) \eta\right]} = - \left[\frac{1}{1-\eta} - \frac{1}{1 - \left(1 - \frac{5}{6\Delta}\right) \eta} \right] d\eta$$

The solution is
$$\frac{\xi}{1-\eta} = c \left[1 - \left(1 - \frac{5}{6\Delta}\right) \eta \right]^{\frac{5}{6\Delta}-1} \quad (17)$$

The constant c can be determined later.

From $d\phi/ds = d\phi/d\eta \cdot d\eta/ds$ and equation (17), the equivalent normal differential equation for equation (15) is:

$$\frac{d\phi}{d\eta} - \frac{\phi}{\eta} \frac{1 - \left(1 + \frac{5}{6\Delta}\right) \eta}{1 - \left(1 - \frac{5}{6\Delta}\right) \eta} = \frac{25}{72} c \eta' \left(1 - \frac{1}{6} \eta\right)' \left[1 - \left(1 - \frac{5}{6\Delta}\right) \eta \right]^{\frac{5}{6\Delta}-1} c, \quad (18)$$

After c_f is determined, $\phi = \phi(\eta)$, i.e., $\theta = \theta(\eta)$, can be determined.

(3) Composite Solution

Strictly speaking, the boundary layer growth process should be solved inside and outside the wave as shown in Figure 1. The complete solution is obtained by combining the two solutions at the end of the wave. Obviously, solving equation (18) is most of

the work. We can assume a composite solution: to find an equivalent expansion wave of zero thickness which results in the same boundary layer thickness at the tail end of the wave at the same time as that in equation (18). We used such a zero thickness expansion wave to find a universal solution. In fact, it is a problem to find the propagating speed V of an equivalent central wave.

Assuming that the friction coefficient law is normal:

/24

$$c_f = k(Re_\theta)^{-m} \quad (19)$$

k is a constant and the subscript θ represents taking Re with respect to θ .

Substituting it into equation (9), we get the solution

$$-\theta^{m+1} = \frac{k}{2} (1+m) \frac{Vt-x}{\left(\frac{\rho_e u_e}{\mu_e}\right)^m \left(1 - \frac{V}{u_e} \Delta\right)} \quad (20)$$

$$\frac{1}{1+m} \left(\frac{\rho_e a_e}{\mu_e}\right)^{m+1} \frac{\mu_e}{\rho_e u_e} \phi^{m+1} = \frac{k}{2} a_{e,t} \frac{1 - \frac{V}{a_e} - \eta}{1 - \frac{V}{u_e} \Delta}$$

By substituting the unsteady expansion wave correlation into it, we get:

$$\frac{1}{1+m} \left(\frac{\rho_e a_e}{\mu_e}\right)^{m+1} \phi^{m+1} = \frac{5}{12} k a_{e,t} \eta^2 \left(1 - \frac{\eta}{6}\right)^2 (1 - 0.28\eta)^2 \left(\frac{1 - \frac{V}{a_e} - \eta}{\eta + \frac{6}{5} \frac{V}{a_e} \Delta}\right) \quad (21)$$

At the tail $\eta = \eta_1 = \frac{\gamma + 1}{2} M_3$, generally, $M_3 < 0.30$ which

means $\eta_1 < 0.34$. η_1 is a small quantity. After keeping the lowest order term on the right side of equation (21), we get:

$$\frac{1}{1+m} \left(\frac{\rho_e a_e}{\mu_e}\right)^{m+1} \phi_1^{m+1} = \frac{25}{72} k a_{e,t} \frac{1 - \frac{V}{a_e}}{\frac{V}{a_e} \Delta} \eta_1^2 \quad (22)$$

The subscript 1 represents the wave tail.

Corresponding to equation (18), we get

$$\begin{aligned} \frac{d\phi^{n+1}}{d\eta} - (1+m) \frac{\phi^{n+1}}{\eta} \frac{1 - \left(1 + \frac{5}{6\Delta}\right)\eta}{1 - \left(1 - \frac{5}{6\Delta}\right)\eta} \\ = \frac{25}{72} (1+m) ck (1 - 0.28\eta)^n \frac{\left(1 - \frac{\eta}{6}\right)^5 \eta^2}{\left(\frac{\rho_1 a_1}{\mu_1}\right)^n \left[1 - \left(1 - \frac{5}{6\Delta}\right)\eta\right]^{2 - \frac{5}{6\Delta}}} \end{aligned}$$

The solution is

$$\begin{aligned} \frac{1}{1+m} \left(\frac{\rho_1 a_1}{\mu_1}\right)^n \phi^{n+1} = \frac{25}{72} ck e^{(1+m)\eta} \int \frac{1 - \left(1 + \frac{5}{6\Delta}\right)\eta}{1 - \left(1 - \frac{5}{6\Delta}\right)\eta} \frac{\eta^2}{\eta^2} \times \\ \times \left\{ \int_0^\eta \frac{(1 - 0.28\eta)^n \left(1 - \frac{\eta}{6}\right)^5 \eta^2}{\left[1 - \left(1 - \frac{5}{6\Delta}\right)\eta\right]^{2 - (5/6\Delta)}} e^{-(1+m)\eta} \frac{\eta^2}{\eta^2} d\eta \right\} \quad /25 \end{aligned} \quad (23)$$

At the tail of the wave:

$$\begin{aligned} \frac{1}{1+m} \left(\frac{\rho_1 a_1}{\mu_1}\right)^n \phi_1^{n+1} = \frac{25}{72} ck \left[\eta_1^{1+n} - (1+m) \frac{5}{3\Delta} \eta_1^{n+1} \right] \times \\ \times \int_0^{\eta_1} (1 - 0.28m\eta) \left(1 - \frac{5}{6}\eta\right) \eta^2 \left[\eta_1^{-(1+m)} + (1+m) \frac{5}{3\Delta} \eta^{-n} \right] d\eta \quad (24) \\ \approx \frac{25}{72} ck \frac{\eta_1^2}{2-m} \end{aligned}$$

From $\xi/1-\eta = a_4 t$, we can specify that $c = a_4 t [1 - (1 - 5/6\Delta)\eta]^{1-5/6\Delta}$. Substituting it into the above equation and keeping the lowest order term in η_1 , we get:

$$\frac{1}{1+m} \left(\frac{\rho_1 a_1}{\mu_1}\right) \phi_1^{n+1} = \frac{25}{72} a_4 t k \frac{\eta_1^2}{2-m} \quad (25)$$

Comparing (22) to (25) we get:

i.e.,

$$\frac{V}{a_s} \Delta \frac{\eta_1}{2-m} = 1 - \frac{V}{a_s} \quad (26)$$

or

$$\frac{V}{a_s} = \left(1 + \frac{\delta^* - \delta_p}{\theta} \frac{\eta_1}{2-m} \right)^{-1}$$

$$\frac{V}{a_s} = 1 - \frac{\delta^* - \delta_p}{\theta} \frac{\eta_1}{2-m} \quad (27)$$

When the flow is binary and incompressible and $n = 7$, $m = 1/4$, $\Delta = n+2/n = 9/7$.

$$\frac{V}{a_s} = \left(1 + \frac{36}{49} \eta_1 \right)^{-1} \approx 1 - \frac{2}{3} \eta_1 \quad (28)$$

This is Becker's result^[3]. Strictly speaking, the propagating speed V of the axisymmetric effective central expansion wave is also related to the velocity cross-section and the law of skin friction in first order approximation.

III. Results and Discussion

For convenience, we take the absolute value of u_e . Then, equation (9) can be rewritten as:

$$\left(1 + \frac{V}{u_e} \frac{\delta^* - \delta_p}{\theta} \right) \frac{d\theta}{dX} = \frac{1}{2} c_f \quad (29)$$

where

$$X = Vt - x \quad (30)$$

$$\frac{V}{a_s} = 1 - \frac{1}{2-m} \frac{\delta^* - \delta_p}{\theta} \frac{(\gamma+1)M_1}{2+(\gamma-1)M_1} \quad (31)$$

$$\frac{V}{u_e} = \frac{1}{M_1} + \frac{\gamma-1}{2} - \frac{\gamma+1}{2(2-m)} \frac{\delta^* - \delta_p}{\theta} \quad (32)$$

As long as c_f is determined, the solution can be found. /26

We noticed that the value of $1/2-m$ varies by about 3% when $m = 1/4 \sim 1/7$. We also assumed that $\delta^* - \delta_p / \theta$ is a constant (although the not too large variation of $\delta^* - \delta_p / \theta$ is included in the calculation), equation (26) or (27) may be considered invariant in approximation. Therefore, the assumption that

$$\frac{V}{a_i} \approx 1 - \frac{2}{3} \eta_i = 1 - \frac{\left(\frac{\gamma+1}{3}\right) M_i}{1 + \left(\frac{\gamma-1}{2}\right) M_i} \quad (33)$$

is not related to the specific laws of velocity cross-section and skin friction in reference [3] is still valid (approximately) in axisymmetric conditions. In the normal range, the difference in the values of (31) and (33) is less than 10%.

Equations (29) to (32) are our starting equations. For simplicity, equations (31) and (32) can be approximated by the corresponding Becker's result.

Let us take the Karman modified friction coefficient expression

$$c_f = \frac{(0.242)^2}{(\lg Re_s + 1.1696)(\lg Re_s + 0.3010)} \left(1 + \frac{\gamma-1}{2} M_i^2\right)^{-0.447} \quad (34)$$

and substitute it into equation (29) to obtain the boundary layer thickness by integration:

$$\delta = \frac{0.0293(Vt-x)}{\frac{\theta}{\delta} + \frac{V}{u_s} \frac{\delta^* - \delta_p}{\theta}} [\lg(2Re_s)]^{-1} \left(1 + \frac{\gamma-1}{2} M_i^2\right)^{-0.447} \quad (35)$$

Subsequently, the expressions for θ/δ , δ^*/δ and δ_p/δ are found. After reorganization, the above formula can be written as:

$$C = B\left(\frac{\delta}{r_s}\right) - A\left(\frac{\delta}{r_s}\right)^2 \quad (36)$$

where

$$\left. \begin{aligned} A &= \frac{n}{(2n+2)(2n+3)} \left(1 + \frac{2}{2n+1} \frac{T_s}{T_w}\right) + \frac{V}{u_s} \frac{n}{(2n+1)(2n+2)} \left(1 + \frac{1}{n} \frac{T_s}{T_w}\right) \\ B &= \frac{n}{(n+2)(n+3)} \left(1 + \frac{2}{n+1} \frac{T_s}{T_w}\right) + \frac{V}{u_s} \frac{n}{(n+1)(n+2)} \left(1 + \frac{2}{n} \frac{T_s}{T_w}\right) \\ C &= \frac{0.0293(Vt-x)}{r_s [\lg(2Re_s)]^2 \left(1 + \frac{\gamma-1}{2} M_i^2\right)^{0.447}} \end{aligned} \right\} \quad (37)$$

If $T_e/T_w = 1$, the above formula can be further simplified. Obviously, the computation is simple.

Figures 2 and 3 are the calculated results.

Figure 2 is a comparison of the calculated results with experimental values in wind tunnels. They agree very well. Results calculated by Ludwig are also shown in the figure.

127

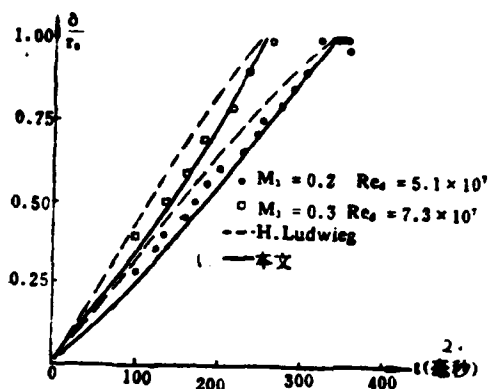


Figure 2. Comparison and Calculated Results

1. this work
2. t (microsecond)

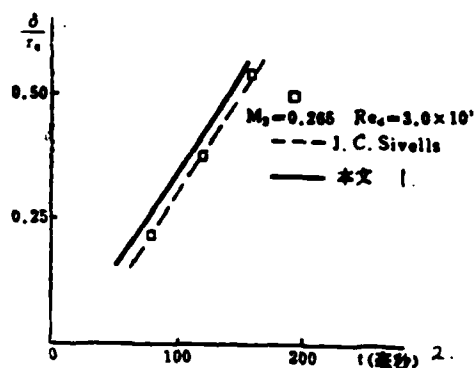


Figure 3. Comparison and Calculated Results

1. this work
2. t (microsecond)

Figure 3 is the comparison of our calculated results with the experimental wind tunnel values at Arnold Engineering Development Center (AEDC). The calculated results deviate from the experimental values by a certain moment. In the figure, the modified result in reference [3] is also given. Sivells used the start-up time of the experiment to modify the effective origin. This is to add another time correction. When the starting device is located downstream from the wind tunnel, this correction could improve the agreement with experimental values. However, this correction could not be obtained ahead of time in engineering. Numerically, this correction value would not bring about a large error for design purposes. It could be neglected. Of course, it is ideal to determine this correction in theory.

In summary, it is possible to theoretically calculate the boundary layer growth behind an unsteady expansion wave in a cylindrical tube by using the composite solution of an effective central wave propagating at a speed V directly from the unsteady axisymmetric boundary layer momentum integral with some assumptions. The effective velocity V has been found. Within a certain error range, it is not related to the velocity cross-section and the law of skin friction. Becker's result is a special case obtained in a binary incompressible system when $n = (1/7)$ and $m = (1/4)$. The composite solution is an algebraic expression which is easy to calculate. The results are in good agreement with the experiments. For engineering design purposes, the accuracy is sufficient.

References

- [1] Becker, E., Ingenieur Archiv, 25, 155-163 (1957).
- [2] Ludwig, H., et al., AGARD-CP-174 (1976).
- [3] Sivells, J.C., AEDC-75-118 (1975).

CALCULATION OF THE BOUNDARY LAYER GROWTH BEHIND AN UNSTEADY EXPANSION WAVE IN A TUBE

Wang Songgao

(Institute of Mechanics, Academia Sinica)

Abstract

The problem of the boundary layer growth in the charge tube is discussed. Based on E. Becker's work and J. C. Sivells' modification, in the axisymmetric case, a theoretical treatment of the boundary layer growth in the expansion wave is given; the movement velocity of the equivalent unsteady expansion wave of zero width is derived; an analytical solution is obtained and has been reduced to an algebraical expression. The result contains various factors which affect boundary layer growth, axisymmetry, velocity profile, skin-friction coefficient law and expansion wave thickness effect. The calculation is simple and the results coincide with experiments.

Numerical Computation for Inviscid Supersonic Flow
Around a Bent Cone

Ji Chuqun

(Beijing Institute of Aerodynamics)

Abstract

In this work, a computation method for inviscid supersonic flow around a bent cone was developed using a difference method. In order to overcome the difficulty brought about by the bent body axis in the calculation, the equation solving place is transformed into an inclined plane in the advancing direction through the Euler transformation of the independent variables. In other words, an "inclined shift" or "parallel shift" of the Euler equation was used to solve the problem. Numerical examples showed that good results could be obtained using this method.

I. Introduction

This numerical method for the characteristics of an inviscid supersonic flow around a bent cone was based on a difference method and the shock wave capturing technique with the following essential points. (1) In order to overcome the difficulty due to the bent cone axis, the independent variables of the Euler equation are transformed onto an inclined solving plane which is the same direction as the thrust. Moreover, the angle of inclination gradually increases or decreases as the computation progresses. In other words, the numerical solution of the Euler equation is found by the "inclined advance" with a varying angle of inclination or "parallel advance" using right inclined angle. Its advantage is that the calculation can advance in a rational direction according to the specific shape of the object to simplify the calculation and to ensure the accuracy. (2) The second order two-step MacCormack scheme is used. (3) The computation area is divided into two parts by a transformation plane (see Figure 1). The part in front of the plane uses the

front cone cylindrical coordinate to solve the Euler equation by "inclined advance". The part behind the plane uses the rear cone cylindrical coordinate to solve the Euler equation by "parallel advance". (4) The computation formulas for the external shock wave and the boundary are derived from the shock wave correlation and the boundary compatibility relations, respectively. (5) The flow characteristics of singular points on the intersect of the front and rear cone surface are solved individually. The position of internal shock wave is derived from the pressure change in the flow field. No filtering and smoothing process is included in the calculation. (6) A non-uniform radial lattice is used so that the number of meshes is increased near the surface without increasing the total number of meshes.

II. Basic Equations and Boundary Conditions

The coordinate system, attack angle α , and sideslip angle β used in the computation are defined in Figure 1. Different equations were used in the "inclined advance" and "parallel advance" areas for solving the Euler equation. In the latter case, the conserved Euler equation is used. The specific computation method is shown in reference [2]. In the following, the equation in the "inclined advance" region and its boundary conditions are given.

1. Points in the Flow Field

In a cylindrical coordinate (z, r, ϕ) , the aerodynamic equation for a steady inviscid and thermally non-conductive flow is:

received on May 16, 1983, revised on Oct. 19

$$\begin{aligned}
u \frac{\partial u}{\partial z} + v \frac{\partial u}{\partial r} + \frac{w}{r} \frac{\partial u}{\partial \phi} + \frac{1}{\rho} \frac{\partial p}{\partial z} &= 0 \\
u \frac{\partial v}{\partial z} + v \frac{\partial v}{\partial r} + \frac{w}{r} \frac{\partial v}{\partial \phi} + \frac{1}{\rho} \frac{\partial p}{\partial r} - \frac{w^2}{r} &= 0 \\
u \frac{\partial w}{\partial z} + v \frac{\partial w}{\partial r} + \frac{w}{r} \frac{\partial w}{\partial \phi} + \frac{1}{\rho r} \frac{\partial p}{\partial \phi} + \frac{vw}{r} &= 0 \\
u \frac{\partial \rho}{\partial z} + v \frac{\partial \rho}{\partial r} + \frac{w}{r} \frac{\partial \rho}{\partial \phi} + \rho \left(\frac{\partial u}{\partial z} + \frac{\partial v}{\partial r} + \frac{1}{r} \frac{\partial w}{\partial \phi} \right) + \frac{\rho v}{r} &= 0 \\
u \frac{\partial p}{\partial z} + v \frac{\partial p}{\partial r} + \frac{w}{r} \frac{\partial p}{\partial \phi} - a^2 \left(u \frac{\partial \rho}{\partial z} + v \frac{\partial \rho}{\partial r} + \frac{w}{r} \frac{\partial \rho}{\partial \phi} \right) &= 0
\end{aligned} \tag{1}$$

The pressure p , density ρ , speed of sound a , and velocity components u , v , w are dimensionless. The dimension factors are $\rho_\infty, V_\infty^2, \rho_\infty$ and V_∞ . In order to change the solving plane of equation (1) from $z = \text{const}$ to an inclined plane $\eta(z, r, \phi) = \text{const}$ (with respect to z -axis), new variables η , ξ , and φ are introduced in the following equation.

$$\begin{aligned}
z &= E(r, \eta, \psi) = \eta + r(A + B\eta) \cos \psi \\
r &= f_1(\eta, \psi) + \xi[f_1(\eta, \psi) - f_2(\eta, \psi)] \\
\phi &= \psi
\end{aligned} \tag{2}$$

where

$$\begin{aligned}
A &= \text{ctg } \theta_0 - \frac{\eta_0}{\eta^* - \eta_0} (\text{ctg } \theta^* - \text{ctg } \theta_0) \\
B &= \frac{1}{\eta^* - \eta_0} (\text{ctg } \theta^* - \text{ctg } \theta_0)
\end{aligned}$$

where η_0 and θ_0 the initial values of η and angle of inclination of the front cone flow field solution. η^* and θ^* represent the η value and angle of inclination of the transformation plane (see Figure 1). $f_1(\eta, \varphi)$ and $f_2(\eta, \varphi)$ represent the external shock wave boundary and object boundary [$r=f_1(\eta, \varphi)$, $r=f_2(\eta, \varphi)$],

respectively.

By using the transformation correlation (2), equation (1) finally becomes

$$\frac{\partial p}{\partial \eta} = \frac{\rho a^2 \left[G_1 \eta_1 + G_2 \eta_2 + G_3 \left(\frac{1}{r} \eta_3 \right) \right] - e (a^2 G_1 + G_2)}{a^2 \left[\eta_1^2 + \eta_2^2 + \left(\frac{1}{r} \eta_3 \right)^2 \right] - e^2}$$

$$\frac{\partial \rho}{\partial \eta} = \frac{- \left(G_1 - e \cdot \frac{\partial p}{\partial \eta} \right)}{a^2 e} \quad (3)$$

$$\frac{\partial u}{\partial \eta} = \frac{1}{e} \left(G_1 - \frac{1}{\rho} \eta_1 \frac{\partial p}{\partial \eta} \right)$$

$$\frac{\partial v}{\partial \eta} = \frac{1}{e} \left(G_2 - \frac{1}{\rho} \eta_2 \frac{\partial p}{\partial \eta} \right)$$

$$\frac{\partial w}{\partial \eta} = \frac{1}{e} \left(G_3 - \frac{1}{\rho r} \eta_3 \frac{\partial p}{\partial \eta} \right)$$

where

/31

$$G_1 = - \left[n \frac{\partial \rho}{\partial \xi} + \frac{w}{r} \frac{\partial \rho}{\partial \psi} + \rho \left(\xi_1 \frac{\partial u}{\partial \xi} + \xi_2 \frac{\partial v}{\partial \xi} + \frac{1}{r} \xi_3 \frac{\partial w}{\partial \xi} + \frac{1}{r} \frac{\partial w}{\partial \psi} \right) + \frac{\rho v}{r} \right]$$

$$G_2 = - n \frac{\partial u}{\partial \xi} - \frac{w}{r} \frac{\partial u}{\partial \psi} - \frac{1}{\rho} \xi_1 \frac{\partial \rho}{\partial \xi}$$

$$G_3 = - n \frac{\partial v}{\partial \xi} - \frac{w}{r} \frac{\partial v}{\partial \psi} - \frac{1}{\rho} \xi_2 \frac{\partial \rho}{\partial \xi} + \frac{w^2}{r}$$

$$G_4 = - \left[n \frac{\partial w}{\partial \xi} + \frac{w}{r} \frac{\partial w}{\partial \psi} + \frac{1}{\rho r} \left(\xi_3 \frac{\partial \rho}{\partial \xi} + \frac{\partial \rho}{\partial \psi} \right) + \frac{v w}{r} \right]$$

$$G_5 = - \left[n \frac{\partial \rho}{\partial \xi} + \frac{w}{r} \frac{\partial \rho}{\partial \psi} - a^2 \left(n \frac{\partial \rho}{\partial \xi} + \frac{w}{r} \frac{\partial \rho}{\partial \psi} \right) \right]$$

$$e = \bar{\eta} \cdot \bar{V} = \eta_1 u + \eta_2 v + \frac{1}{r} \eta_3 w$$

$$n = \bar{\xi} \cdot \bar{V} = \xi_1 u + \xi_2 v + \frac{1}{r} \xi_3 w$$

$$\eta_1 = \frac{\partial \eta}{\partial z} = \frac{1}{E_1}$$

$$\eta_2 = \frac{\partial \eta}{\partial r} = - \frac{E_2}{E_1}$$

$$\frac{1}{r} \eta_* = \frac{1}{r} \frac{\partial \eta}{\partial \phi} = -\frac{E_*}{r E_*}$$

$$E_* = \frac{\partial E(\eta, r, \psi)}{\partial \eta} = 1 + r \cos \psi \cdot B$$

$$E_r = \frac{\partial E(\eta, r, \psi)}{\partial r} = (A + B\eta) \cos \psi$$

$$\frac{1}{r} E_* = \frac{1}{r} \cdot \frac{\partial E(\eta, r, \psi)}{\partial \psi} = -\frac{1}{r} (A + B\eta) \sin \psi$$

Equation (3) is the formula to calculate a point in the "inclined advance" solving region. When the solving plane advances from η_0 to η^* , its angle of inclination with the z-axis also gradually changes from θ_0 to θ^* .

2. Shock Wave and Characteristic Compatibility

According to an analysis of the shock wave boundary characteristics, the only characteristic compatibility in calculating the shock wave point is the Porter I family compatibility relation.

$$\rho a \left[\left(e \frac{\partial u}{\partial \eta} + \frac{1}{\rho} \eta_* \frac{\partial p}{\partial \eta} \right) N_1 + \left(e \frac{\partial v}{\partial \eta} + \frac{1}{\rho} \eta_* \frac{\partial p}{\partial \eta} \right) N_2 + \left(e \frac{\partial w}{\partial \eta} + \frac{1}{\rho r} \eta_* \frac{\partial p}{\partial \eta} \right) N_3 \right] - a^2 \rho \left(\eta_* \frac{\partial u}{\partial \eta} + \eta_* \frac{\partial v}{\partial \eta} + \frac{1}{r} \eta_* \frac{\partial w}{\partial \eta} \right) - e \frac{\partial p}{\partial \eta} = -F \quad (4)$$

where

$$F = -\rho a (N_1 G_1 + N_2 G_2 + N_3 G_3) + a^2 G_1 + G_3$$

$$\begin{bmatrix} N_1 \\ N_2 \\ N_3 \end{bmatrix} = \left(\frac{a}{V^2} - \frac{V_*}{V^2} \sqrt{\frac{V^2 - a^2}{V^2 - V_*^2}} \right) \begin{bmatrix} u \\ v \\ w \end{bmatrix} - \sqrt{\frac{V^2 - a^2}{V^2 - V_*^2}} \begin{bmatrix} n_{s1} \\ n_{s2} \\ n_{s3} \end{bmatrix}$$

$$V = \sqrt{u^2 + v^2 + w^2}$$

$$V_* = un_{s1} + vn_{s2} + wn_{s3}$$

$$\begin{bmatrix} n_{s1} \\ n_{s2} \\ n_{s3} \end{bmatrix} = \frac{1}{\sqrt{1 + m_1^2 + m_2^2}} \begin{bmatrix} -m_1 \\ 1 \\ -m_2 \end{bmatrix}$$

where n_{s1} , n_{s2} , and n_{s3} are the unit normal vector of the shock wave plane,

$$m_1 = \frac{\partial f_1}{\partial z}, \quad m_2 = \frac{1}{f_1} \frac{\partial f_1}{\partial \phi}$$

In addition, the shock wave point solution should also satisfy the Ranke-Hugoniot relation:

$$\begin{aligned}
 p &= \frac{S}{\gamma+1} + \sqrt{\frac{S^2}{(\gamma+1)^2} - \left(\frac{\gamma-1}{\gamma+1}\right)(L-S^2)} \\
 \rho &= \frac{1}{s-p} \cdot \rho_1 V_{s1}^2 \\
 u &= u_1 - \left(1 - \frac{\rho_1}{\rho}\right) n_{11} V_{s1} \\
 v &= v_1 - \left(1 - \frac{\rho_1}{\rho}\right) n_{12} V_{s1} \\
 w &= w_1 - \left(1 - \frac{\rho_1}{\rho}\right) n_{13} V_{s1}
 \end{aligned} \tag{5}$$

where

$$\begin{aligned}
 S &= p_1 + \rho_1 V_{s1}^2 \\
 L &= \frac{2\gamma}{\gamma-1} p_1 \rho_1 V_{s1}^2 + \rho_1^2 V_{s1}^4
 \end{aligned}$$

p_1 , ρ_1 , u_1 , v_1 , and w_1 are quantities in front of the wave.

In order to facilitate obtaining the numerical solution, the Ranke-Hugoniot was differentiated with respect to η . It was then used simultaneously with the characteristic compatibility relation to derive the differential equation for the shock wave slope m_1

$$\frac{\partial m_1}{\partial \eta} = \frac{-F - L_{s1}}{L_{s1}} \tag{6}$$

where

$$\begin{aligned}
 L_{s1} &= \rho a \left[\left(eK_s + \frac{1}{\rho} \eta_s K_s \right) N_1 + \left(eK_s + \frac{1}{\rho} \eta_r K_s \right) N_2 + \left(eK_s + \frac{1}{\rho r} \eta_s K_s \right) N_3 - \right. \\
 &\quad \left. - a^2 \rho \left(\eta_s K_s + \eta_r K_s + \frac{1}{r} \eta_s K_s \right) - eK_s \right] \\
 L_{s1} &= \rho a \left[\left(eI_s + \frac{1}{\rho} \eta_s I_s \right) N_1 + \left(eI_s + \frac{1}{\rho} \eta_r I_s \right) N_2 + \left(eK_s + \frac{1}{\rho r} \eta_s I_s \right) N_3 - \right. \\
 &\quad \left. - a^2 \rho \left(\eta_s I_s + \eta_r I_s + \frac{1}{r} \eta_s I_s \right) - eI_s \right]
 \end{aligned}$$

$$\begin{bmatrix} K_1 \\ K_2 \\ K_3 \\ K_4 \end{bmatrix} = \frac{\partial}{\partial m_1} \begin{bmatrix} p \\ u \\ v \\ w \end{bmatrix} + a_2 \frac{\partial}{\partial m_2} \begin{bmatrix} p \\ u \\ v \\ w \end{bmatrix}, \quad \begin{bmatrix} I_1 \\ I_2 \\ I_3 \\ I_4 \end{bmatrix} = \beta_1 \frac{\partial}{\partial m_2} \begin{bmatrix} p \\ u \\ v \\ w \end{bmatrix}$$

$$a_2 = \frac{1}{f_1} z_1 \eta_1$$

$$\beta_1 = \frac{1}{f_1} z_1 \frac{\partial m_1}{\partial \psi} - \frac{1}{f_1^2} f_{11} \cdot f_{12}$$

$$z_1 = E_1 + E_2 f_{11}$$

All the derivatives of flow parameters with respect to m_1 and m_2 can be obtained from the Rankine-Hugoniot relation.

Equations (5) and (6) are the equations to solve the shock wave point.

3. Surface Boundary Conditions and Characteristic Compatibility Relations

From an analysis of the surface boundary characteristics we know that there are four compatibility relations in calculating a surface point: three flow characteristic compatibility relations and the Porter II series compatibility relation. They are

$$\begin{aligned}
& e \left(u \frac{\partial u}{\partial \eta} + v \frac{\partial v}{\partial \eta} + w \frac{\partial w}{\partial \eta} \right) + \frac{1}{\rho} \left(u \eta_z + v \eta_r + \frac{w}{r} \eta_\theta \right) \frac{\partial p}{\partial \eta} = E_1, \\
& e \left(t_1 \frac{\partial u}{\partial \eta} + t_2 \frac{\partial v}{\partial \eta} + t_3 \frac{\partial w}{\partial \eta} \right) + \frac{1}{\rho} \left(t_1 \eta_z + t_2 \eta_r + \frac{t_3}{r} \eta_\theta \right) \frac{\partial p}{\partial \eta} = E_2, \\
& e \frac{\partial p}{\partial \eta} - a^2 e \frac{\partial \rho}{\partial \eta} = E_3, \\
& -\rho a \left[\left(e \frac{\partial u}{\partial \eta} + \frac{1}{\rho} \eta_z \frac{\partial p}{\partial \eta} \right) N_1 + \left(e \frac{\partial v}{\partial \eta} + \frac{1}{\rho} \eta_r \frac{\partial p}{\partial \eta} \right) N_2 + \left(e \frac{\partial w}{\partial \eta} + \right. \right. \\
& \left. \left. + \frac{1}{\rho r} \eta_\theta \frac{\partial p}{\partial \eta} \right) N_3 + a^2 \rho \left(\eta_z \frac{\partial u}{\partial \eta} + \eta_r \frac{\partial v}{\partial \eta} + \frac{1}{r} \eta_\theta \frac{\partial w}{\partial \eta} \right) + e \frac{\partial p}{\partial \eta} \right] = E_4.
\end{aligned} \tag{7}$$

where

$$\begin{aligned}
E_1 &= G_1 u + G_2 v + G_3 w, \quad E_2 = G_1 t_1 + G_2 t_2 + G_3 t_3, \\
E_3 &= G_4, \quad E_4 = -\rho a (N_1 G_1 + N_2 G_2 + N_3 G_3) + a^2 G_1 + G_4, \\
\begin{bmatrix} t_1 \\ t_2 \\ t_3 \end{bmatrix} &= \frac{1}{V} \begin{bmatrix} v n_1 - w n_2 \\ w n_1 - u n_3 \\ u n_2 - v n_1 \end{bmatrix}
\end{aligned}$$

/34

$$\begin{bmatrix} N_1 \\ N_2 \\ N_3 \end{bmatrix} = \frac{1}{VM} \begin{bmatrix} u \\ v \\ w \end{bmatrix} + \sqrt{1 + \frac{1}{M^2}} \begin{bmatrix} n_1 \\ n_2 \\ n_3 \end{bmatrix}, \quad \left(M = \frac{V}{a} \right)$$

n_1 , n_2 , and n_3 are the unit normal vectors of the surface.

In addition, a surface point should also satisfy the following boundary condition:

$$n_1 \frac{\partial u}{\partial \eta} + n_2 \frac{\partial v}{\partial \eta} + n_3 \frac{\partial w}{\partial \eta} = G \tag{8}$$

where

$$G = -\left(u \frac{\partial n_1}{\partial \eta} + v \frac{\partial n_2}{\partial \eta} + w \frac{\partial n_3}{\partial \eta}\right)$$

The differential equation for a surface point can be derived from equations (7) and (8):

$$\frac{\partial \rho}{\partial \eta} = \frac{-(J_1 + J_2)e + a^2 \rho \left(\eta_1 J_1 + \eta_2 J_2 + \frac{1}{r} \eta_3 J_3 \right)}{e \left(e - a \bar{n} \sqrt{1 - \frac{1}{M^2}} \right) - a^2 \left(\eta_1 W_1 + \eta_2 W_2 + \frac{1}{r} \eta_3 W_3 \right)}$$

$$\frac{\partial \rho}{\partial \eta} = \frac{J_1 + e \frac{\partial \rho}{\partial \eta}}{a^2 e} \quad (9)$$

$$\frac{\partial u}{\partial \eta} = \frac{1}{e} \left(-J_1 - \frac{1}{\rho} W_1, \frac{\partial \rho}{\partial \eta} \right)$$

$$\frac{\partial v}{\partial \eta} = \frac{1}{e} \left(-J_2 - \frac{1}{\rho} W_2, \frac{\partial \rho}{\partial \eta} \right)$$

$$\frac{\partial w}{\partial \eta} = \frac{1}{e} \left(-J_3 - \frac{1}{\rho} W_3, \frac{\partial \rho}{\partial \eta} \right)$$

where

$$J_1 = H_1 \frac{u}{V} + H_2 t_1 + H_3 n_1$$

$$J_2 = H_1 \frac{v}{V} + H_2 t_2 + H_3 n_2$$

$$J_3 = H_1 \frac{w}{V} + H_2 t_3 + H_3 n_3$$

$$J_4 = \rho a \sqrt{1 - \frac{1}{M^2}} (H_1 + n_1 G_1 + n_2 G_2 + n_3 G_3) - a^2 G_1, \quad J_5 = -G_1$$

$$H_1 = -\frac{1}{V} (G_1 u + G_2 v + G_3 w)$$

$$H_2 = -(G_1 t_1 + G_2 t_2 + G_3 t_3), \quad H_3 = -G_2$$

$$W_1 = \frac{eu}{V_1} + \bar{t} t_1, \quad W_2 = \frac{ev}{V_2} + \bar{t} t_2, \quad W_3 = \frac{ew}{V_3} + \bar{t} t_3,$$

$$\bar{t} = t_1 \eta_1 + t_2 \eta_2 + t_3 \left(\frac{1}{r} \eta_3 \right)$$

III. Numerical Computation

The computation of a supersonic inviscid flow is mathematically a problem to solve the initial boundary value of a five variable quasi-linear hyperbolic equation series. After the solution on the given initial plane is obtained, the computation can advance. Specifically for a bent cone, this method involves: (1) using equation (3) and its corresponding boundary equations (6) and (9) to find a discrete solution in the "inclined advance" solving region by transforming the initial plane η_0 to another plane (which is perpendicular to the body axis of the rear cone). Of course, the initial plane and the solving plane must be spatially directed. (2) The flow parameters and shock wave shape parameters are converted from the (z_1, r_1, ϕ_1) coordinate and the (z_2, r_2, ϕ_2) coordinate (see Figure 1). (3) The transformed plane is used as the initial plane to find the solution at the object end by "parallel advance". The specific method is shown in reference [2]. (4) In the "advance" calculation, we will encounter some points on the ridge of the surface. The flow may expand or contract at these points. Therefore, it is necessary to solve these singular points individually.

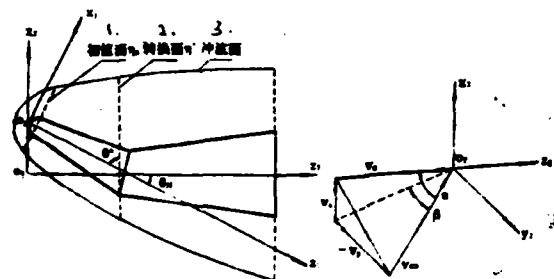


Figure 1. Definition of Attack Angle and Sideslip Angle

1. initial value plane n_e ,
2. transformation plane n'
3. shock wave plane

1. Calculation of Points in the Flow Field

\bar{f} is used to express a column vector whose components are p , ρ , u , v , and w . For equation (3), the pre-estimation step and the modification step of the MacCormack scheme can be written as

$$\bar{f}_{i,j}^{*} = \bar{f}_{i,j} + \left(\frac{\partial \bar{f}}{\partial \eta} \right)_{i,j}^{*} \Delta \eta \quad (10)$$

$$\bar{f}_{i,j}^{**} = \frac{1}{2} \left[\bar{f}_{i,j} + \bar{f}_{i,j}^{*} + \left(\frac{\partial \bar{f}}{\partial \eta} \right)_{i,j}^{*} \Delta \eta \right] \quad (11)$$

The values of $\partial \bar{f} / \partial \xi$ and $\partial \bar{f} / \partial \varphi$, which are derivatives of flow parameters with respect to ξ and φ included in the function of $\partial \bar{f} / \partial \eta$, were approached by the forward (pre-estimate) and backward (modification) derivation difference. When the radial mesh spacing $\Delta \xi$ and circumferential mesh spacing $\Delta \varphi$ are ascertained, the integration step $\Delta \eta$ is determined by the stability condition.

2. Calculation of Shock Wave Points

The differential equation (6) was solved by discretization using the MacCormack scheme. The pre-estimate and modification

steps are:

$$(m_1)_{i,j}^{*+1} = (m_1)_{i,j}^* + \left(\frac{\partial m_1}{\partial \eta} \right)_{i,j}^* \cdot \Delta \eta \quad (12)$$

$$(m_1)_{i,j}^{*+1} = \frac{1}{2} \left[(m_1)_{i,j}^* + (m_1)_{i,j}^{*+1} + \left(\frac{\partial m_1}{\partial \eta} \right)_{i,j}^{*+1} \cdot \Delta \eta \right] \quad (13)$$

The pre-estimate and modification steps for the shock wave position f_1 are: /36

$$(f_1)_{i,j}^{*+1} = (f_1)_{i,j}^* + (m_1)_{i,j}^* \cdot \Delta \eta \quad (14)$$

$$(f_1)_{i,j}^{*+1} = \frac{1}{2} \left\{ (f_1)_{i,j}^* + (f_1)_{i,j}^{*+1} + \frac{1}{2} \left[(m_1)_{i,j}^* + (m_1)_{i,j}^{*+1} \right] \cdot \Delta \eta \right\} \quad (15)$$

The values of $\partial m_1 / \partial \varphi$ in the right function of $\partial m_1 / \partial \eta$ can be approached by the central difference of the m_1 values at various φ . The values of $\partial \bar{f} / \partial \xi$ for various derivatives of flow parameters with respect to φ are approached by the same method as that for internal points. The values of $\partial \bar{f} / \partial \xi$ are approached by a two point backward difference method in the pre-estimation step. In the modification step, they are approached by a three point derivation difference method.

The simple process of shock wave point computer is described as follows. The shock wave slope m_1 was determined by the difference scheme (12) or (13). The shock wave position f_1 was obtained from the difference scheme (14) or (15). $f'_{1\phi}$ was determined by the central difference of the f_1 value on each meridian plane. Then, the circumferential slope of the shock wave $f'_{1\phi}$ and m_2 can be obtained from the following equation:

$$f'_{1\phi} = \frac{-f'_{1\phi} E_\phi + f'_{1\phi} E_\phi}{E_\phi + f'_{1\phi} E_\phi} \quad (16)$$

In the above equation

$$f'_{1\phi} = \frac{m_1 E_\phi}{1 - m_1 E_\phi}$$

Finally, flow parameters behind the wave were determined by m_1 and m_2 using the Rankine-Hugoniot relation.

3. Computation of Surface Points

The same difference scheme as that for internal points is used to discretize and solve the surface point equation (9). In the modification step, the radial differential $\partial \bar{f} / \partial \xi$ included in the right function is approached by a three point deviation difference method.

4. Tightening of Mesh Points Near the Surface

A boundary surface $\xi_i = \text{const}$ was set up to divide the meshes near the surface. Smaller meshes are used inside and larger meshes are used on the outside. If the total number of radial meshes is N and the boundary is set up at $i = n'$, then the mesh spring inside (close to the surface of the object) is

$$\Delta \xi_n = \frac{1}{(N - n' + 1) n'}$$

Outside the boundary, it is

$$\Delta \xi_n = \frac{1}{N - n' + 1}$$

Therefore, the meshes near the surface are significantly tightened as compared to uniform meshes while the total number of meshes does not increase.

IV. Calculation of Flow Characteristics at Singularity Points on the Surface

Because the flow parameters on the intersecting line of the front and rear cones have multiple values, therefore, they must be solved individually. The specific method is to establish a right angle coordinate $(\bar{t}_1, \bar{t}_2, \bar{t}_3)$ at the origin A on the intersect. \bar{t}_2 is the direction of the unit normal vector of the front cone surface, \bar{t}_3 is in the direction of the tangent of the

inner intersecting line and \bar{t}_1 is perpendicular to both \bar{t}_2 and \bar{t}_3 .

$$\bar{t}'_1 = \frac{\bar{t}_2 \times \bar{t}_3}{|\bar{t}_2 \times \bar{t}_3|} \quad (D)$$

The supersonic flow expands or contracts on the \bar{t}_1 - \bar{t}_2 plane /37 so that the flow direction is shifted by a certain angle. The flow parameters satisfy the two-dimensional Prandtl-Meyer solution or two-dimensional shock wave correlation. Moreover, the velocity component along \bar{t}_3 does not change beyond point A.

V. Numerical Examples

Several numerical examples are given in the following.

Figure 2 shows the pressure distribution around a bent cone obtained by the "parallel advance" and "inclined advance" method. The "inclined advance" method began with the initial value plane ($\theta_0 = 90^\circ$) to $\theta_1^* = 74^\circ$, then from $\theta_1^* = 74^\circ$ to $\theta_2^* = 90^\circ$. From the figure we can see that the results of these two techniques are identical. The same accuracy resulted.

Figures 3 and 4 show the pressure distribution on the surface of the object around bent cone A. The geometric parameters are $\theta_1 = 10^\circ$, $\theta_2 = 7^\circ$, $\eta^* = 8$ and $\theta_N = 6^\circ$. Furthermore, there is a transition link between the front and rear cones. Therefore, there are two intersecting lines on the surface. When the angle of attack is large, the inviscid flow equation cannot appropriately describe the true flow pattern. Furthermore, the attack angle of the front cone $a_{\text{front}} = a + \theta_N$ in the computation. Therefore, the attack angle range is greatly related to the degree of bending of the bent cone. In this example, the largest angle of attack was 14° and the results are still good.

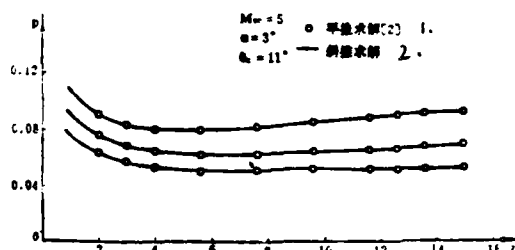


Figure 2. Comparison of Pressure Distributions on Bent Cone by "Parallel Advance" and "Inclined Advance" Methods

1. parallel advance solution [2]
2. inclined advance solution

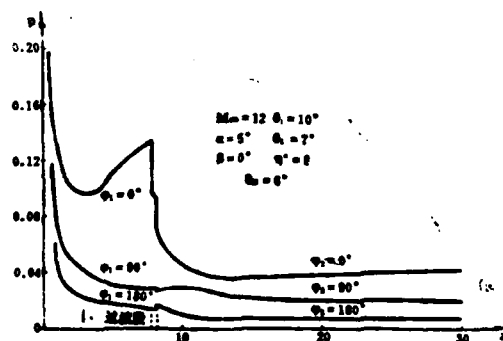


Figure 3. Surface Pressure Distribution of Bent Cone A

1. transition section

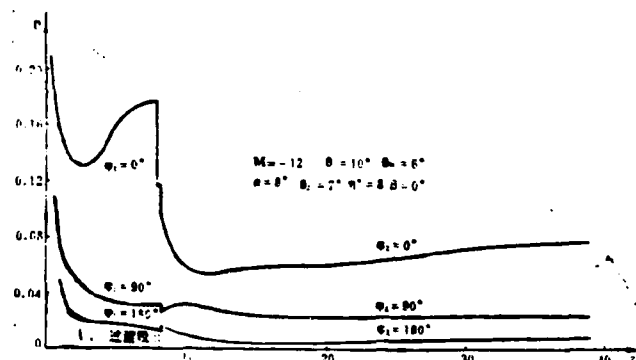


Figure 4. Surface Pressure Distribution of Bent Cone A

1. transition section

Figures 5, 6, and 7 are the flow field pressure characteristics and internal shock wave shape of bent cone B ($\theta_1 = \theta_2 = 7^\circ$, $\theta_N = 13^\circ$) with sideslip. The mesh numbers used in the calculation were $M = 20$ (radial) and $M = 20$ (circumferential). No filtering was used to smooth the process. The inner shock wave position in the figure is determined by the pressure variation in the flow field. From Figure 7 we can see that the pressure change position (i.e., a strong interruption position) is very obvious when an inner shock wave appears. Therefore, it is basically correct to determine the inner shock wave position based on it. In addition, the result of total entropy was compared with. From the numerical examples, the calculated entropy of flow field points and boundary points is in agreement with that of the incoming flow.

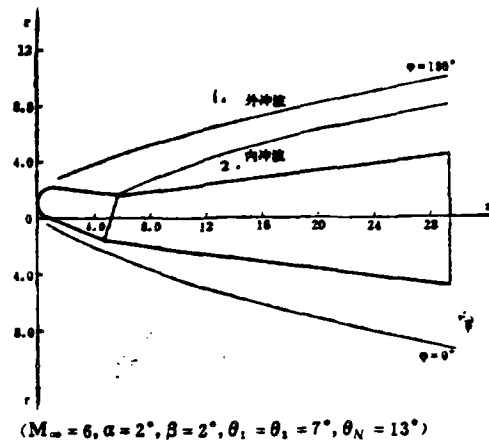


Figure 5. Shape of Shock Wave of Bent Cone B (expansion wave not shown)

1. external shock wave
2. inner shock wave

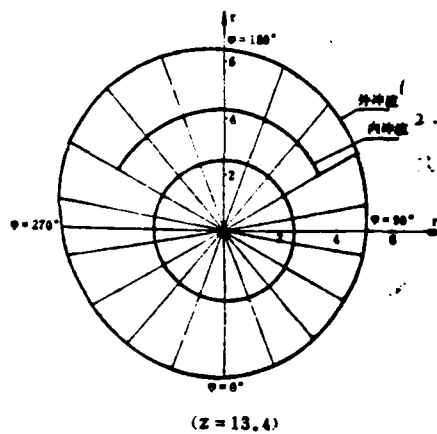


Figure 6. Shape of Shock Wave of Bent Cone B

1. external shock wave
2. inner shock wave

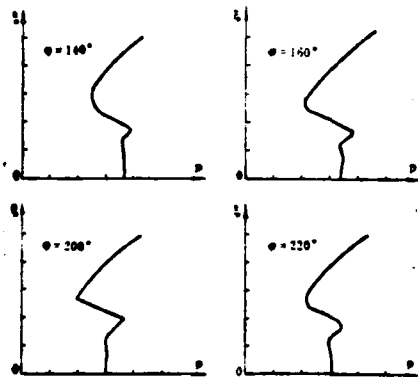


Figure 7. Pressure Characteristics at Z = 14.4 for Bent Cone B

References

- [1] Zhu Youlan, Zhong Xichang, Chen Bingmu and Zhang Zuomin, A Difference Method for Initial Boundary Value Problems and Flow Around a Body, Science Publishing Co., 1980.
- [2] Ji Chuqun, A Numerical Method for Supersonic Inviscid Flow with Inner Shock Wave, Journal of Aeronautics, 2 (1980).
- [3] Kutler, P., Warming, R., Lomax, H., AIAA J., Vol. 11, No. 2 (1973).

A NUMERICAL COMPUTATION FOR THE INVISCID SUPERSONIC FLOW AROUND BENT CONE

Ji Chuqun

(Beijing Institute of Aerodynamics)

Abstract

A numerical computation method for the inviscid supersonic flow around a bent cone is given in this paper by using finite-difference method and shock-capturing technique. In order to overcome the difficulty due to the bend of the bent cone axis in the advanced process solving equation, the solving plane of Euler equation is considered as a inclined plane with the advanced direction using a transform of the equation independent variables. The second order, two-step MacCormack scheme is used. The equation system for boundary computation is derived according to the characteristic compatibility relations on body surface or shock wave and corresponding boundary condition. The flow properties of the singular points on the intersected line between two cone surface are solved individually. The non-uniform computation meshes along the direction of body radius are used in order to raise the computation accuracy when the gradient of the entropy near body surface is very large. The computation results in many numerical examples indicate that good results can be obtained by means of this method.

Theory of Similarity and the Profile of the Mean Density
Distribution of Hypersonic Boundary Layer

Cai Shutang (Department of Modern Mechanics, The
University of Science and Technology of China)

Gao Shouen (Department of Physics, Hangzhou Teachers College)

Abstract

It is well known that in a boundary layer, the variation of [1] the physical quantity along the flow direction (the x direction) is much smaller than that along the direction perpendicular to the flow (the y direction). At the same time, the velocity in the "y" direction is much smaller than that in the "x" direction. In this paper, we derive the vorticity pulsating equations by means of neglecting the physical quantity variation in the "x" direction and the velocity variation in the "y" direction. In a coordinate system of the average fluid velocity motion, we introduce the similarity hypothesis to determine the pulsating velocity and the pulsating density. Based on the necessary condition of the pulsating similarity, we find the equation $\bar{p} = k(y + y_0)^n$ as the average density variation rule in the turbulent boundary layer of the compressible fluid. Although this method is very approximate, it conforms to the experimental data. This paper demonstrates that in a comparatively large range, the similarity hypothesis is applicable.

I. Introduction

Many papers have been published about the turbulent boundary layer of the incompressible fluid on a flat surface. Although some other papers discussed the turbulent boundary layer of the compressible fluid on a flat surface, yet their discussions were incomplete, and their selections of the close systems were quite arbitrary. In this paper we adopt the vorticity similarity conception to study the profile of the mean density distribution

received on May 16, 1983, revised Sept. 20, 1983

of the hypersonic boundary layer. We directly applied Prof. Zhou Peiyuan's method (published in 1959) of the compressible fluid vorticity equations. Based on the premise of the similarity conditions, we obtain a few groups of the related physical quantity equations. They can be simplified to satisfy the differential equations for the mean density. After integrating we obtain an exponent equation for the mean density profile. This process seems to be too approximate. However, the mathematical results conform with the experiment results in a wide range.

II. Vorticity Pulsating Equations of Compressible Fluid

First, let us put down the Navier-Stokes equations for compressible fluid and the Reynolds equation after the Navier-Stokes equations being averaged by the Reynolds method, i.e.

$$\frac{\partial}{\partial t}(\rho U_i) + \frac{\partial}{\partial x_j}(\rho U_i U_j) = -\frac{\partial p}{\partial x_i} + \frac{\partial}{\partial x_j} \sigma_{ij} \quad (1)$$

$$\frac{\partial}{\partial t}(\bar{\rho} \bar{U}_i + \overline{\rho' u'_i}) + \frac{\partial}{\partial x_j}(\bar{\rho} \bar{U}_i \bar{U}_j + \bar{\rho} \overline{u'_i u'_j} + \overline{\rho' u'_i} \bar{U}_j + \bar{\rho}' \bar{U}_i \bar{U}_j + \overline{\rho' u'_i u'_j})$$

$$= -\frac{\partial \bar{p}}{\partial x_i} + \frac{\partial}{\partial x_j} \bar{\sigma}_{ij} \quad (2) \quad /50$$

where, U_i = velocity, p' = pressure, ρ = density, σ_{ij} = stress tensors other than pressure. As to the relation of the mean quantity and instantaneous quantity, we have

$$A = \bar{A} + A', \quad \bar{A}' = 0$$

where, A' = physical quantity and A = pulsating quantity. When we subtract (1) from (2), we obtain

$$\begin{aligned} & \frac{\partial}{\partial t}(\bar{\rho} u'_i + \bar{U}_i \rho' + \rho' u'_i - \overline{\rho' u'_i}) + \frac{\partial}{\partial x_j}(\bar{\rho} \bar{U}_i u'_j + \bar{\rho} \bar{U}_i u'_j + \rho' \bar{U}_i \bar{U}_j \\ & + \bar{\rho} u'_i u'_j - \bar{\rho} \overline{u'_i u'_j} + \bar{U}_i \rho' u'_j - \bar{U}_i \overline{\rho' u'_j} + \bar{U}_i \rho' u'_i - \bar{U}_i \overline{\rho' u'_i} \\ & + \rho' u'_i u'_j - \overline{\rho' u'_i u'_j}) = -\frac{\partial p'}{\partial x_i} + \frac{\partial}{\partial x_j} \sigma'_{ij} \end{aligned} \quad (3)$$

Similarly, we have a continuous equation and an averaged continuous equation:

$$\frac{\partial}{\partial t} \rho + \frac{\partial}{\partial x_i} (\rho U_i) = 0 \quad (4)$$

$$\frac{\partial}{\partial t} \bar{\rho} + \frac{\partial}{\partial x_i} (\bar{\rho} \bar{U}_i + \overline{\rho' u'_i}) = 0 \quad (5)$$

The subtraction between these two equations results in the pulsating density equation:

$$\frac{\partial \rho'}{\partial t} + \frac{\partial}{\partial x_i} (\rho' \bar{U}_i + \bar{\rho} u'_i + \rho' u'_i - \overline{\rho' u'_i}) = 0 \quad (6)$$

In equation (3), when we retain the spin factor, cancel "p'", simplify it with equations (5) and (6), and let

$$\omega_{ik} = \frac{\partial u'_i}{\partial x_k} - \frac{\partial u'_k}{\partial x_i}, \quad \Omega_{ik} = \frac{\partial \bar{U}_i}{\partial x_k} - \frac{\partial \bar{U}_k}{\partial x_i}$$

then we can obtain the equation to satisfy the pulsating vorticity ω_{ik}

$$\begin{aligned} & \bar{\rho} \frac{\partial}{\partial t} \omega_{ik} + \rho' \frac{\partial}{\partial t} \Omega_{ik} - \omega_{ik} \frac{\partial}{\partial x_i} \overline{\rho' u'_i} + \bar{\rho} \bar{U}_i \frac{\partial}{\partial x_i} \omega_{ik} + \bar{\rho} u'_i \frac{\partial}{\partial x_i} \Omega_{ik} + \\ & + \rho' \bar{U}_i \frac{\partial}{\partial x_i} \Omega_{ik} + \rho' u'_i \frac{\partial}{\partial x_i} \Omega_{ik} + \xi_{ik} + T_{ik} \\ & = \frac{\partial^2 \sigma'_{ij}}{\partial x_i \partial x_j} - \frac{\partial^2 \sigma'_{ki}}{\partial x_i \partial x_k} \end{aligned} \quad (7)$$

in which,

$$\begin{aligned} \xi_{ik} = & \frac{\partial u'_i}{\partial t} \frac{\partial \bar{\rho}}{\partial x_k} - \frac{\partial u'_k}{\partial t} \frac{\partial \bar{\rho}}{\partial x_i} + \left(u'_i \frac{\partial^2 \bar{\rho}}{\partial t \partial x_k} - u'_k \frac{\partial^2 \bar{\rho}}{\partial t \partial x_i} \right) + \frac{\partial \bar{U}_i}{\partial t} \frac{\partial \rho'}{\partial x_k} \\ & - \frac{\partial \bar{U}_k}{\partial t} \frac{\partial \rho'}{\partial x_i} + \bar{U}_i \frac{\partial^2 \rho'}{\partial t \partial x_k} - \bar{U}_k \frac{\partial^2 \rho'}{\partial t \partial x_i} + \frac{\partial^2}{\partial t \partial x_k} (\rho' u'_i) \\ & - \frac{\partial^2}{\partial t \partial x_i} (\rho' u'_k) + \frac{\partial^2 \rho'}{\partial x_i \partial x_k} \bar{U}_i \bar{U}_k - \frac{\partial^2 \rho'}{\partial x_k \partial x_i} \bar{U}_k \bar{U}_i \end{aligned}$$

$$\begin{aligned}
& + \frac{\partial \rho'}{\partial x_i} \frac{\partial}{\partial x_i} (\bar{U}_i \bar{U}_i) - \frac{\partial \rho'}{\partial x_i} \frac{\partial}{\partial x_i} (\bar{U}_i \bar{U}_i) + \frac{\partial \rho'}{\partial x_i} \left(\bar{U}_i \frac{\partial \bar{U}_i}{\partial x_i} - \right. \\
& \left. - \bar{U}_i \frac{\partial \bar{U}_i}{\partial x_i} \right) + \rho' \frac{\partial}{\partial x_i} \left(\bar{U}_i \frac{\partial \bar{U}_i}{\partial x_i} - \bar{U}_i \frac{\partial \bar{U}_i}{\partial x_i} \right) + \frac{\partial u'_i}{\partial x_i} \bar{U}_i \frac{\partial \bar{\rho}}{\partial x_i} \\
& - \frac{\partial u'_i}{\partial x_i} \bar{U}_i \frac{\partial \bar{\rho}}{\partial x_i} + u'_i \frac{\partial}{\partial x_i} \left(\bar{U}_i \frac{\partial \bar{\rho}}{\partial x_i} \right) - u'_i \frac{\partial}{\partial x_i} \left(\bar{U}_i \frac{\partial \bar{\rho}}{\partial x_i} \right) + \frac{\partial u'_i}{\partial x_i} \bar{\rho} \frac{\partial \bar{U}_i}{\partial x_i} \\
& - \frac{\partial u'_i}{\partial x_i} \bar{\rho} \frac{\partial \bar{U}_i}{\partial x_i} + u'_i \frac{\partial}{\partial x_i} \left(\bar{\rho} \frac{\partial \bar{U}_i}{\partial x_i} \right) - u'_i \frac{\partial}{\partial x_i} \left(\bar{\rho} \frac{\partial \bar{U}_i}{\partial x_i} \right) \\
& + \frac{\partial u'_i}{\partial x_i} \left(\frac{\partial \bar{\rho}}{\partial x_i} \bar{U}_i - \frac{\partial \bar{\rho}}{\partial x_i} \bar{U}_i \right) + u'_i \frac{\partial}{\partial x_i} \left(\frac{\partial \bar{\rho}}{\partial x_i} \bar{U}_i - \frac{\partial \bar{\rho}}{\partial x_i} \bar{U}_i \right) \\
& + \frac{\partial^2 u'_i}{\partial x_i \partial x_i} \bar{\rho} \bar{U}_i - \frac{\partial^2 u'_i}{\partial x_i \partial x_i} \bar{\rho} \bar{U}_i + \frac{\partial}{\partial x_i} (\bar{\rho} \bar{U}_i) \frac{\partial u'_i}{\partial x_i} - \frac{\partial}{\partial x_i} (\bar{\rho} \bar{U}_i) \frac{\partial u'_i}{\partial x_i} \\
& + \frac{\partial \bar{U}_i}{\partial x_i} \left(\frac{\partial \rho'}{\partial x_i} u'_i - \frac{\partial \rho'}{\partial x_i} u'_i \right) + \bar{U}_i \frac{\partial}{\partial x_i} \left(\frac{\partial \rho'}{\partial x_i} u'_i - \frac{\partial \rho'}{\partial x_i} u'_i \right) \\
& + \frac{\partial}{\partial x_i} (\rho' \omega_{ii}) \bar{U}_i + \frac{\partial \bar{U}_i}{\partial x_i} \rho' \omega_{ii} + \frac{\partial}{\partial x_i} (\rho' u'_i) \frac{\partial \bar{U}_i}{\partial x_i} - \frac{\partial}{\partial x_i} (\rho' u'_i) \frac{\partial \bar{U}_i}{\partial x_i} \\
& + \rho' u'_i \frac{\partial^2 \bar{U}_i}{\partial x_i \partial x_i} - \rho' u'_i \frac{\partial^2 \bar{U}_i}{\partial x_i \partial x_i} + \frac{\partial}{\partial x_i} \left(u'_i \frac{\partial \rho'}{\partial x_i} \right) \bar{U}_i \\
& - \frac{\partial}{\partial x_i} \left(u'_i \frac{\partial \rho'}{\partial x_i} \right) \bar{U}_i + u'_i \frac{\partial \rho'}{\partial x_i} \frac{\partial \bar{U}_i}{\partial x_i} - u'_i \frac{\partial \rho'}{\partial x_i} \frac{\partial \bar{U}_i}{\partial x_i} \\
& + \bar{U}_i \frac{\partial}{\partial x_i} \left(\rho' \frac{\partial u'_i}{\partial x_i} \right) - \bar{U}_i \frac{\partial}{\partial x_i} \left(\rho' \frac{\partial u'_i}{\partial x_i} \right) + \frac{\partial \bar{U}_i}{\partial x_i} \rho' \frac{\partial u'_i}{\partial x_i} \\
& - \frac{\partial \bar{U}_i}{\partial x_i} \rho' \frac{\partial u'_i}{\partial x_i} + \frac{\partial \bar{\rho}}{\partial x_i} \frac{\partial}{\partial x_i} (u'_i u'_i) - \frac{\partial \bar{\rho}}{\partial x_i} \frac{\partial}{\partial x_i} (u'_i u'_i) \\
& + \frac{\partial^2 \bar{\rho}}{\partial x_i \partial x_i} u'_i u'_i - \frac{\partial^2 \bar{\rho}}{\partial x_i \partial x_i} u'_i u'_i + \frac{\partial \bar{\rho}}{\partial x_i} \omega_{ii} u'_i \\
& + \bar{\rho} \frac{\partial}{\partial x_i} (\omega_{ii} u'_i) + \frac{\partial \bar{\rho}}{\partial x_i} \left(u'_i \frac{\partial u'_i}{\partial x_i} - u'_i \frac{\partial u'_i}{\partial x_i} \right) \\
& + \bar{\rho} \frac{\partial}{\partial x_i} \left(u'_i \frac{\partial u'_i}{\partial x_i} - u'_i \frac{\partial u'_i}{\partial x_i} \right) + \frac{\partial^2}{\partial x_i \partial x_i} (\rho' u'_i u'_i) \\
& - \frac{\partial^2}{\partial x_i \partial x_i} (\rho' u'_i u'_i) \\
T_{ii} = & \frac{\partial}{\partial t} \left[- \frac{\partial}{\partial x_i} (\overline{\rho' u'_i}) + \frac{\partial}{\partial x_i} (\overline{\rho' u'_i}) \right] - \overline{\rho' u'_i} \frac{\partial}{\partial x_i} \Omega_{ii} \\
& + \frac{\partial}{\partial x_i} \left[- \bar{U}_i \left(\frac{\partial}{\partial x_i} \overline{\rho' u'_i} - \frac{\partial}{\partial x_i} \overline{\rho' u'_i} \right) - \left(\overline{\rho' u'_i} \frac{\partial}{\partial x_i} \bar{U}_i \right. \right.
\end{aligned}$$

$$\begin{aligned}
& -\overline{\rho' u_i} \frac{\partial \bar{U}_i}{\partial x_i} - \left(\frac{\partial \overline{\rho' u_i}}{\partial x_i} \bar{U}_i - \frac{\partial}{\partial x_i} \overline{\rho' u_i} \bar{U}_i \right) \\
& - \left(\frac{\partial \bar{\rho}}{\partial x_i} \overline{u_i u_i} - \frac{\partial \bar{\rho}}{\partial x_i} \overline{u_i u_i} \right) - \bar{\rho} \left(\frac{\partial \overline{u_i u_i}}{\partial x_i} \right. \\
& \left. - \frac{\partial}{\partial x_i} \overline{u_i u_i} \right) - \left(\frac{\partial}{\partial x_i} \overline{\rho' u_i u_i} - \frac{\partial}{\partial x_i} \overline{\rho' u_i u_i} \right)
\end{aligned}$$

III. Similarity and Mean Density of the Supersonic Boundary Layer

First, let us consider the steady state conditions, in which the partial derivative of the average quantity of equation (7) with respect to time is zero. Secondly, when we consider the supersonic boundary layer, the "x" derivative term of an average quantity can be neglected as compared to its "y" derivative. At the same time we can omit the velocity terms in the "y" direction. Then by adopting Zhou's method, we introduce a coordination system of motions which varies with the point "P₀", and also introduce a similar condition

$$\begin{aligned}
u_i' &= q \phi_i \left(\frac{x_i - x_i^0}{\Lambda} \right), \quad \rho' = \bar{\rho} \phi \left(\frac{x_i - x_i^0}{\Lambda} \right) \\
\xi_i &= \frac{x_i - x_i^0}{\Lambda}
\end{aligned}$$

Let,

then

$$\frac{u_i'}{q} = \phi_i(\xi_i), \quad \frac{\rho'}{\bar{\rho}} = \phi(\xi_i) \quad (8)$$

in which "x_i⁰", which can usually be considered as the origin, is the coordinate of point "P₀" in the coordinate system of motion. "x" is the coordinate of a certain point in this system, and "Λ" is the characteristic length of the pulsating quantity. We further substitute (8) to the vorticity pulsating equation (7),

and eliminate the viscosity terms in (7). In this paper, we are not going to write the details of the derivation because of the complexities of these equations. Here we only present the coefficients in front of the nondimensional $F(\xi_1)$ of all the terms in these equations. There are seven different coefficients as follows:

$$\begin{aligned} \textcircled{1} \quad & \frac{q}{\Lambda} \frac{d}{dy} \overline{\rho'V}, & \textcircled{2} \quad & \bar{\rho} q \frac{d^2 U}{dy^2}, \\ \textcircled{3} \quad & \bar{\rho} \frac{q}{\Lambda} \frac{dU}{dy}, & \textcircled{4} \quad & q \frac{d\bar{\rho}}{dy} \frac{dU}{dy}, \\ \textcircled{5} \quad & \frac{q^2}{\Lambda} \frac{d\bar{\rho}}{dy}, & \textcircled{6} \quad & q^2 \frac{d^2 \bar{\rho}}{dy^2}, \\ \textcircled{7} \quad & \bar{\rho} \frac{q^2}{\Lambda}. \end{aligned}$$

In order to obtain the similarity of the pulsating velocity " u_1 " and the pulsating density " p " in the profile of the boundary layer (i.e., in the profile of the boundary layer, the functions of $\phi_h(\xi_1)$ and $\phi(\xi_1)$ are identical), the ratios of these seven constants have to be independent of the " y " coordinate. Therefore, coefficient (3) is directly proportional to coefficient (4), i.e.,

$$\bar{\rho} \frac{q}{\Lambda} \frac{dU}{dy} \propto q \frac{d\bar{\rho}}{dy} \frac{dU}{dy}$$

After eliminating, $(dU/dy) q$ we obtain

$$\frac{d\bar{\rho}}{dy} \propto \frac{\bar{\rho}}{\Lambda} \quad /53 \quad (9)$$

Similarly coefficient (5) is directly proportional to (6), then

$$\frac{q^2}{\Lambda} \frac{d\bar{\rho}}{dy} \propto q^2 \frac{d^2 \bar{\rho}}{dy^2}$$

When we eliminate " q^2 ", we obtain

$$\Lambda \propto \frac{\frac{d\bar{\rho}}{dy}}{\frac{d^2 \bar{\rho}}{dy^2}} \quad (10)$$

When we eliminate " Λ " in (9) and (10), we obtain

$$C \frac{d\bar{\rho}}{dy} = \frac{\bar{\rho} \frac{d^2 \bar{\rho}}{dy^2}}{\frac{d\bar{\rho}}{dy}} \quad (11)$$

in which "C" is a constant. Simplifying, we obtain

$$\frac{\frac{d^2 \bar{\rho}}{dy^2}}{\frac{d\bar{\rho}}{dy}} = C \frac{\frac{d\bar{\rho}}{dy}}{\bar{\rho}} \quad (11)'$$

After integrating, we obtain

$$\ln \frac{d\bar{\rho}}{dy} = C \ln \bar{\rho} + \ln K \quad (12)$$

in which $\ln K$ is an integration constant. Simplifying, we obtain

$$\frac{d\bar{\rho}}{dy} = K \bar{\rho}^C \quad (12)'$$

After shifting the terms, we obtain

$$\frac{d\bar{\rho}}{\bar{\rho}^C} = K dy$$

Then after integrating, we obtain

$$\frac{1}{1-C} \bar{\rho}^{1-C} = K(y+y_0)$$

in which " y_0 " is an integration constant. After simplifying, we obtain

$$\bar{\rho} = [K(1-C)]^{\frac{1}{1-C}} (y+y_0)^{\frac{1}{1-C}}$$

Let

$$n = \frac{1}{1-C}, \quad K' = [K(1-C)]^{\frac{1}{1-C}} \quad /54$$

we obtain

$$\bar{\rho} = K' (y+y_0)^n \quad (13)$$

Further, let

$$\bar{\eta} = \frac{y}{\delta}$$

After dividing " $\bar{\rho}$ " with " $\bar{\rho}_\infty$ ", we obtain

$$\frac{\bar{\rho}}{\bar{\rho}_\infty} = K' (y+y_0)^n \quad (14)$$

This non-dimensional equation expresses the mean density.

IV. Comparison: Theory and Experiment

Let us use the graphic method to find the accuracy of the equation by using the x abscissa to represent the data calculated from the equation (14) and the ordinate to represent the experimental data. If the calculated results agree with the experiment results, then all the corresponding points should fall on a 45° line from origin. The comparisons are displayed in Figures 1, 2 and 3. We can see that all the points are practically falling on the 45° line in each figure. These figures explain that except on both ends of each line (which show some deviation) the theoretical calculated data essentially agree with the experimental results.

V. Discussion

It is concluded that the similarity assumption is quite approximate, yet it is practical for application.

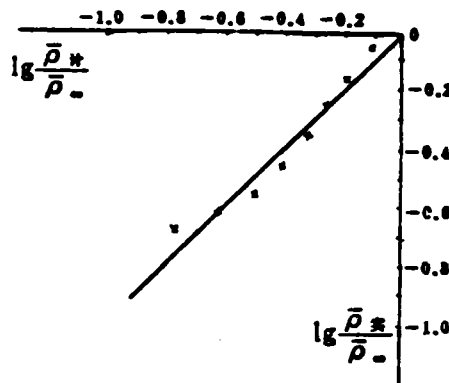


Figure 1. $P_0 = 3200\text{cmHg}$, $d = 4 \text{ inch}$, $n = 0.98$, $n_0 = 0.15$,
 $K' = 0.606$

1. calculated
2. experimental

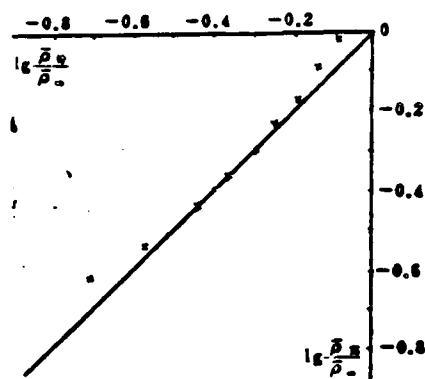


Figure 2. $P_0 = 1700 \text{ cmHg}$, $\sigma = 4.5 \text{ inch}$, $n = 0.92$, $\eta_0 = 0.13$, $K' = 0.71$

1. calculated
2. experimental

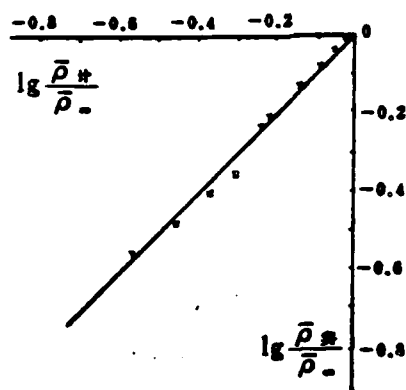


Figure 3. $P_0 = 500 \text{ cmHg}$, $\sigma = 6 \text{ inch}$, $n = 0.88$, $\eta_0 = 0.15$, $K' = 0.96$

1. calculated
2. experimental

References

/55

- [1] Zhou Paiyuan, Journal of Mechanics, 3, 4 (1959), 281-297.
Chinese Science, 8 (1959), 1095-1119.
- [2] Zhou Paiyuan, Quarterly of Applied Mathematics, 5, 3
(1947), 346-353.
- [3] Cai Shutang, Symposium of Theoretical Physics and
Mechanics, 161-185 (1984), Science Publishing Co.
- [4] NASA, N75-33347.

The Engineering Numerical Technique for the Determination
of the Inviscid Flow Field Heating Rate on Ballistic
Re-entry Vehicles

Yang Maozhao, He Fangshang

(China Aerodynamic Research and Development Center)

Abstract

RVSPHR (The Ballistic Re-entry Vehicle's Shock Pressure and Heating Rate Computer Code) is an approximate numerical technique for the determination of the inviscid aerodynamics and heat transfer of re-entry vehicles. In the transonic flow region surrounding the nose stagnation point, the distribution of the surface pressure and the shock angles is assigned from the correlation. With the assumptions for the profiles of pressure and normal velocity along body-normals in Von Mises coordinates, local iteration is carried out at each normal to determine the shape of the shock wave based on mass continuity satisfied along that normal. In the downstream supersonic regions, the exact Euler equations of motion are integrated using the finite-difference method. The surface heating rate is calculated using a non-inviscid flow. All calculated results are compared with more rigorous solutions as well as experimental results and good agreements have been found.

I. Introduction

The determination of the aerodynamic characteristics using the numerical technique of inviscid flow and the analysis of the aerodynamic heating process using numerical calculation of the boundary layer have been successfully carried out. However, since the rigorous numerical calculation is time consuming and costly, it has not been widely employed for carrying out the initial engineering estimations in certain applications. For engineering application, we have used engineering approximate solutions for treating the transonic region in rigorous inviscid

flow calculation. The iterative numerical procedure in solving the elliptic equations for the subsonic region surrounding the nose stagnant point is avoided. This simplifies greatly the problem of the subsonic region and accelerates the calculation without sacrificing much of the accuracy or affecting the solution of the downstream supersonic region. With this approach, we have determined the correlation equation of the surface pressure distribution and the shock angles in the transonic region around the nose as well as the profiles of pressure and normal velocity along body-normals in the shock wave layer. The position of the shock wave corresponding to each normal on the surface is determined by local iteration or overall iteration based on mass conservation. The solution of the transonic region provides the preliminary data of the profiles for calculating the downstream supersonic region. The exact Euler equations of motion for the supersonic region are integrated using a numerical technique with the finite-difference method.

Although this technique for determining the inviscid flow field is an approximate method, it is a technique for calculating the overall flow field in regarding the estimation of pressure distribution and the shape of the shock on the aircraft. It provides the necessary data for boundary layer calculations with consideration of the effects of entropy swallowing. Based on this technique, we have further derived a method of integration with the momentum in the boundary layer and a method of entropy swallowing calculation relating to mass balance of the flow. The new technique does not need to carry out iterations on the parameters of the outside edge of the boundary layer and much less computer time is required in calculating the boundary parameters and the surface heating rate.

We have carried out calculations on many aircrafts and wind tunnel test models. The results are in good agreement with these obtained from more rigorous solutions and experimental data. There are also significant savings in computer time.

Manuscript submitted Mar. 24, 1983, revised June 18, 1983

(1) Technique for the Determination of the Inviscid Flow

The purpose of this technique is to avoid the iterative calculation in solving the elliptic equation in the subsonic flow region surrounding the front edge of the passive nose. The following approximations and assumptions are made in the calculation of the transonic flow region around the nose:

1. The pressure distribution in the transonic region (from stagnation point to the sonic point) is determined using engineering equations. Love's modified equation^[1] is used in the calculation of the upstream region of the sonic point. Matched Newtonian equations with Prandtl-Meyer expansion are used for the region after the sonic point. The equations by curve fitting for the latter are shown in the following:

For $M \leq 1.2$,

$$p = p_0 \{ 1 + 1.08 \sin^2 [(\pi/2) - \theta] [\exp(-4\sqrt{\ln s^*/s}) - 1] - 0.468 \exp(-4\sqrt{\ln s^*/s}) \}$$

2.1-1

For $M > 1.2$,

$$p = p_0 \left\{ 1 - \left[1.46143 - 0.51143 \sin \left(\frac{\pi}{2} + \theta^* - \theta - \frac{50}{180} \pi \right) \right] \sin^2 \left(\frac{\pi}{2} + \theta^* - \theta - \frac{50}{180} \pi \right) \right\}$$

2.1-2

Where θ , s , θ^* , s^* are the dip angle and arc length of the surface at local point and the sonic point respectively. P_0 is the pressure at the stagnation point, which can be expressed by the following equation with ideal gas:

$$p_0 = p_\infty \left(\frac{\gamma+1}{2} M_\infty^2 \right)^{\frac{\gamma}{\gamma-1}} \left(\frac{\gamma+1}{2\gamma M_\infty^2 - \gamma + 1} \right)^{1/(\gamma-1)}$$

2.1-3

For equilibrated air, it should be calculated by iteration from the relations of the thermodynamic characteristics using the entropy behind the normal shock wave and the accurate enthalpy, h_s , at the stagnation point. All quantities used in this paper are dimensional and in metric system.

2. In the shock wave layer with relatively small spherical angle, the profile of the normal velocity on the surface other than the flow at the stagnation point can be correlated with the profile at the stagnation point using the following equation:

$$v(\psi) = \frac{v_0(\xi)}{v_0(y_s)} \cdot v(\psi_s) \quad 2.1-4$$

where $v_0(\xi)$ is the normal velocity distribution of the flow at the stagnation point. $v_0(y_s)$, $v(\psi_s)$ are the normal velocities behind the shock wave at and away from the stagnation point respectively. The values are fixed with given shape of the shock wave. $v_0(\xi)$ can be determined using the pressure distribution of the flow at the stagnation point. According to the numerical technique for the determination of the inviscid flow^[2], $p_0(\xi)$ can be fitted in the following equation:

$$p_0(\xi) = p_0 + (p_{sks} - p_0)\xi^{2.855336} \quad 2.1-5$$

where p_{sks} is the pressure behind the normal shock wave. From Equation (2.1-5), the enthalpy distribution, $h_0(\xi)$, can be calculated and the following equation is obtained:

$$v_0(\xi) = \sqrt{gJ[h_0 - h_0(\xi)]} \quad 2.1-6$$

In Von Mises coordinates, the relationship of the flow function and the normal coordinate y is

$$d\psi = \rho u r dy \quad 2.1-7$$

which gives

$$y = \frac{r_s}{\cos\theta} \left[\sqrt{1 + \frac{2 \cos\theta}{r_s}} \int_0^{\psi} \frac{1}{\rho u} d\psi - 1 \right] \quad 2.1-8 \quad /58$$

In the region near the stagnation point, using

$$\xi = y_0/y_{s0} = y/y_s \quad 2.1-9$$

the ξ value corresponding to each point y in the flow at the

stagnation point can be easily calculated.

3. The following profile of pressure along body-normals in the shock wave layer is assumed:

$$p(\psi) = p_b + (p_{sh} - p_b)(\psi/\psi_s)^2 \quad 2.1-10$$

where p_b is the estimated surface pressure from previous engineering equations, p_{sh} is the value of the pressure behind the shock wave in the profile.

4. The initial shape of the shock wave is

$$y_{i,k} = y_{i,k-1} + y'_{i,k-1} dx \quad 2.1-11$$

$$y'_{i,k-1} = (1 + y_{i,k-1}/R) \operatorname{tg}(\beta_{i,k-1} - \theta_{i,k-1}) \quad 2.1-12$$

$$\beta_{i,k-1} = 0.5326 + 0.3333 \theta_{i,k-1} + 0.2122 \theta_{i,k-1}^2 \quad 2.1-13$$

The above calculations can be carried out if the distance, $y_{sh,0}$, from the body to the shock wave on the flow line at the stagnation point is available. The value of $y_{sh,0}$ can be calculated from:

$$y_{sh,0} = \left(0.128 + \frac{0.77}{M_\infty^2} - 0.025 \sqrt{\rho_{sh}/\rho_\infty - \frac{6 M_\infty^2}{5 + M_\infty^2}} \right) R, \quad 2.1-14$$

For an ideal gas the following equation may be used

$$y_{sh,0} = \left(0.13 + \frac{0.6137}{M_\infty^2 - 1} \right) R, \quad 2.1-15$$

After obtaining the values of the flow field parameters, p and u , of the calculating cross-section, the new position of the shock wave y_s can be determined by the requirement of mass continuity, which gives

$$y_s = \frac{r_s}{\cos \theta} \left[\sqrt{1 + \frac{2 \cos \theta}{r_s} \int_0^\psi \frac{1}{\rho u} d\psi} - 1 \right] \quad 2.1-16$$

Since the calculated position of the shock wave may not be consistent with the original position assigned, additional iterations are necessary until the results of consecutive

iterations show the desired accuracy. This is the local iteration process for obtaining the shape of the shock wave. With this calculation technique, we have also developed an overall iterative procedure. After obtaining the positions of the shock wave on the cross-sections along all body-normals by local iterative procedure, the new distribution of the shock angles, β'_{sh} , can be obtained by parabolic fit or spline fit of the shape of the shock wave. Equation:

$$\beta_{sh(n+1)} = \beta_{sh(ol d)} + \epsilon_1 [\beta'_{sh} - \beta_{sh(ol d)}] \quad 2.1-17$$

is used to replace the old equation of the shock angles (2.1-13) and a new local iteration for the profile along each body-normal is carried out for further improving the estimation of the position of the shock wave. Better convergency of the calculation can be obtained with $\epsilon_2 = 0.2 \sim 0.6$.

The above calculation is carried out from one cross-section to next cross-section starting from the point near the stagnation point until the velocity u reaches the sonic velocity at one particular cross section. After that the calculation should be carried out following the procedure for supersonic region.

Since the calculation in the supersonic region is carried out in boundary layer coordinate system (s, y) , which is different from the Von Mises coordinate system (s_r, ϕ) and the preliminary cross-section data for the calculation should be obtained by interpolation, the simultaneous equations, as shown in the following vectors, for calculation of the supersonic region can be derived from Euler equations of motion for the stable, inviscid and compressible axisymmetric body.

$$\frac{\partial \zeta}{\partial \xi} + A \frac{\partial \zeta}{\partial \xi} = -\pi \quad 2.1-18 \quad /59$$

where

$$\zeta = \begin{bmatrix} p \\ \sigma \\ s \end{bmatrix}$$

$$\Lambda = \begin{bmatrix} \frac{A+C}{E} & \frac{\rho a^2 H}{E y_1} & 0 \\ \frac{1}{\rho u^2} \left(\frac{A\sigma + C\sigma}{E} + \frac{H + \sigma\eta}{y_1} \frac{\partial y_1}{\partial x} \right) & \frac{A+C}{E} & 0 \\ 0 & 0 & A \end{bmatrix}$$

$$\pi = \begin{bmatrix} \frac{\rho a^2 H}{r E} (\sin \theta + \sigma \cos \theta) \\ \frac{\sigma H a^2}{r E u^2} (\sin \theta + \sigma \cos \theta) - \frac{1 + \sigma^2}{R} \\ 0 \end{bmatrix}$$

$$A = \frac{\sigma H - \eta \frac{\partial y_1}{\partial x}}{y_1}$$

$$C = \frac{a^2 \eta}{u^2 y_1} \frac{\partial y_1}{\partial x}$$

$$E = 1 - (a^2/u^2)$$

$$a = -\left(\frac{\partial s}{\partial \rho}\right)_p / (\partial s / \partial p)_p \quad s - \text{熵}$$

$$a - \text{音速}$$

$$\xi = x$$

$$\eta = y/y_1(x)$$

$$\sigma = v/u$$

$$H = 1 + (y/R)$$

$$R = -1 / \frac{\partial \theta}{\partial x} = -\cos \theta / \frac{d^2 r}{dx^2}$$

$$r = r_1 + y \cos \theta$$

At point $\xi = (n + \bar{\theta})\Delta\xi$, $\eta = [m + (1/2)]\Delta\eta$, $\bar{\theta} = 0.625$ the above equations can be rearranged in implicit forms to give:

$$\Gamma_{n+\frac{1}{2}} \zeta_{n+\frac{1}{2}} + \Delta_{n+\frac{1}{2}} \zeta_n = \Pi_{n+\frac{1}{2}} \quad 2.1-19$$

$$\Gamma_{n+\frac{1}{2}} = 1 + 2\bar{\theta} \frac{\Delta\xi}{\Delta\eta} A_{n+\frac{1}{2}}^{\bar{\theta}}$$

where

$$\Delta_{n+\frac{1}{2}} = 1 - 2\bar{\theta} \frac{\Delta\xi}{\Delta\eta} A_{n+\frac{1}{2}}^{\bar{\theta}}$$

$$\Pi_{n+\frac{1}{2}} = \left[1 - 2(1 - \bar{\theta}) \frac{\Delta\xi}{\Delta\eta} A_{n+\frac{1}{2}}^{\bar{\theta}} \right] \zeta_{n+\frac{1}{2}} + \left[1 - 2(1 - \bar{\theta}) \frac{\Delta\xi}{\Delta\eta} A_{n+\frac{1}{2}}^{\bar{\theta}} \right] \zeta_n - 2\Delta\xi \pi_{n+\frac{1}{2}}^{\bar{\theta}}$$

and I is the unit matrix. Two of the elements can be expressed as

$$2A_{n+\frac{1}{2}}^{*+1} = \bar{\theta} (A_{n+\frac{1}{2}}^{*+1} + A_{n+\frac{1}{2}}^{*+1}) + (1 - \bar{\theta}) (A_{n+\frac{1}{2}}^{*+1} + A_{n+\frac{1}{2}}^{*+1})$$

$$2\pi_{n+\frac{1}{2}}^{*+1} = \bar{\theta} (\pi_{n+\frac{1}{2}}^{*+1} + \pi_{n+\frac{1}{2}}^{*+1}) + (1 - \bar{\theta}) (\pi_{n+\frac{1}{2}}^{*+1} + \pi_{n+\frac{1}{2}}^{*+1})$$

The solution of the above finite-difference equations can be obtained by the catching up technique. The recurrence relations of the coefficients are as follows: /60

$$\mu_{n+1} = \frac{\mu_n \Delta_{n+\frac{1}{2}}^{-1} \Gamma_{n+\frac{1}{2}}}{\|\mu_n \Delta_{n+\frac{1}{2}}^{-1} \Gamma_{n+\frac{1}{2}}\|} \quad 2.1-20$$

$$G_{n+1} = \frac{\mu_n \Delta_{n+\frac{1}{2}}^{-1} \Pi_{n+\frac{1}{2}} - G_n}{\|\mu_n \Delta_{n+\frac{1}{2}}^{-1} \Gamma_{n+\frac{1}{2}}\|} \quad 2.1-21$$

where $\Delta_{m+\frac{1}{2}}^{-1}$ is the inverse of $\Delta_{m+\frac{1}{2}}$, $\|\dots\|$ represents the determinant.

In addition

$$\mu_{n+1} \zeta_{n+1} = G_{n+1} \quad 2.1-22$$

With impermeable body surface, $\sigma = 0$, then

$$\begin{aligned} \mu_n \zeta_n &= G_n \\ \mu_n(0, 1, 0) \end{aligned} \quad 2.1-23$$

where

$$G_0 = 0$$

Therefore, the values of μ_M , G_0 within the shock wave can be determined by the recurrence relations starting from the surface of the body. Combining with the shock wave condition of Rankine-Hugoniot, ξ_{M0} is readily obtained from the relation of the shock wave:

$$\mu_M \zeta_M = G_M$$

Then, the values of

$$\zeta_{M-1}, \zeta_{M-2}, \dots, \zeta_0$$

can be obtained from the finite-difference equation (2.1-19) by calculating back to the surface.

II. Improved Entropy Swallowing Technique

It is well known that the effects of entropy swallowing of the boundary layer are usually determined by mass balance. The mass flow swallowed by the boundary layer should be equal to the mass flow which passes through the bow shape shock wave along the inviscid flow. The equation of mass conservation of the flow path can be written as

$$\frac{1}{2} \rho_{\infty} u_{\infty} r_s^2 = \rho_e u_e r \theta_M \quad 2.2-1$$

where the momentum thickness of the boundary layer, θ_M , can be determined from the following axisymmetric equation of momentum:

$$\frac{d\theta_M}{ds} = \frac{1}{2} c_f - \theta_M \left(\frac{2+H_c}{u_e} \frac{du_e}{ds} + \frac{1}{\rho_e} \frac{d\rho_e}{ds} + \frac{1}{r} \frac{dr}{ds} \right) \quad 2.2-2$$

Iterations are needed to converge the values on both sides of equation (2.2-1). The estimated shock angle (or shock height r_s) as well as the values of the parameters p_c , u_c and M_c should be modified continuously. The convergency can be tested by substituting the value of θ determined from equation (2.2-2) in equation (2.2-1). This is the iterative process used previously for entropy change. In our analysis, the axisymmetric integration equation of momentum is written in terms of the total differential form of the mass flow. Equation (2.2-2) is rewritten as

$$\frac{d}{ds} (\rho_e u_e r \theta_M) = \frac{1}{2} \rho_e u_e r c_f - (1+H_c) (\rho_e u_e r \theta_M) \frac{1}{u_e} \frac{du_e}{ds} \quad 2.2-3$$

where H_c is the mode parameter depending on the flow. It can be /61 written in the following two expressions for laminar and turbulent flows respectively.

For laminar flow:

$$H_c = 2.59156 h_e/h_s + h_s/h_e - 1 \quad 2.2-4$$

For turbulent flow:

$$I_1 = \int_0^1 \frac{h_s(z' - z^4)}{h_s + (h_s - h_e)z + (h_e - h_s)z^2} dz$$

$$I_2 = \int_0^1 \frac{h_s z'}{h_s + (h_s - h_e)z + (h_e - h_s)z^2} dz \quad 2.2-5$$

where

$$c_f = \frac{2Pr^{1/3} \dot{q}_w}{g \rho_c u_c h_c} \quad (2.2-6)$$

c_f can be related to the heat flux, \dot{q}_w , by Reynold's analogy. It should be noted that equation (2.2-3) is different from equation (2.2-2). The mass flow $p_c u_c r_M^{\theta}$ is considered to be a single parameter and it can be calculated by Euler's method or Runge-kutta method of integration utilizing the solution of the inviscid flow. r_s is then obtained from equation (2.2-1) and the entropy behind the shock wave at position r_s can be calculated by interpolation from the shape of the inviscid shock wave. The peripheric parameters at the outer edge of the boundary layer, p_c , u_c , h_c , M_c can be calculated along the flow using the pressure distribution of the inviscid flow. Iterative modifications of the value of du_c/ds in equation (2.2-3) are carried out. The above calculation is made repeatedly with newly calculated u_c value until the convergency is reached. Practically, the convergency can be reached shortly. It takes much less computer time than the technique of variable entropy with iterative calculation on all the peripheric parameters such as p_c , u_c and h_c . This is an improved numerical technique of variable entropy.

III. Results of Calculation and Comparison

All calculated results of the inviscid flow, including shock shape, surface pressure distribution and the flow field profiles through the shock layer, are compared with more rigorous numerical solutions^[2] as shown in Figures 1, 2 and 3. Calculations are carried out on a semiconic body having a cone angle of 10° at various Mach numbers and elevations with equilibrated air and ideal gas. The results indicate that the shock shape and surface pressure distribution are quite consistent with vigorous numerical solutions. The position of

shock wave determined by local iteration and the off-body distance of the shock wave at the stagnation point obtained by parabolic interpolation are compared with rigorous numerical solutions and show relative deviations within 1.1% to 1.8% as listed in Table 1. The density and velocity profiles of the flow in the shock layer at $M_\infty = 2.0$ are in good agreement with reference [2]. Some deviation of the pressure profile is observed near the body surface, while good agreement is approached near the shock wave.

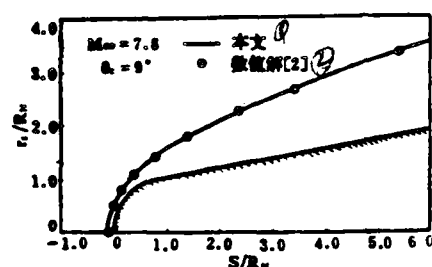


Figure 1. Shock Shape

1. our result
2. numerical solutions of [2]

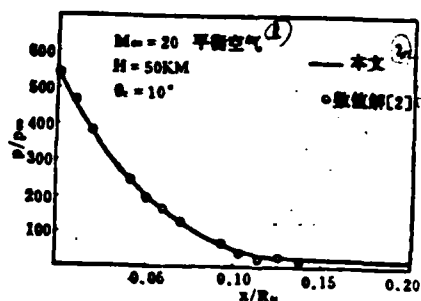


Figure 2(a). Surface Pressure Distribution on the Nose

1. ideal gas
2. our result
3. numerical solutions of [2]

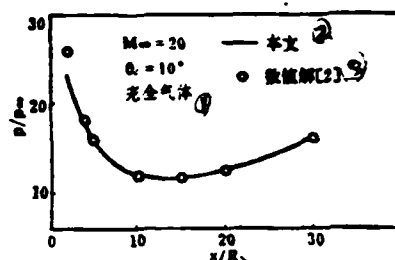


Figure 2(b). Surface Pressure Distribution on the Body

1. ideal gas
2. our result
3. numerical solutions of [2]

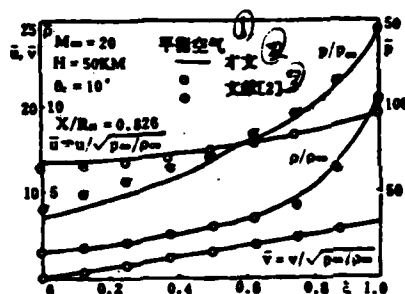


Figure 3. The Flow Field Profiles in the Shock Layer

1. equilibrated air
2. our result
3. numerical solutions of [2]

Obviously, the approximation technique for the transonic flow region does not cause significant error in overall calculation of the inviscid flow field and much less computer time is required than more rigorous solutions. This technique is very effective and feasible in engineering applications.

Table 1

$\frac{V_{1.0}}{R_N}$		本 文	文献[2]
	平衡空气	0.055	0.054
	完全气体	0.1315	0.1300

Key on following page.

1. equilibrated air
2. ideal gas
3. our result
4. reference [2]

We have also made a calculation based on the experimental model of Widhopf^[3]. The pressure distribution is shown in Figure 4. The calculated results are in good agreement with the experimental results. The calculated heat flux at various flow conditions is shown in Figures 5, 6 and 7. The experimental results of reference [3] and the boundary layer numerical solutions of reference [4] are also shown in the figures. Our calculated results are quite satisfactory in comparison.

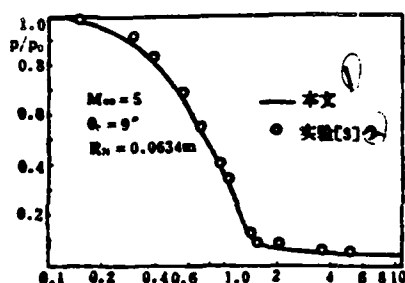


Figure 4. Comparison of the Calculated Pressure Distribution With Experimental Data

1. our results
2. experimental data of [3]

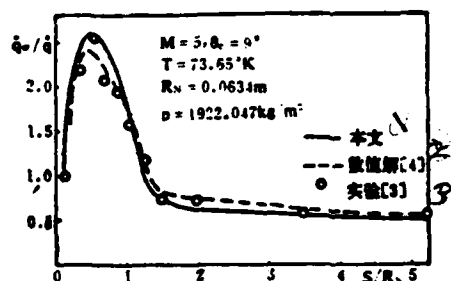


Figure 5. Distribution of Heat Flux

1. our results
2. numerical solutions of [4]
3. experimental data of [3]

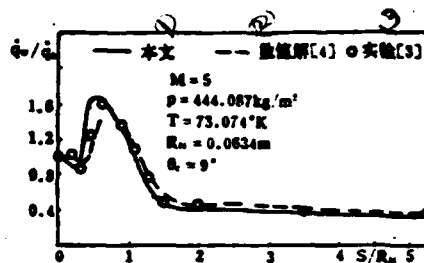


Figure 6. Distribution of Heat Flux

1. our results
2. numerical solutions of [4]
3. experimental data of [3]

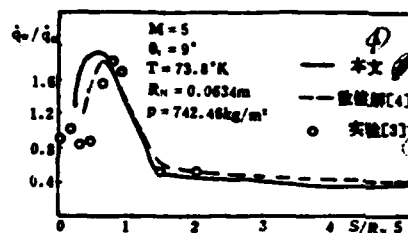


Figure 7. Distribution of Heat Flux

1. our results
2. numerical solutions of [4]
3. experimental data of [3]

Our numerical technique can be extended to three dimensional calculation with angle of attack using suitable coordinate transformation and analogical approximation of axisymmetry.

References

/63

- [1] Love, E.S., Woods, W.C., Rainey, R.W., AIAA Paper 69-181.
- [2] Lyuvimov, A.N., Rusanov, V.V. Gas Flow Around Solids, II.
- [3] Widhopf, G.F., AD-7 48292.
- [4] Pan, M.L., and Z.Q. Liu, "Finite-Difference Solutions of Turbulent Boundary Layer Equations" China Aerodynamic Research and Development Center, Nov. 1980.

- [5] Yang, M.Z., "An Effective Engineering Numerical Technique for Aerodynamics and Heating Rate of the Cone Shape Body", Report Presented in Conference of Experimental and Engineering Techniques for High Supersonic Speed., 1982.
- [6] He, F.S., "Calculation of the Flow Field on Ablative Body with Small Angle of Attack" Report Presented in Conference of Experimental Techniques of High Supersonic Speed, Dec. 1982.

Visualization of Three Dimensional Separated Flows Using the Smoke Wire Technique

Xia Xuejian

(Beijing Institute of Aeronautics and Astronautics)

Abstract

The smoke wire technique is used for visualizing the vortex flow at the wake of an axisymmetric body and the asymmetric vortices which emanated from the nose of the aircraft at high angle of attack. The smoke wire technique can be employed for automatic photographs, by the sequential circuit, conditional photographs or manual operation.

I. Introduction

Various techniques for visualization of the flows have been applied in aerodynamic research, especially in some complicated flows such as the separated flow, jet flow and wake flow emanating from wings and the fuselage at high angles of attack. They are also effective tools for studying the separated flow and the structure of the turbulence on nonflying passive bodies. Recently, various new techniques for visualizing the flows have been explored.

The smoke wire technique has been applied since the fifties. Recently, this technique has been gradually used in the visualization of complicated flows. Reference [1] employed this technique to visualize the bubble separation of the laminar flow and the transition of the boundary layer of the flow about the wings. It indicates that the technique can be used in flows which cannot be measured by hot wire probe or pressure transducer. We have used the smoke wire technique in studying the three dimensional separated flows such as the wake flow on a three dimensional passive body. The flow pattern exhibited was consistent with the measurements obtained with hot wires. Various periodic characteristics of the flow were observed

visually. This technique has also successfully detected the presence of asymmetric vortices emanating from the nose of the body at high angles of attack without lateral gliding in wind tunnel experiments. Since the smoke lines are very thin, detail flow pattern can be observed. This technique can be widely used in research for its convenience and less environmental pollution.

The limitation of this technique is on the wind speed of the test. It cannot be applied at high Reynolds Number. Reference [2] has compared in detail the characteristics of the separated flows on wings, fuselage and whole body at high angles of attack tested in water tunnel, wind tunnel and test flight at corresponding limits of the Reynolds Number. It also analyzed the effect of Reynolds Number on the separated flows. Since the separated flows around sharp edges or fixed edges are less sensitive to Reynolds Number, the smoke wire technique can provide more quantitative measurement on the flow pattern. Additional analyses are necessary for more complicated flows which are affected by the Reynolds Number. The flow spectrum on a fuselage at high angles of attack using smoke wire technique can provide qualitative information.

II. The Equipment for Smoke Wire Display and the Technique of Operation

Figure 1 shows the equipment of smoke wire display for studying the wake flow. The system consists of three positions:

the first portion is the smoke generator, which is located in the wind tunnel. The second portion is the process electrical system, which includes power source for heating the smoke wire /72 and the synchro control box. The third portion is the light source, camera and the activation system (the portion in the dark shown in the picture).

AD-A155 480 ACTA AERODYNAMICA SINICA(U) FOREIGN TECHNOLOGY DIV 272
WRIGHT-PATTERSON AFB OH 30 APR 85 FTD-ID(R5)T-1168-84

AD-A155 480 ACTA AERODYNAMICA SINICA(U) FOREIGN TECHNOLOGY DIV 272
WRIGHT-PATTERSON AFB OH 30 APR 85 FTD-ID(R5)T-1168-84

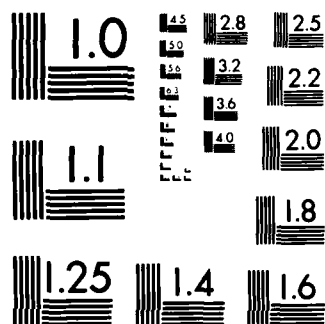
AD-A155 480 ACTA AERODYNAMICA SINICA(U) FOREIGN TECHNOLOGY DIV 272
WRIGHT-PATTERSON AFB OH 30 APR 85 FTD-ID(R5)T-1168-84

UNCLASSIFIED F/G 20/4 NL

UNCLASSIFIED F/G 20/4 NL

UNCLASSIFIED F/G 20/4 NL

[illegible]



MICROCOPY RESOLUTION TEST CHART
NATIONAL BUREAU OF STANDARDS-1963-A

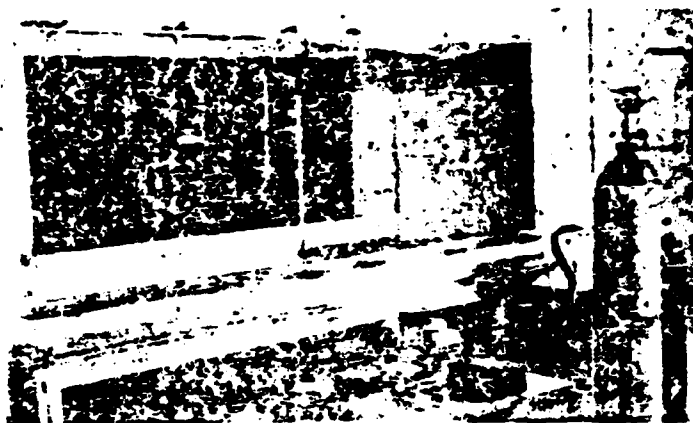


Figure 1. Equipment for Smoke Wire Display

1. The Smoke Wire Generator and the Operation

Figure 2 shows the smoke wire generator which is composed of resistance wire, supporting frame, the feedback passage of the resistance wire. The resistance wire is for generating the smoke by heating. It can be a tungsten wire, nichrome wire or stainless steel wire. Stainless steel wire is more favorable since it has high resistivity, fixed strength and less tendency to become brittle. The diameter of the resistance wire depends on the experiment. A size of 0.15mm is suitable in general. For certain flow conditions which may be distributed by the wire, the selection of the diameter should be more careful. Reference [1] provides some information on the selection of the wire. It should be noticed that the diameter of the resistance wire affects the smoking time. Since the diameters of the oil drops attached on a thin wire are smaller, the duration of smoking will also be shorter. The tension on the resistance wire will also affect the mass flow of the smoke. The equipment employs a tension bolt to adjust the length of the resistance wire.

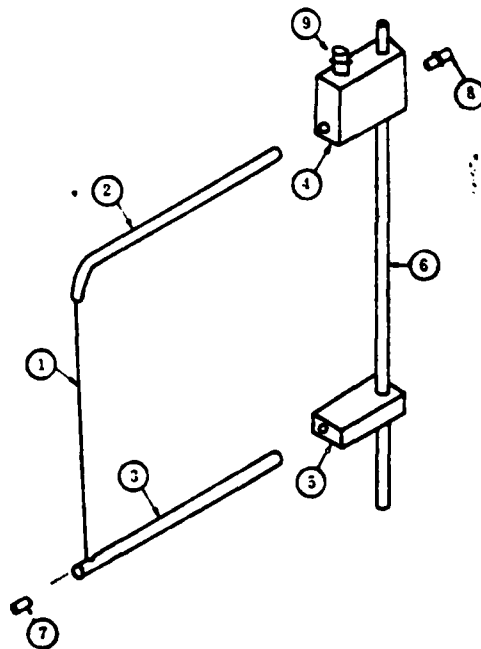


Figure 2. The Structure of the Smoke Generator

1. resistance wire
2. top bracket
3. bottom bracket
4. top support
5. bottom support
6. supporting pole
7. tension bolt for the steel wire
8. tension bolt for the steel wire
9. receptacle for conducting wire

Specially selected oils should be used for smoke generation. Smoke oil for model trains, paraffin oils as well as other oils have been used in experiments. Experimental results indicate that glycerine can provide longer smoking duration and more clear flow pattern. The smoking duration can be a few seconds with a wind speed of about 2 M/sec. The duration is long enough for taking photographs.

Various tests have been carried out for selecting a better method to coat the oil. The oil can be extruded from the top bracket by compressed air or dripped down from the top end of the resistance wire. It is found by experience that uniform distribution of oil, which gives uniform flow spectrum, can be

/73

obtained by coating manually on the resistance wire with a brush.

2. Electrical System of the Smoke Wire Process

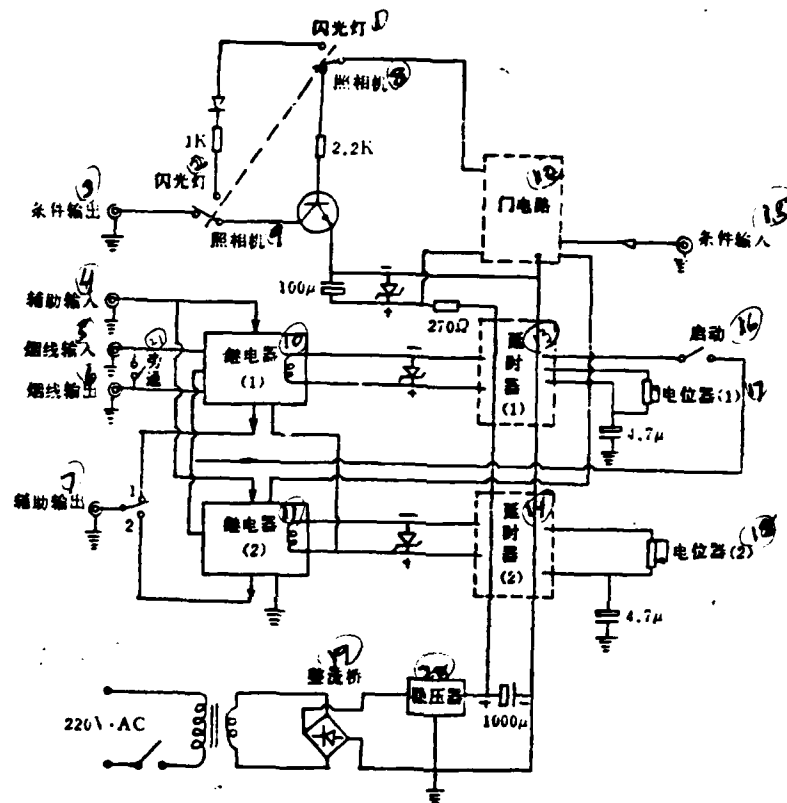


Figure 3. Circuit Diagram of the Synchro Box

1. flash light
2. flash light
3. conditional output
4. auxiliary output
5. smoke wire input
6. smoke wire output
7. auxiliary output
8. camera
9. camera
10. relay
11. relay
12. gate circuit
13. time delay unit
14. time delay unit
15. conditional input

- 16. initiate switch
- 17. potentiometer -1
- 18. potentiometer -2
- 19. rectifying bridge
- 20. voltage stabilizer
- 21. bypass switch

The sequence of activating the smoke wire and the camera is controlled by two time delay circuits. The first time delay unit controls the duration of the electric current which passes through the resistance wire for heating. The second time delay unit controls the delay time before activating the camera. The time duration of both units is adjusted by the potentiometer. The arrangement can be changed when using conditional input (the flow spectrum is obtained by activating the flash light at the occurrence of a special event). Figures 3 and 4 show the circuit diagram of the synchro box and the distribution of the process durations.

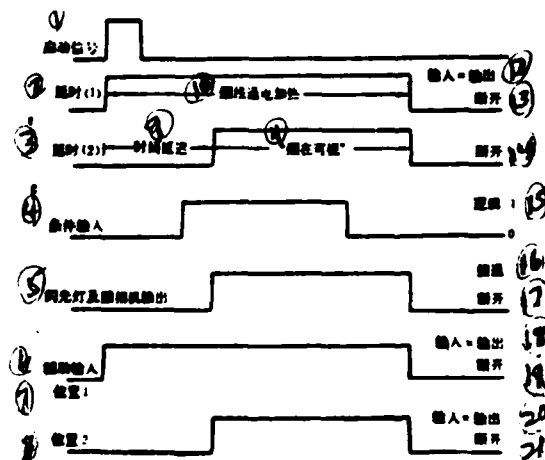


Figure 4. Diagram of the Process Durations

- 1. automatic signal
- 2. delay -1

3. delay -2
4. conditional input
5. output of the flash light and the camera
6. auxiliary output
7. position 1
8. position 2
9. delayed duration
10. heating the smoke wire by electricity
11. "smoke visualized"
12. input=output
13. switch off
14. switch off
15. logic 1
16. switch on
17. switch off
18. input=output
19. switch off
20. input=output
21. switch off

There are three types of "input" and "output" for the circuitry:

1) Power Input and Output for the Smoke Wire

The timing circuit of the smoke wire is on when the direct current with variable voltage is connected to the smoke wire input of the synchro box and the output is connected to the smoke generator. The "input" and the "output" is connected internally when the "bypass" switch is on, which bypasses the timing circuit. /74

2) Conditional Input and Output

This method can be used to photograph the flow pattern of a special event. The input signal in this mode should be compatible with the TTL circuit (integrated circuit of transistor-transistor logic). During working condition, the input voltage should be low (Figure 4) at the beginning and jumps to a high value when the event occurs. This causes the second timing circuit in high voltage at the same moment and provides output to activate the flash light and the camera. A low current (few mAs) triggering circuit can be used for activating the flash light. A momentary high current (up to 4 amps, 60 volts) triggering circuit should be employed to trigger the camera.

It should be noticed that the conditional photograph is usually carried out in the dark. The shutter of the camera is open when the "initiate switch" is on. The flash light is triggered and the film in the camera is exposed for recording when the conditional event occurs and the "smoke" is visible. The shutter of the camera is closed when the time is out. Usually the signals of the hot wire can be recorded simultaneously when the flash light is triggered. Therefore the flow pattern observed can be compared with the measurements of the hot wire for studying the flow structure.

3) Auxiliary Input and Output

This is a universal input which makes the system more flexible in application. It can provide an adjustable auxiliary output with time delay for any signal input. Usually the best flow spectrum can be observed a few moments after the resistance wire is heated. The auxiliary input and output can be used in such cases for photographing.

One of the above three types of input and output can be selected as needed for processing.

The principle and the working procedure of the synchro box of the process circuit have been discussed above. In addition to the synchro box, it needs a power supply with variable voltage for heating the resistance wire. The current should be about 2-3 amps and the variable voltage should be in the range of 0-100 volts. Figure 5 shows the circuit diagram of the power source for heating.

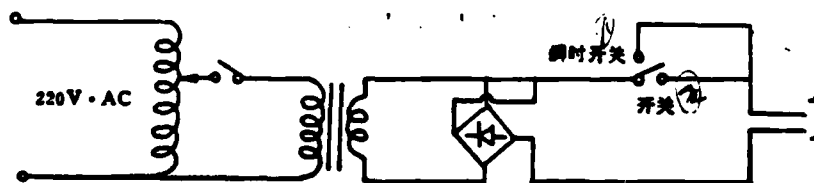


Figure 5. Circuit Diagram of the Power Source for Heating the Smoke Wire

1. momentary switch
2. switch

3. Light Source and the Photographic System

Strobe light was used as the light source on top of the wind tunnel for studying the wake flow. The frequency of the flash was adjustable from 1-13/sec. A plane light source was employed for obtaining the flow pattern of a cross-section of the three dimensional flow. The camera was a regular one of type 135. The shutter was activated by a compressed air switch controlled by the triggering circuit with the application of the auxiliary input/output.

Described above is the smoke wire technique which we have used to investigate the wake flow of a three dimensional passive body. Recently, we visualized the separated flow with positive results at high angle of attack using a simple manual operation. The equipment included a smoke generator, a coupling transformer and a resistance wire heated by AC. Pictures were taken at the best conditions depended on visual observation with naked eye. The smoke wire technique with manual operation is simple and easy when the conditional photograph is not necessary and manpower is available.

III. Examples of Visualization of the Three Dimensional Separated Flows Using Smoke Wire Technique

/75

Hot wire measurement of the wake flow of an axisymmetric body with declined base surface indicates that a strong periodic flow appears near the wake at certain angles of decline (such as 70° , 60°). The periodic phenomenon becomes less regular with a declining angle of 90° (vertical tail cut). The result has been demonstrated by visualizing with smoke wire. Pictures 3 and 2 of the flow patterns obtained by the smoke technique (with base angle of 70° and 90°) are shown in the inside back cover. The front end of the model was a semi-ellipsoid and the crabbing angle and angle of attack were zero.

Picture 1 indicates clearly the regular separation of the vortex which is more serious at the top than at the bottom. The same characteristic was also detected by hot wire measurement.

The separation of the vortex with a base angle of 90° as shown in Picture 2 was less regular than that at an angle of 70° , while the intensity was about the same from top to bottom. Intensive vortices occurred only occasionally. This characteristic is consistent with that obtained by hot wire measurement. The detailed results were reported in reference [3].

Picture 3 (inside back cover) is the photograph of the vortex flow emanating from the nose of the body at high angle of attack obtained by smoke wire technique. The flow pattern is quite similar to that obtained in water tunnel tests as reported in reference [2] (Figure 31 in reference [2]).

Figure 6 is a sketch of Picture 3. The model is at zero crabbing angle and with an angle of attack of 46° . The picture shows clearly two asymmetric vortices emanating from the front edge of the nose. The center portions of the vortices are shown in the picture. The vortex at the left side is at higher position than the one at the right side. The left vortex proceeded a longer distance before breaking apart while the one at the right side broke into spiral eddies moving in reversed direction. According to the analyses for slim fuselage in reference [2], the angle to initiate the asymmetric vortices is slightly retarded and the lateral position of the vortices is moved outward somewhat at low Reynolds Number. However, it has qualitatively recognized the asymmetry and the breakdown of the vortices.

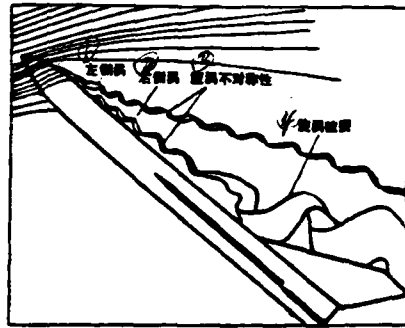


Figure 6. Sketch of the Breakdown of the Asymmetric Vortices at the Nose of the Fuselage

1. left vortex
2. right vortex
3. asymmetry of the vortex
4. breakdown of the vortex

Picture 4 (inside back cover) (from reference [4]) shows the back vortex on the right side of the body with an angle of attack of 31° . The swirl and the position of the center of the vortex are clearly observed.

IV. Conclusion

The smoke wire technique can be used to visualize the two and three dimensional stable flows as well as three dimensional separated flows. It can provide quantitative as well as qualitative information on the characteristics of the separated flows. It can be employed to take conditional photographs of the flow pattern at certain special occasions. The method is simple and flexible. It can provide the detailed structures of the flows. The smoke wire technique is an effective tool for studying complicated flows.

Picture 3 is photographed in cooperation with Shen Xialing of the Project Group.

References

/76

- [1] Batill S.M. and Mueller, T.J., AIAA Journal, 19, 3 (1981)
- [2] Erickson, G.E., 'Vortex Flow Condition', ICAS Paper No.82-6.6.1.
- [3] Xia, X.J. and Bearman, P.W., Aero. Quart., Vol. 34 Feb. 1983, Part 1.
- [4] Wang, Z.Y., Chen, N.X., and Zhao, S.C., Beijing Institute of Aeronautics and Astronautics, Research Report BH-B924 (1982).

VISUALIZATION OF THREE DIMENSIONAL SEPARATED FLOWS USING THE SMOKE WIRE TECHNIQUE

Xia Xuejian

(Beijing Institute of Aeronautics and Astronautics)

Abstract

The smoke wire technique is used for visualization of the vortex flow in the near wake of an axisymmetric body and the asymmetric vortices which emanate from the nose of body at high angles of attack, as well as the vortex breakdown above the wing. The smoke wire technique is available for automatic photograph by the sequential circuit, conditional photographs or manual operation.

The Application of Surface Hot Film in Aerodynamic Testing

Wang Tiecheng

(Nanjing Aeronautical Institute)

Abstract

Investigation of the boundary layer by means of measuring the magnitude and direction of the wall shear stress is very important in aerodynamic research. Surface hot films provided a new method for this study. This paper was written on the basis of development and testing of the surface film. The basic methods of experiment and limits of application were introduced with our typical experimental results.

Introduction

When air flows along a wall surface (solid surface), the shear stress, τ_w , is

$$\tau_w = \mu \left. \frac{\partial u}{\partial y} \right|_{y=0} \quad (1)$$

where μ is the (dynamic) viscosity of the air, u is the velocity of the air along the x axis.

Using surface hot films to measure the surface shear stress has many advantages. Since the hot film is attached to the wall and is parallel to the surface, the interference of the flow is small. It can be applied in conditions of low and high pressure gradients. It has high sensitivity to frequency response and can be used to measure the dynamic change of the surface shear stress. It can also be employed to measure the direction of the wall shear stress. When the surface hot film is employed to measure the absolute value of the wall shear stress, it is necessary to calibrate the hot film. The calibration is usually quite complicated. However in many boundary layer experiments, only the relative magnitude and the relative change of the wall shear stress are required to be measured and the calibration of the hot film is not necessary.

The first hot film successfully developed in China, the M-1 hot film, had been certified by the Technical Group of the Department of Aeronautical Technology in October, 1982. It had been formally used in aerodynamic experiments. This article was written based on the development and experiments of the M-1 hot film.

Structure and Theory

There are three types of hot film depending on the difference of the structure: type M, type B and type C. They are composed of the [Fig 1] substrate, heating film and lead wires. The substrate of type M [Fig 2] hot film is a flexible, heat-resisting plastic film. On top of it there are dual heating films distributed in V-shape. The substrate for type B hot film is a cylindrical insulator. The single hot film is located at the left end surface of the cylinder (as shown in Figure 2a). The lead wires are at the right end.

The advantage of this type of hot film is that it contains a /78 metal protective jacket (Figure 2b and 2c) and is convenient in installation. Type P (see Figure 3) is basically similar to type B. The only difference is that it has a shorter substrate cylinder. It looks like a disk and does not have the protective jacket. Both type P and type M hot films use adhesive to attach to the wall, while type B hot film can be attached to the holes of the wall by friction force. All three types of hot films should be in parallel to the surface when attached to the wall.

Heat is generated when electricity is passed through the heating film on the wall. When air is forced to flow along the surface of the wall, the process of heat transfer between the wall and air is usually called the forced convection heat transfer. The magnitude and the direction of the shear at the surface of the wall can be measured by the amount of heat transferred by forced convection. The following equations are

obtained theoretically:

$$Nu \propto \tau_w^{1/2} \quad (2)$$

$$F = \frac{Nu_1 - Nu_2}{Nu_1 + Nu_2} \propto \theta \quad (3)$$

where Nu is the Nusselt number (dimensionless heat) of the forced convection heat transfer between the wall surface and the air flow, θ is the angle between the direction of the wall shear stress and the symmetric line of the dual heated films (Figure 5), F is the parameter related to the direction of the shear stress on the wall surface, subscripts 1 and 2 refer to the two heating films.

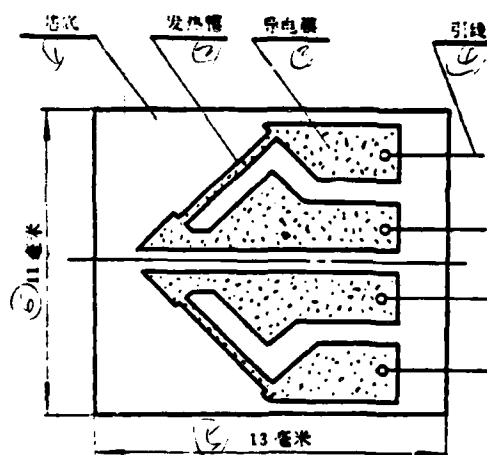


Figure 1. Type M-1 Surface Hot Film

1. substrate
2. heating film
3. conductive film
4. leading wire
5. 13 mm
6. 11 mm

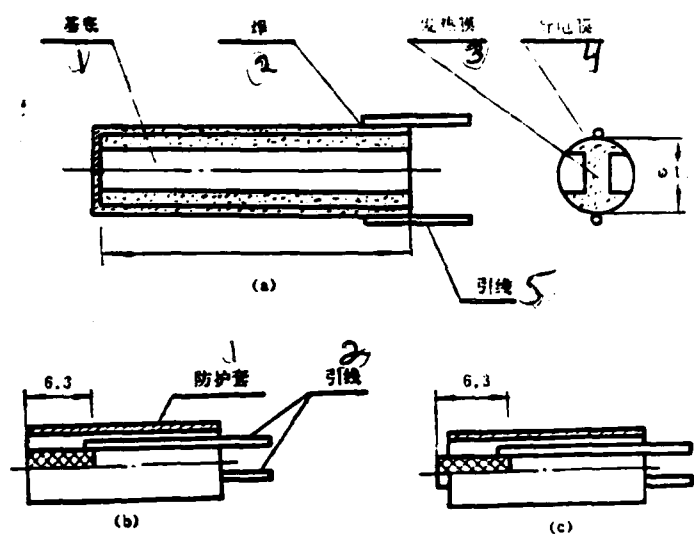


Figure 2. Type B-1 Surface Hot Film

- (a)
1. substrate
 2. welding
 3. heating film
 4. conductive film
 5. leading wire

- (b)
1. protective jacket
 2. leading wire

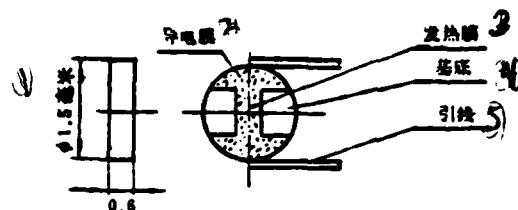


Figure 3. Type P Surface Hot Film

1. 1.5 mm
2. conductive film
3. heating film
4. substrate
5. leading wire

Connecting the surface hot film to the measurement circuit /79 of the isothermic hot wire - hot film wind speed meter (CTA), then

$$Nu = c \frac{E' - E_0}{k \Delta T} \quad (4)$$

where E and E_0 are the output voltage readings of the electrical bridge of the hot wire hot film wind speed meter and its initial reading, k is the thermal conductivity of air, $\Delta T = T_w - T_\infty$ is the difference between the working temperature of the heated film and the temperature of the in-flow, c is a constant related to the size and material of the heating film.

Regardless of the temperature change of the air flow, using single heated film to measure the surface shear stress, the following equation can be obtained from Equations (2) and (4):

$$E' - E_0 = A \tau_w^{1/3} \quad (5)$$

where A is a constant which can be determined by calibration.

In the case of using dual heated films to measure the surface shear stress, if the geometric size, material and working temperature of two films are the same, and the angle θ is not too big, from Equation (3) and Equation (4), it gives:

$$F = \frac{(E_1^2 - E_{01}^2) - (E_2^2 - E_{02}^2)}{(E_1^2 - E_{01}^2) + (E_2^2 - E_{02}^2)} = B \theta \quad (6)$$

where the constant B can be determined by calibration.

Equations (5) and (6) are the basic functions in using surface hot film to measure the direction and magnitude of the wall shear stress.

Applications

Using the calibrated surface hot film to measure the wall shear stress is one of the basic applications. The measurement is not very complicated. According the Equation (5), measurements of the voltage output E and the initial reading E_0 of the electrical bridge are enough to determine the magnitude of the wall shear stress. Figure 4 is obtained by calibrating the wall shear stress within the low speed boundary layer on type M-1 surface hot film using a Preston tube. It indicates a linear relation between $E^2 - E_0^2$ and $\tau_w^{1/3}$. It has also verified Equation (5), which is obtained theoretically. In measuring the wall shear stress, the value can be obtained by measuring $E^2 - E_0^2$ value. Table 1 lists the τ_w values obtained from the calibration curve by measuring the $E^2 - E_0^2$ values at various flow velocities V_∞ within the turbulent boundary layer on a flat plate using type M-1, surface hot film. It indicates that the results are very close to those obtained from theoretical calculation.

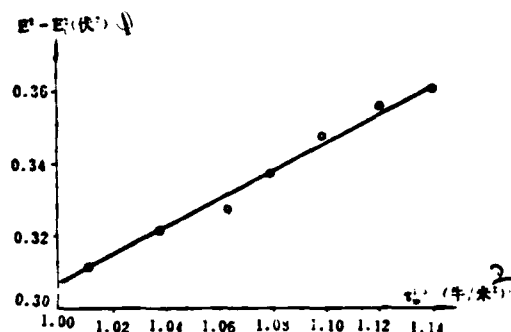


Figure 4. The Calibration Curve of the Type M-1 Surface Hot Film

1. (volt²)
2. (newton/M²)^{1/3}

The second application of the surface hot film is to measure the direction of the wall shear stress, i.e., the direction of the local flow. Figure 5 shows the results of the calibration of the directional sensitivity of type M-1 surface hot film. The calibration was carried out under the condition of constant inflow direction. Various F values were obtained by measuring E_1 , E_2 , E_{01} and E_{02} with different angle θ between the symmetric line of the hot film and the direction of the inflow.

Table 1. The Measured τ_w Value (unit: Newton/M²) Using Type M-1 Surface Hot Film /80

V_∞ (米/秒) ①	25.40	24.60	23.98	23.27	22.54	21.79	21.10
τ_w (表面测量) ②	1.49	1.43	1.35	1.28	1.17	1.12	1.03
τ_w (计算结果) ③	1.53	1.45	1.38	1.31	1.24	1.16	1.09

1. (M/sec)
2. (surface hot film)
3. (calculated result)

Figure 5 shows that F has a linear relation with θ in the range $-35^\circ \leq \theta \leq 35^\circ$. Equation (6), which is obtained theoretically, is also verified. With the calibration curve, the value can be obtained experimentally through the F value by measuring the values of E_1 , E_2 , E_{01} and E_{02} .

The use of a surface hot film for measuring the wall shear stress can be applied in all boundary layers with two or three components, compressible or incompressible flows, laminar or turbulent boundary layers, and with high or low pressure gradients. Therefore, the use of surface hot film to measure the condition of the boundary as well as to determine the transition point and the point of separation of the boundary layer is more meaningful than the measurement of the wall shear stress alone. It has a much broader range of applications. Since the objective of most investigations is the determination of the positions of transition and separation in the boundary layer, it is unnecessary to measure the absolute value of the wall shear stress. It needs only to determine the relative magnitude of the shear stress at various locations along the flow for comparison purposes. In such experiments, it is unnecessary to calibrate the surface hot film. The relative magnitude of the shear stress can be represented by the output voltage of the electrical bridge. The measurement is simple and reliable. The application is illustrated using the following example with transverse flow around the cylinder (two dimensional circle). The condition of the low velocity boundary layer on two dimensional circle is complicated and typical. There are many research results on two dimensional circles in both theoretical and experimental studies. It is readily able to judge the reliability of the experimental results of the surface hot film.

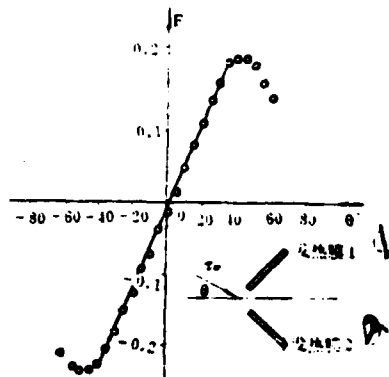


Figure 5. Results of Sensitivity Test of the M-1 Surface Film on the Direction of the Wall Shear Stress

1. heating film 1
2. heating film 2

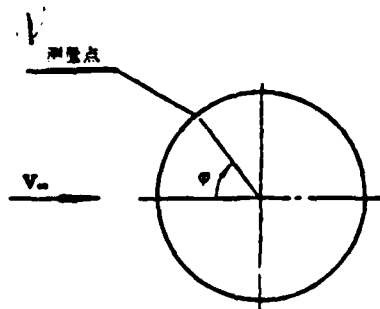


Figure 6. The Central Angle Measured From the Arrest Point

1. point of measurement

The central angle φ of the two dimensional circle is the angle between the measuring point (where the surface hot film is located) and the direction of the inflow. It is measured from the arrest point as shown in Figure 6. Figures 7, 8 and 9 show the test results of the M-1 surface hot film and the results of similar tests carried out in foreign countries. These figures indicate that the results obtained from tests with surface hot films are quite consistent with those obtained from other testing methods. The test results of the M-1 surface hot film are consistent with those obtained with the surface hot films developed in foreign countries. The i shown in Figure 8a is the current passing through the hot film.

The test results shown in Figure 7a are those under a typical flow condition with $Re_d = \rho V_\infty d / \mu = 3.5 \times 10^5$ (d is the diameter of the cylinder), where separation of the two dimensional circle occurs. As shown in Figure 7a, the wall shear stress (time average value) increases with the increase of the angle φ from $\varphi = 0^\circ$. It reaches a maximum with φ approaching 60° and then decreases abruptly when it approaches the separation point. The test results are consistent with the rules. /81

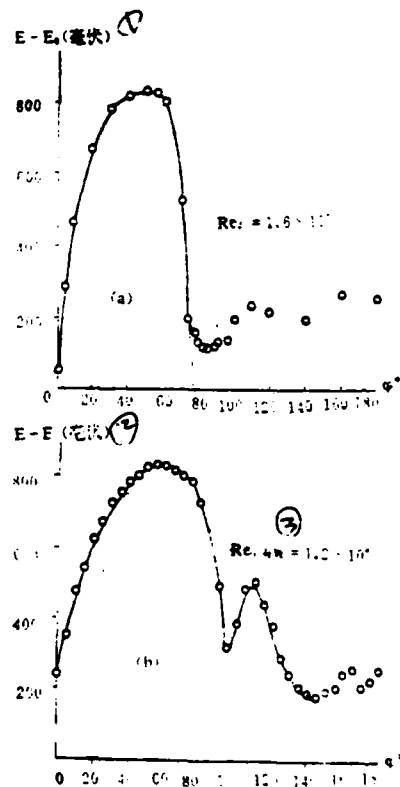


Figure 7. Distribution of the Wall Shear Stress on Two Dimensional Circle Measured Using Type M-1 Surface Hot Film

1. (mV)
2. (mV)
3. $Re_{d, effective} = 1.2 \times 10^6$

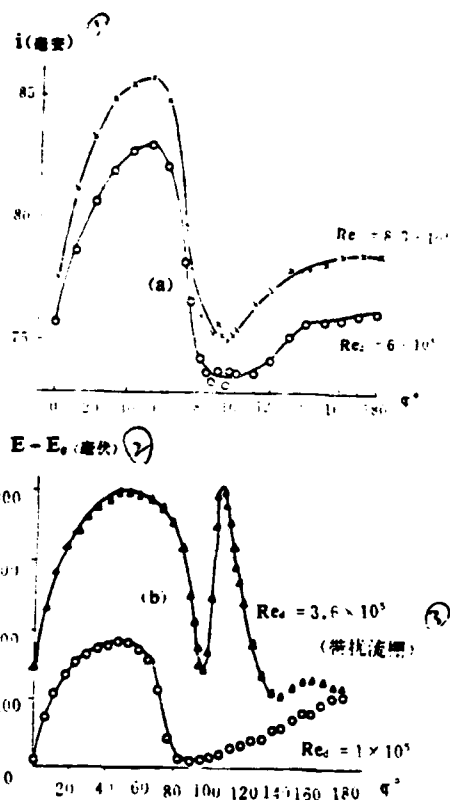


Figure 8. Distribution of the Wall Shear Stress on Two Dimensional Circle Measured Using Surface Hot Film Tested in Foreign Countries[4,7].

1. (mA)
2. (mV)
3. with flow disturbing grid

Theoretically, the second order derivative of the curve should be negative. The curve should intersect with the horizontal axis at the point of separation, at which the wall shear stress is zero. The separation point in the actual flow is fluctuating which makes the wall shear stress show a minimum near the point of separation. The separation point can be determined to be about 78° based on the test result, where there is an abrupt decrease of the wall shear stress. Determination of the separation point by measuring the distribution of the root-mean-square value of the pulsating wall shear stress is a more sensitive method. The distribution can be represented by the root-mean-square values of the pulsating voltage output of the electrical bridge, $\sqrt{e'^2} - \sqrt{e_0^2}$ as shown in Figure 9.

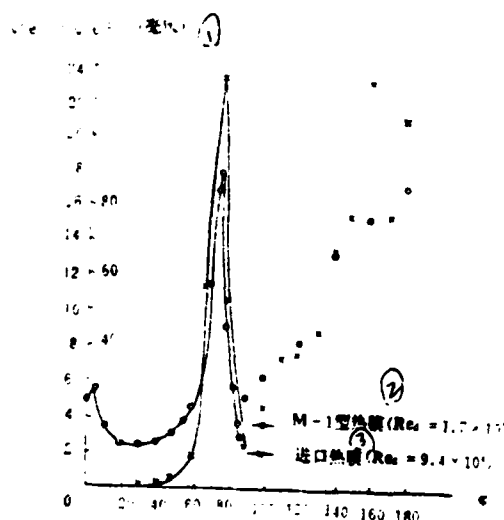


Figure 9. Test Results of the Distribution of the Pulsating Wall Shear Stress on Two Dimensional Circle

1. (mV)
2. M-1 hot film
3. imported hot film

Since the root-mean-square value of the pulsating wall shear stress at the separation point is a maximum, it can be used to determine the position of the separation point. The peak appears clearly at $\phi = 78^\circ$ on the curve shown in Figure 9 and the separation point is readily determined. Another method to determine the position of point of separation is to observe the pulsating signal of the voltage at various ϕ values as shown in Figure 10. Since the point of separation is oscillating, the waveform obtained at $\phi = 0^\circ$ is the arrest point. The wall shear stress is a periodic function with frequency increasing of the Karman's vortex shedding frequency. The disturbance appears on the waveform at the point of separation. The waveform at $\phi = 0^\circ$ is the typical characteristic of the flow in the

187

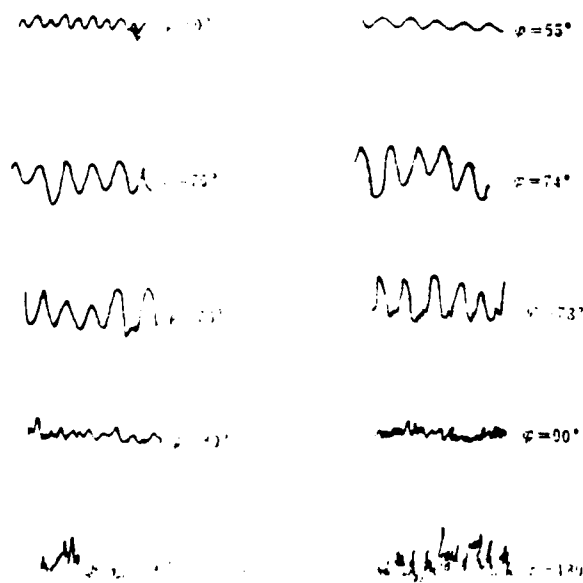


Figure 10. The Voltage output of type M-1 Surface Hot Film Tested on Two Dimensional Circle. $Re_d = 1.7 \times 10^5$.

Figure 7b illustrates the application of the surface hot film in studying the transition of boundary layer from laminar flow to turbulent flow. Since the effective Reynolds Number is larger than 3.5×10^5 , the test results of the distribution of the wall shear stress are different from those obtained at low Reynolds Number. Figure 7b shows that the laminar boundary layer extends to $\varphi = 100^\circ$ before separation. Gas bubbles appear at $\varphi = 110^\circ$ to $\varphi = 110^\circ$. The turbulent boundary layer is reattached to the surface at $\varphi = 110^\circ$, and it is separated from the surface at $\varphi = 140^\circ$.

Figure 11 shows the test results of using surface hot film to measure the wall shear stress on the surface of a wing. The surface hot film is located at $x = 0.8b$ in the front edge of the wing. During experiments, the voltage output of the electrical bridge is monitored with fixed V_∞ and changing angle of attack. The test results show that the turbulent boundary layer exists on top of the wing from the leading edge to $x = 0.8b$ with $\alpha < -1^\circ$. When $\alpha = -1^\circ$, the transition point is located at $0.8b$. The wall shear stress is a minimum at this point. The wall shear stress increases significantly when the measuring point gets into the turbulent boundary layer. With further increase of the angle of attack, the thickness of the boundary layer increases and the wall shear stress decreases. The turbulent boundary layer separates at $x = 0.8b$, when $\alpha = 12^\circ$.

No further discussions of the basic applications and testing methods of the surface hot film are included due to limitation of the size of this paper. A significant amount of studies on the surface hot film as well as the testing methods are currently in progress around the world. Further applications of the surface hot film in aerodynamic tests are very promising.

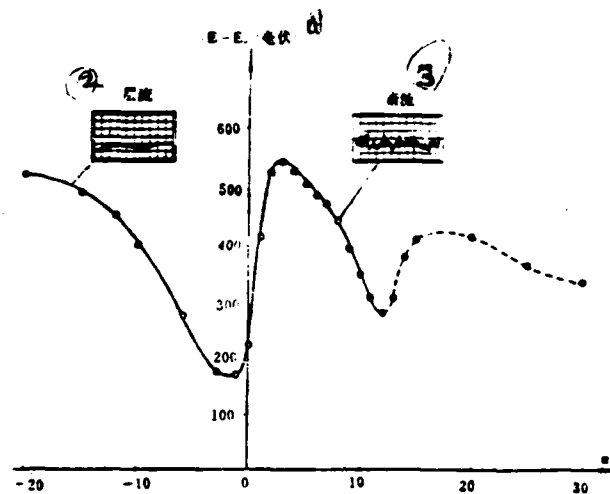


Figure 11. Measurement of the Surface Shear Stress on NACA0012 Aerofoil Using Type M-1 Surface Hot Film ($Re_d = 2 \times 10^5$)

1. (mV)
2. laminar flow
3. turbulent flow

References

- [1] Ludweig, H., Instrument for Measuring the Wall Shearing Stress of Turbulent Boundary Layers, NACA TM 1284, 1950.
- [2] Ludweig, H., and Tillman, W., Investigations of the Wall-Shearing Stress in Turbulent Boundary Layer, NACA TM 1285, 1950.
- [3] Liepmann H, W. and Skinner, G.T., Shearing-Stress Measurements by Use of a Heated Element, NACA TN 3268, 1954.
- [4] Bellhouse, B.J. and Schultz, D.L., Determination of Mean and Dynamic Skin Friction, Separation and Transition in Low-Speed Flow with a Thin-Film Heated Element, J. Fluid Mech., Vol. 24, Part 2, 1966.
- [5] McCroskey, W.J. and Durbin, E.J., Flow Angle and Shear Stress Measurements Using Heated Films and Wires, ASME J. of Basic Engineering, March 1972.

- [6] Meier, H.U., Kreplin, H.P., Experimental Investigation of the Boundary Layer Transition and Separation on a Body of Revolution, Z.F.W. 4, Heft ⁷⁴ 2, 1980.
- [7] Meier, H.U., Kreplin, H.P., Fang, L.W., Experimental Study of Two- and Three- Dimensional Boundary Layer Separation, DFVLR IB 222 81A12, 1981.

THE APPLICATION OF SURFACE HOT FILM IN AERODYNAMIC TESTING

Wang Tiecheng
(Nanjing Aeronautical Institute)

Abstract

In the study of boundary layer, by means of surface hot film, a new way is provided to measure the magnitude and direction of wall shear stress. This paper is written on the basis of investigation and testing of surface hot film. Some basic methods of experiment and limits of application are introduced with our typical experimental results.

Measurement of the Correlation Between the Fluctuating
Pressure and the Fluctuating Velocity in a Turbulent
Boundary Layer

Bian Yuzhong

(Harbin Aerodynamic Research Institute)

J.F. Morrison and P. Bradshaw

(Imperial College of Science and Technology, U.K.)

I. Introduction

The first measurement of the pressure-velocity correlation was conducted by Kawamura and Serafini. Afterward they published many papers on the research of the correlation between the fluctuating wall pressure and the fluctuating velocity, as well as the power spectrum. In their papers, the detail results of the correlation between the fluctuating wall pressure and the fluctuating velocity were supplied by Willmarth and Wooldridge (Ref. 1).

Bradshaw (Ref. 2) studied the correlation between the fluctuating wall pressure and fluctuating velocity in a drastic decelerating boundary layer. He discovered that the convection velocity was slow in the boundary with a reverse pressure gradient. He also utilized Townsend's concept of inactive surface in a reverse pressure gradient.

Willmarth (Ref. 3) and Cantwell (Ref. 4) discussed the experimental study for the structure of the turbulent boundary layer. In recent years, due to the improvement of instrumentation and related technology, a great deal of progress was made in the understanding of the turbulent boundary layer. R.A. Antonia (Ref. 5) discussed the application of the conditional sampling in the turbulent measurement.

The discovery of the law of motion of turbulence along the wall surface advanced the study of turbulence structure. One of the important methods to study the motion is the conditional sampling technique. This paper employed the average of the

primary conditional sampling technique.

The purpose of this paper is to study the correlation variation of the fluctuating wall pressure and the fluctuation longitudinal velocity along the longitudinal (x-direction) and perpendicular (y-direction) distances from the wall. It also describes the structure of the turbulent boundary layer from these variables.

2. Experimental Equipment

The parameters of the wind tunnel for this experiment are [2] listed as follows: testing cross-section, 76.2 x 12.7 centimeters (30 x 50 inches); length, 2.74 meters (9 feet); normal wind speed, 30 meters per seconds; the turbulence rate of the longitudinal free flow in the test section, less than 0.1%; longitudinal pressure gradient, zero.

All the experiments were conducted on the lower tunnel wall. Wires of 0.5 mm diameter were installed on the exit and on the tunnel conversion section for the flow transformation. The mean flow properties, such as the cross section profile of the averaged velocity, the thickness of the boundary layer, thickness of the dislocation boundary layer, and the momentum thickness, were measured with a Pitot tube whose motion in the boundary layer was controlled by a traveling mechanism. The velocity profile and the heat sensor correction constants were obtained from the system analysis performed with a microprocessor. The shear stress on the wall was measured with a Preston tube.

The fluctuating wall pressure was measured with a high sensitivity piezo-resistance transducer. The transducer had an outside case with a diameter of 2.29 millimeter and was capable to measure a pressure as low as 2 pound/in² (maximum output: about 300 mv). It was installed on a copper disc which was

mounted on the lower wall of the wind tunnel. Figure 1 shows the/101 installation diagram of the transducer and the hot wire sensors.

The piezo-transducer was driven by a special designed strain-gage amplifier or a power gage. We adopted the amplifier or the power gage because they could eliminate ordinary interference and they also obtained a wider range of gains. The response of the transducer frequency was calibrated by a Bruel and Kjaer frequency spectrum analyzer.

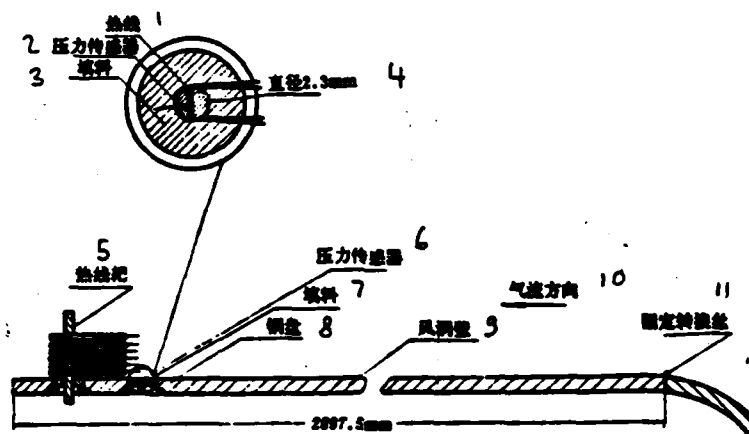


Figure 1. The Installation of Piezo-transducer and Hot Wire

1. hot wire
2. piezo-transducer
3. filling material
4. diameter, 2.3mm
5. hot wire rack
6. piezo-transducer
7. filling material
8. copper disc
9. wind tunnel wall
10. direction of flow
11. stationary transformation wire

The fluctuating velocity was measured by a hot wire rack containing 6 single hot wires.

The signals generated from the piezo-transducer and hot wires were recorded on a magnetic tape with a 14-channel tape recorder. Then they were digitalized from the analog data by a PDP computer.

3. Measurement

All the measurements were conducted in the boundary layer transformed from the fixed transformation wire after the convergence section.

The properties of the turbulent boundary layer are measured as follows:

U(米/秒)	Re _x	Re _θ	C _f	δ(mm)	δ*(mm)	θ(mm)	u _τ (米/秒)	τ _w (牛頓/米 ²)
28.4	5.3 × 10 ⁵	6520	0.0027	34.5	4.6	3.6	1.05	1.26

1. meter/seconds

2. Newton/meter²

The reliability of the non-dimensional power spectrum of the wall pressure ranged $0.038 < \overline{wv}/u_r^2 < 2$.

The measurements were conducted in the range of $1 \text{ Hz} < f < 20 \text{ KHz}$. Hot wire sensors could be moved in the direction of upstream or downstream of the piezo-transducer. This experiment selected three downstream positions of the transducer: $x_1 = 0, 20$, and 40 millimeter. At these three positions, we recorded the wall pressures and the longitudinal fluctuating velocities which were all the functions of time.

The correlation coefficient of pressure-velocity was calculated by the following definition:

$$R_{p,u}(x_1, x_2, x_3, \tau) = \frac{\overline{p(x, 0, 0, t)u(x+x_1, x_2, 0, t+\tau)}}{\sqrt{\overline{p^2}(x, 0, 0, t)} \sqrt{\overline{u^2}(x+x_1, x_2, 0, t)}} \quad (1)$$

4. Results

The root mean square values of the fluctuating pressure in the range of $1 \text{ Hz} < f < 20 \text{ KHz}$ were calculated from the experimental data as follows:

/102

	$\sqrt{\overline{p^2}}/\tau_w$	$\sqrt{\overline{p^2}}/q_w$
直接測量	3.81	9.8×10^{-3}
數據分析	3.96	10.3×10^{-3}
資料[1]	2.64	5.61×10^{-3}

1. Direct Measurement
2. Datum Analysis
3. Data from ref. (1)

The fact that the $\sqrt{\bar{p}^2}/r_w$ value of this paper is larger than that from Ref. (1) can be explained as follows: both the flow velocity and the Reynold number (based on the momentum thickness) were smaller, it is also possible that the experimental data were measured in the range of $1 \text{ Hz} < f < 20 \text{ KHz}$, and consequently the low frequency signals were not filtered. Therefore, in the low frequency test range the noise and the wind tunnel vibration interfered with the experiment results. The data of Ref (1) was conducted in the range of $100 \text{ Hz} < f < 10 \text{ KHz}$, hence, the signals with the frequencies below 100 Hz and above 10 KHz were filtered. Their measurement was conducted in a very narrow frequency range. Therefore they eliminate the noise interference in the low frequency range.

The fluctuating velocities were measured at different positions along the "y" direction with a rack containing six hot wires. It is quite obvious that the hot wire sensors themselves could change the structure of the air flow.

This experiment proved that a regular component of the fluctuating pressure was directly affected by the recognizable velocity characteristics.

Figure 2 shows the pressure velocity correlation coefficients calculated from Equation (1) as a function of the non-dimensional lagging time $[U_\infty(\tau - \tau')]/\delta^*$.

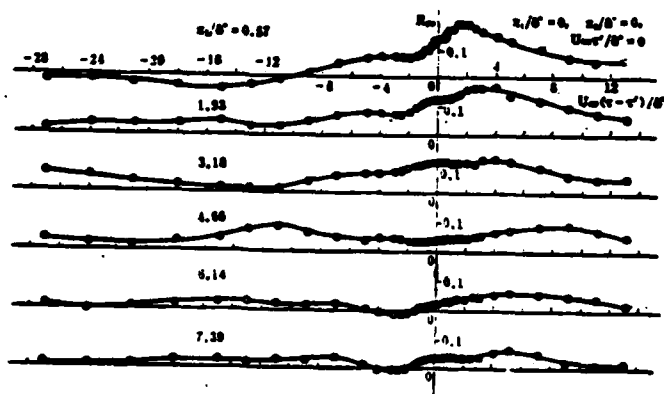


Fig. 2(a)

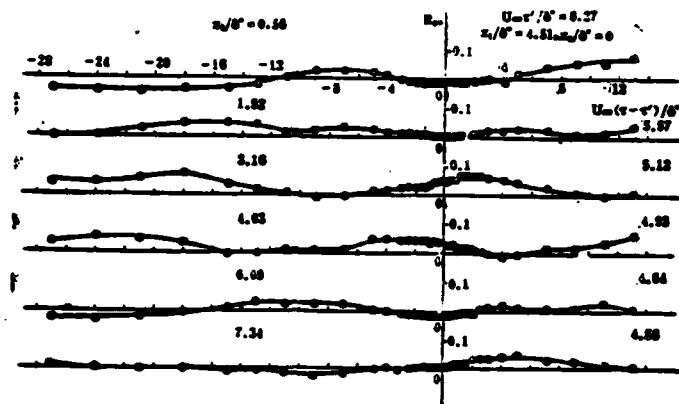


Fig. 2(b)

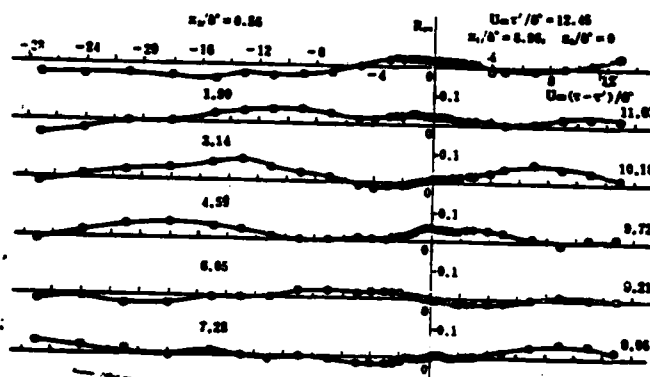


Fig. 2(c)

/103

Figure 2. Correlation Between the Fluctuating Velocity and Fluctuating Pressure

The lagging time τ' was obtained along the longitudinal direction from the local average velocity measured by the hot wire on each specified location. For convenience, $U_\infty \tau' / \delta^*$ is used to replace τ' . At every specified position, on the planes which are respectively parallel to the air flow and perpendicular to the wall surface, the correlation coefficients R_{pu} measured with the hot wire and the piezo-transducer on the wall vary

similarly.

Figure 2(a) shows that at the longitudinal position $x_1/\delta^* = 0$, the correlation coefficient decreases rapidly with the increase of the distance from the wall surface. The maximum value of R_{pu} decreases from 0.185 to 0.065. Figure 2(a) also shows the variations of the correlation coefficient curves when x_1/δ^* equals to 4.51 or 8.96. The maximum of the variation is less than 0.1.

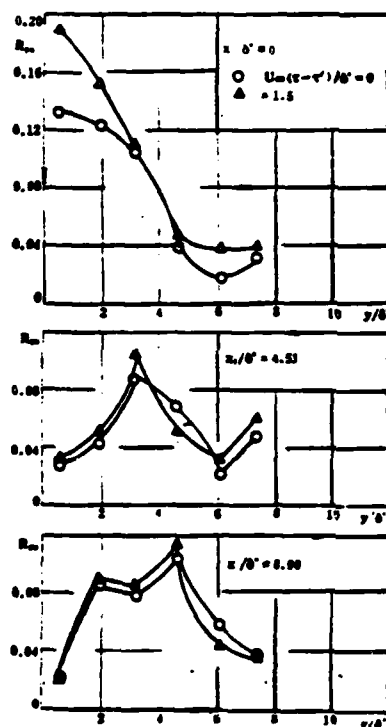


Figure 3. The Changes of the Fluctuating Correlation of Pressure Velocity According to "y"

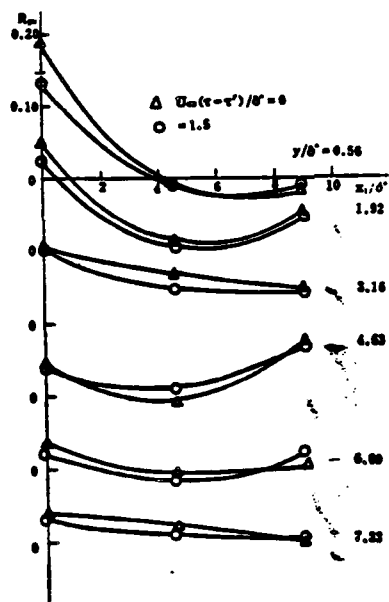


Figure 4. The Changing of the Fluctuating Correlation of Pressure Velocity According to "x"

At different longitudinal position from x_1/δ^* , the fluctuating correlation of the pressure velocity changes with the /104 change of the distance from the wall surface, as shown in Fig. (3). Figure 4 shows when $x_1/\delta^* = 0.56, 3.16$ and 7.33 , the correlation coefficient decreases with the increase of the distance x_1/δ^* . This trend is very obvious near the wall surface. When $y/\delta^* = 1.92, 4.63$ and 6.09 , the curve concaves. A comparison of the data shows that the magnitude of the extreme values of the correlation coefficient decreases but the intervals of the lagging time τ increase. When the hot wire is near the wall surface, the lagging and the variation are large.

5. Conclusion

1. The root means square values of the fluctuation pressure $\sqrt{\bar{p}^2}$ on the wall surface equal 3.81 and $3.93 \tau_w$ respectively.
2. On the wall surfaces, the magnitude of the pressure and the velocity is affected by the boundary layer transformation

condition and Reynold's number (based on the momentum thickness).

3. The fluctuating pressure on the wall surface is directly related to the fluctuating velocity above wall surface. The reverse flow velocity, which is the disturbance velocity directly related to the interference of the wall surface pressure, is the local averaged velocity.

4. The correlation coefficient of fluctuating wall surface pressure and the longitudinal fluctuating velocity is affected by the experiment interference.

References

- [1] Willmarth, W.W. and Wooldridge, C.E., Measurements of the Correlation Between the Fluctuating Velocities and Fluctuating Wall Pressure in a Thick Turbulent Boundary Layer. AGARD rep. 456, 1963.
- [2] Bradshaw, P., Irrotational Fluctuations near a Turbulent Boundary Layer. J. Fluid Mech. 27 (1967), 209
- [3] Willmarth, W.W., Pressure Fluctuations Between Turbulent Boundary Layer. Ann. Rev. Fluid Mech., 7 (1975), 13-38.
- [4] Cantwell, Brian J., Organized Motion in Turbulent Flow. Ann. Rev. Fluid Mech., 13 (1981), 457-515.
- [5] Antonia, R. A., Conditional Sampling in Turbulence Measurement. Ann. Rev. Fluid Mech., 13 (1981), 131-156.

**MEASUREMENT OF THE CORRELATION BETWEEN THE
FLUCTUATING PRESSURE AND THE FLUCTUATING
VELOCITY IN A TURBULENT
BOUNDARY LAYER**

Bian Yuzhong

(Harbin Aerodynamic Research Institute)

J. F. Morrison and P. Bradshaw

(Imperial College of Science and Technology, U. K.)

Abstract

Measurements of the space-time correlation between the fluctuating wall pressure and the fluctuating velocity in a turbulent boundary layer with zero longitudinal pressure gradient are reported.

The structure of the pressure-velocity correlation was obtained from measurements of the correlation between the fluctuating pressure and the fluctuating velocity at various distances in x-direction and various points in y-direction in the boundary layer. The largest variations of pressure-velocity correlation with x-direction and y-direction distances from the pressure transducer are near the pressure transducer.

END

FILMED

8-85

DTIC